

Frequency- and layer-specific  
connectivity within the cortical premotor-motor  
network and the effect of high frequency STN  
stimulation on mouse motor cortical areas in vivo

Dissertation  
zur Erlangung des Grades  
Doktor der Naturwissenschaften  
Im Fachbereich Biologie  
der Johannes Gutenberg-Universität in Mainz

Svenja Lena Kreis  
geb. am 24.01.1993 in Moosburg an der Isar,  
Deutschland

Mainz, November 2024

Dekan: Prof. Dr. Eckhard Thines

1. Berichterstatter: Prof. Dr. rer. nat. Heiko Luhmann

2. Berichterstatter: Prof. Dr. Carsten Duch

Tag der mündlichen Prüfung: 20.02.2025

# 1 Abstract

Brain disorders related to movement such as Parkinson's disease, tremor, or dystonia are prevalent neurological conditions that cause significant impairment for patients. These disorders clinically manifest as slow movement, shaking, stiffness, and difficulty maintaining posture, all of which greatly impact mobility and quality of life for the patient. The disrupted control of movement is a result of abnormal function in motor network circuits. However, the specific origins and effects of these irregular neuronal activity patterns on cortical neural networks remain largely unclear. A critical initial step in understanding these aberrant activity patterns would involve establishing a detailed framework of the physiological connections within the premotor-motor network.

To achieve this, in the first part of my project simultaneous recordings of neuronal activity from all layers of the caudal and rostral forelimb areas in mice, which are proposed homologous to the human primary motor cortex (M1) and the human premotor cortex (PMC), were conducted. The data was analyzed for spectral power, as well as functional and effective connectivity. This method enabled to examine the layer- and frequency-specific connectivity within the RFA-CFA network in wild-type mice. Further, in collaboration with my colleague, high-density electroencephalography recordings were made from the premotor and primary motor cortex of healthy human subjects. Applying a similar analysis pipeline to the human data, as employed for mouse data, allowed me to compare the data gathered from the motor network of wild-type mice with the premotor-motor network in healthy human subjects at rest. This approach revealed a notably higher spectral power in the  $\beta$ - and  $\gamma$ -frequency bands in the PMC region of the human brain compared to the M1 region, and similarly in mice CFA layers (L) 2/3 and 5 compared to RFA. The data also revealed a strong  $\beta$ -band functional connectivity between the PMC and M1 in humans, and between the CFA L6 and RFA L5 in mice. The analysis showed that the information flow mediated by  $\beta$ - and  $\gamma$ -band oscillations is predominantly directed from the PMC towards the M1 in humans, and similarly from the RFA to the CFA in mice. By combining spectral power, functional, and effective connectivity, the study found strong similarities between the human PMC-M1 network and the mice RFA-CFA network. Suggesting, that the reciprocal connectivity of the mice RFA-CFA circuitry represents a suitable model for the analysis of motor control, physiological PMC-M1 functioning and pathological transformations within this network.

High frequency deep brain stimulation (DBS) of the subthalamic nucleus (STN) is an effective evidence-based therapy for Parkinson's disease; however, its effects on the motor network are unclear. The first step in understanding the mechanism of action of DBS is deciphering the physiological and pathophysiological patterns of motor network connectivity.

Therefore, the second part of my project was to analyse the layer- and frequency-specific effects of STN DBS on the connectivity between STN, RFA and CFA. Multi-site extracellular recordings served to quantify local field potential activity at rest and during burst STN stimulation at multiple stimulation frequencies. The combination of layer- and frequency-specific LFP power, functional and effective connectivity (EC) analysis demonstrated that 160 Hz STN stimulation leads to significant, frequency- and layer-specific changes within the analysed network. More specifically, an increase in high  $\gamma$  power in RFA and CFA was observed. Additionally, high frequency STN stimulation reduced the  $\beta$ - and high  $\gamma$ -frequency coherence between RFA, CFA, and STN, as well as the EC from STN toward RFA and CFA, but no change in the connectivity from cortex toward STN was attested, demonstrating hyperdirect pathway activation. Thus, the present dissertation adds empirical insights into the mechanisms of action of DBS, which represent an important basis for further development of this therapy.

## Zusammenfassung

Bewegungsstörungen wie die Morbus Parkinson, Tremor oder Dystonie sind weit verbreitete neurologische Erkrankungen, die bei den Patienten zu erheblichen Beeinträchtigungen führen. Diese Störungen äußern sich klinisch durch langsame Bewegungen, Zittern, Steifheit und Schwierigkeiten bei der Aufrechterhaltung der Körperhaltung, was die Mobilität und Lebensqualität der Patienten stark beeinträchtigt. Die gestörte Kontrolle von Willkürmotorik ist das Ergebnis einer abnormen neuronaler Funktion in dem motorischen Netzwerkes. Die spezifischen Ursachen und Auswirkungen dieser pathophysiologischen neuronalen Aktivitätsmuster auf die kortikalen neuronalen Netzwerke sind jedoch noch weitgehend unklar. Ein entscheidender erster Schritt zum Verständnis dieser abweichenden Aktivitätsmuster ist die Erstellung eines detaillierten Modells für die physiologischen Verbindungen innerhalb des prämotorisch-motorischen Netzwerkes. Um dies zu erreichen, wurden im ersten Teil meines Projekts simultane Aufzeichnungen der neuronalen Aktivität aus allen Schichten der kaudalen und rostralen Areale der Vordergliedmaßen von Mäusen durchgeführt, die als homolog zum menschlichen primären motorischen Kortex (M1) und zum menschlichen prämotorischen Kortex (PMC) gelten. Die Daten wurden hinsichtlich der spektralen Leistung sowie der funktionellen und effektiven Konnektivität analysiert. Diese Methode ermöglichte die Untersuchung der schicht- und frequenzspezifischen Konnektivität innerhalb des RFA-CFA-Netzwerkes in wildtypischen Mäusen. Darüber hinaus wurden in Zusammenarbeit mit meinem Kollegen hochauflösende Elektroenzephalographie-Aufzeichnungen vom prämotorischen und primären motorischen Kortex gesunder menschlicher Probanden durchgeführt. Die human Daten sowie die Mausdaten wurden mit einer identischen Analyse-Pipeline ausgewertet, dies ermöglichte es mir die Daten aus dem motorischen Netzwerk von Wildtyp-Mäusen mit dem prämotorisch-motorischen Netzwerk gesunder Menschen in Ruhe zu vergleichen. Diese Analyse zeigte eine deutlich höhere spektrale Leistung in den  $\beta$ - und  $\gamma$ -Frequenzbändern in der PMC-Region des menschlichen Gehirns im Vergleich zur M1-Region und in ähnlicher Weise in den CFA-Schichten (L) 2/3 und 5 der Mäuse im Vergleich zur RFA. Die Daten zeigten auch eine starke  $\beta$  Band-Konnektivität zwischen dem PMC und M1 bei Menschen und zwischen dem CFA L6 und RFA L5 bei Mäusen. Die Analyse zeigte, dass der durch  $\beta$  und  $\gamma$  Band Oszillationen vermittelte Informationsfluss bei Menschen vorwiegend vom PMC zum M1 und bei Mäusen in ähnlicher

Weise vom RFA zum CFA gerichtet ist. Durch die Kombination von spektraler Leistung, funktioneller und effektiver Konnektivität fand die Studie starke Ähnlichkeiten zwischen dem menschlichen PMC-M1-Netzwerk und dem RFA-CFA-Netzwerk der Maus. Dies deutet darauf hin, dass die reziproke Konnektivität der RFA-CFA-Netzwerk in Mäusen ein geeignetes Modell für die Analyse der motorischen Kontrolle, der humanen physiologischen PMC-M1-Funktion und der pathologischen Veränderungen innerhalb dieses Netzwerks darstellt.

Die hochfrequente tiefe Hirnstimulation (DBS) des Nucleus subthalamicus (STN) ist eine wirksame, evidenzbasierte Therapie für die Parkinson-Krankheit; ihre Auswirkungen auf das motorische Netzwerk sind jedoch unklar. Der erste Schritt zum Verständnis des Wirkmechanismus der DBS ist die Entschlüsselung der physiologischen und pathophysiologischen Muster der Konnektivität des motorischen Netzwerks.

Daher bestand der zweite Teil meines Projekts darin, die schicht- und frequenzspezifischen Auswirkungen der STN-DBS auf die Konnektivität zwischen STN, RFA und CFA zu analysieren. Zeitgleiche, extrazelluläre Ableitungen neuronaler Aktivität an mehreren Hirnregionen dienten zur Quantifizierung der lokalen Feldpotentialaktivität in Ruhe und während der STN-Burst-Stimulation bei verschiedenen Stimulationsfrequenzen.

# Table of Contents

1	Abstract.....	2
	Zusammenfassung.....	4
2	Introduction .....	9
2.1	The premotor-motor network .....	9
2.2	Cortico-basal ganglia circuit .....	13
2.3	Spontaneous neural activity.....	17
2.3.1	Relevance of beta band activity .....	20
2.3.2	Relevance of gamma band activity.....	22
2.4	High frequency stimulation of the STN .....	23
2.5	Aims of the thesis .....	25
3	Materials and Methods.....	27
3.1	Animals.....	27
3.2	Surgery.....	27
3.3	Electrophysiological recordings.....	29
3.4	Tissue preparation and Immunohistochemistry .....	32
3.5	Analysis of Electrophysiology .....	32
3.5.1	Raw data processing.....	33
3.5.2	Local Field Potential Power .....	34
3.5.3	Beta and gamma-burst detection.....	35
3.5.4	Functional connectivity analysis.....	35
3.6	Microscopy and image processing .....	38
4	Results.....	40
4.1	Premotor-motor network in the mouse motor cortex .....	40
4.1.1	Spontaneous activity in the mouse motor cortex.....	40
4.1.2	Functional connectivity between RFA and CFA.....	44

4.1.3	Effective connectivity between RFA and CFA.....	47
4.1.4	Structural equation modelling.....	51
4.2	Effect of high frequency stimulation in the RFA-CFA-STN network.....	52
4.2.1	Neuronal activity in all layers of RFA, CFA and the STN returns to baseline within 10 min after STN stimulation .....	55
4.2.2	High frequency STN stimulation induces a decrease in spectral LFP power in the $\beta$ -frequency band in RFA, CFA and STN.....	62
4.2.3	High frequency stimulation modulates cortical and subcortical long $\beta$ -bursts .....	65
4.2.4	High frequency stimulation modulates cortical and subcortical $\gamma$ -bursts.....	70
4.2.5	High frequency STN stimulation reduces functional connectivity between RFA, CFA and STN	75
4.2.6	Effect of high frequency STN stimulation on the effective connectivity between RFA, CFA and STN .....	80
4.3	Results summary .....	85
5	Discussion.....	87
5.1	Mouse motor cortical areas RFA and the CFA as a model for human premotor-motor network .....	87
5.1.1	Spontaneous activity in the mouse motor cortex and its similarity to the human PMC-M1 network .....	87
5.1.2	Functional and effective connectivity between the mouse RFA and CFA and its similarities to the human PMC-M1 network.....	88
5.1.3	Oscillations at $\beta$ - and $\gamma$ -frequencies as biomarkers in the premotor-motor network	89
5.2	Effect of high frequency STN stimulation on the RFA-CFA-STN network.....	90
5.2.1	High frequency STN stimulation induces a decrease in spectral LFP power in the high $\gamma$ -frequency band in RFA, CFA and STN.....	91
5.2.2	High frequency STN stimulation reduces the occurrence of long $\beta$ - and $\gamma$ –bursts..	92

5.2.3	High frequency STN stimulation induces a reduction in functional and effective connectivity between RFA, CFA and STN .....	93
6	Conclusion and Outlook.....	94
7	References .....	97
8	Curriculum Vitae .....	117
9	List of Publications .....	120
10	Acknowledgements.....	121
11	Abbreviation.....	122

## 2 Introduction

Movement disorders, including highly prevalent conditions like Parkinson's disease (PD), essential tremor, and dystonia, pose significant neurological challenges, leading to considerable disability for the patients. Parkinson's disease is characterized by a wide range of debilitating motor symptoms such as bradykinesia, tremor, and rigidity, collectively leading to a substantial burden on patients' mobility and overall quality of life (Muthuraman et al. 2015; Bloem et al. 2021). The underlying cause of these motor impairments is attributed to the aberrant functioning of motor network circuitries (Muthuraman et al. 2018; Muthuraman M et al. 2018). However, the mechanisms by which these abnormal activity patterns originate and disrupt the physiological activity within neural circuits remain largely unexplored (Kreis et al. 2022; Mirzac et al. 2023). Consequently, there is a need to investigate the properties of, and the connectivity within, the premotor motor network and to build a robust model of motor cortical activity and connectivity that can shed light on the underlying physiological processes. Identifying such frameworks in a mouse model would allow the identification of specific neural pathways that are disrupted in movement disorders in mice, which in turn leads to a better understanding of the pathophysiological changes in PD patients.

### 2.1 The premotor-motor network

The motor cortex network is a highly complex system of interconnected neurons that is essential for initiating, and controlling voluntary movements. This network is comprised of at least 11 distinct motor areas that can be identified based on their characteristic cellular architecture and connectivity to subcortical nuclei and further cortical areas (Young et al. 2012). The complex connectivity between these areas, which consists of both hierarchical and parallel processing is necessary to achieve fine motor control (Zimmerman and Kirshner 2023).

The M1 is located in the precentral gyrus and is highly interconnected with many cortical areas, including the supplementary motor area and the PMC. Additionally, it projects to the brainstem and motor neurons in the spinal cord (Yokoi et al. 2018). The M1 receives

regulatory input from the basal ganglia and cerebellum via relays in the ventrolateral thalamus (Purves 2001; Yokoi et al. 2018).

The M1 is critical for encoding essential parameters necessary for the execution of voluntary movements, such as force, direction, speed, and magnitude (Purves 2001). Additionally, the M1 is essential for the initiation of voluntary movement and fine motor control (Bakken TE. et al. 2021; Zimmerman and Kirshner 2023).

The PMC, which is situated on the lateral surface of the cortex anterior to M1, is comprised of dorsal and ventral subdivisions and is a critical component of the cortical motor system (Nudo and McNeal 2013; Yip and Lui 2024). Axons originating in the PMC directly innervate the M1 area, as well as the spinal cord (Yip and Lui 2024). The PMC receives input from various brain regions, including the sensory cortex, the parietal cortex, and the basal ganglia. These inputs enable the PMC to integrate information from a range of sources, such as sensory information (e.g., the location of an object) and cognitive information (e.g., the goal of the movement) necessary for the planning and preparation of movements (Hu et al. 2018). This results in more intricate, task-related processing of information in the PMC compared to the M1.

Numerous studies have investigated the function and intricate connectivity between the primary motor cortex (M1) and premotor cortex (PMC) in humans and non-human primates. These studies have shed light on the important role that the M1 and PMC play in the initiation and control of voluntary movements (Johansen-Berg et al. 2004; Groppa and Schlaak et al. 2012; Groppa and Werner-Petroll et al. 2012). The interaction between the PMC and M1 is essential for achieving goal-directed movement (Münchau et al. 2002). The PMC is known to have robust anatomical connections to M1, which leads to the modulation of neuronal activity within the M1 (Chouinard and Paus 2006; Groppa and Schlaak et al. 2012; Groppa and Werner-Petroll et al. 2012).

However, the homologous network in mice has not received the same level of scrutiny, despite the widespread use of mice as model organisms in the study of various movement disorders, including Parkinson's disease, and potential therapeutic interventions. Understanding the intricacies of the mouse motor cortex, including its physiological neuronal activity and the connectivity between its distinct regions, is paramount for several reasons.

Firstly, mice serve as invaluable models for studying human neurological conditions due to their genetic, physiological, and behavioural similarities to humans. Leveraging mouse models allows researchers to investigate the fundamental mechanisms underlying movement disorders and explore potential therapeutic strategies in a controlled and ethically sound manner. However, to fully capitalize on the translational potential of mouse models, it is essential to establish a comprehensive understanding of the mouse motor network and its functional organization. Secondly, elucidating the neuronal activity patterns and connectivity within the mouse motor cortex provides crucial insights into normal brain function and dysfunction. By characterizing the physiological dynamics of the motor cortical circuitry, it is possible to identify aberrant patterns associated with movement disorders and develop targeted interventions to restore physiological function. Moreover, comparative studies between mouse and human motor networks enable researchers to validate the translational relevance of mouse models and bridge the gap between preclinical research and clinical applications. Furthermore, unravelling the complexities of the mouse motor cortex offers opportunities for exploring novel therapeutic targets and treatment modalities. By dissecting the circuit-level mechanisms underlying motor dysfunction, researchers can identify potential pharmacological or neuromodulatory interventions to alleviate symptoms and improve patient outcomes. Understanding the neural circuitry involved in motor control may facilitate the development of innovative neurotechnologies, such as deep brain stimulation or optogenetic approaches, for precision neuromodulation in movement disorders. In conclusion, a detailed understanding of the mouse motor cortex, its physiological neuronal activity, and the connectivity between its different areas is indispensable for advancing our knowledge of movement disorders and developing effective therapeutic strategies. By leveraging mouse models and employing state-of-the-art neurophysiological techniques, researchers can unravel the intricacies of motor circuitry and pave the way for transformative advancements in the field of neuroscience and clinical neurology.

Although the motor cortex is highly conserved across mammals (Ebbesen and Brecht 2017), the precise role of different regions of the mouse motor cortex including the homologues to the human brain is not yet fully understood. The rodent motor cortex, much like its human counterpart, exhibits a layered structure characterized by distinct neuronal inputs and

axonal projections (Lee et al. 2022; Carmona et al. 2024). Thalamocortical and corticocortical projections primarily contribute to the inputs received by the rodent motor cortex areas, reflecting a hierarchical organization of cortical layers that is conserved across mammalian species (Bakken TE. et al. 2021; Yao M et al. 2023). Layer 2/3 is involved in receiving sensory information from the thalamus and the spinal cord. Layer 5 is characterized by its prominent pyramidal neurons and is involved in sending motor signals to the spinal cord and brainstem motor centres (Carmona et al. 2024). Layer 6 is involved in integrating information from the different layers of the cortex (Lee et al. 2022). However, the axonal projection pattern of the input does not always match with the cell layer the input cells are interacting with, since neurons of M1 send dendrites across layers (Lee et al. 2022).

The motor map of the mouse and rat shares similarities in organization and cytoarchitecture (Donoghue and Wise 1982; Tennant et al. 2011). Through the use of intracortical microstimulation (Neafsey and Sievert 1982; Rouiller et al. 1993; Tennant et al. 2011) and Channelrhodopsin-2-photostimulation mapping (Hira et al. 2013), two spatially distinct motor forelimb areas have been identified in the rodent motor cortex: the rostral forelimb area (RFA) and the caudal forelimb area (CFA). Anatomical tracing studies using anterograde and retrograde tracing have demonstrated robust reciprocal connections between RFA and CFA (Rouiller et al. 1993; Hira et al. 2013; Mohammed and Jain 2014; Urban lii et al. 2024). Neurons in RFA project axons that innervate neurons in CFA, and vice versa, forming a dense network of interconnections between these two regions. This bidirectional connectivity suggests that RFA and CFA exchange information and collaborate closely in motor control tasks. Both areas receive unique input from various brain regions, however, the RFA and CFA target distinguishable populations of spinal neurons, comparable to the human PMC and M1 (Carmona et al. 2024).

Both the CFA and RFA are involved in controlling arm and hand movements, although their exact roles are uncertain (Carmona et al. 2024).

Mohammed and Jain (2014) used transcranial optogenetic cortical silencing to show, that both RFA and CFA are essential for goal-directed movements. Additionally, optogenetic stimulation of RFA or CFA leads to forelimb movement in mice (Hira et al. 2015; Brown et al. 2023). It has been speculated that they are organized in an analogous way to the primate frontal cortex (Neafsey and Sievert 1982; Rouiller et al. 1993; Mohammed and Jain

2014) with CFA as a homolog to the primary motor cortex and RFA as a homolog to the premotor area or supplementary motor areas (Rouiller et al. 1993; Dancause et al. 2006; Eisner-Janowicz et al. 2008). However, the idea of a hierarchical premotor-motor organization is frequently challenged (Graziano et al. 2002; Hira et al. 2015).

There is very limited information available on the electrophysiological properties of RFA and CFA and the functional and effective connectivity between the two areas (Giordano et al. 2023). Various studies have reported a suppression of motor cortical activity during forelimb movement in headfixed mice and rats (Hira et al. 2013; Ebbesen and Brecht 2017). This inhibition during motor activity in both primary motor and premotor areas is most likely mediated by GABAergic fast-spiking neurons (Giordano et al. 2023). Similar results have been observed in humans and primates.

Recordings of neuronal activity in freely moving mice showed significantly higher activity in CFA compared to RFA (Das A et al. 2023). Additionally, Hira et al. (2015) found, that photostimulation of RFA increased neuronal activity in the CFA (Hira et al. 2015). However, there are no studies available, analyzing the connectivity between RFA and CFA in rodents.

Detailed information on the electrophysiological properties of the RFA and CFA, as well the how these areas are functionally connected can provide important insights into how these two areas control forelimb movements. A better understanding of this network could lead to new treatments for neurological disorders that affect movement, such as Parkinson's disease.

## 2.2 Cortico-basal ganglia circuit

The basal ganglia network is a complex and intricate system of interconnected structures located deep within the brain, playing a crucial role in a wide range of essential functions, including voluntary movement, motor learning, habit formation, and various cognitive and emotional processes (Haber 2017; Foster NN. et al. 2021)

At the core of this network are the striatum, globus pallidus, substantia nigra, and the subthalamic nucleus (STN) (Faull and Laverly 1969).

The striatum, composed of the caudate nucleus and putamen, is the main input structure of the basal ganglia (Tisch et al. 2004). It receives inputs from the cerebral cortex, thalamus,

and midbrain, and integrates this information to modulate motor, cognitive, and limbic functions (Groenewegen 2003; Wichmann and DeLong 2008). The globus pallidus, divided into external (Gpe) and internal (Gpi) segments, serves as the primary output structure of the basal ganglia (Tisch et al. 2004). The substantia nigra, with its two parts substantia nigra pars compacta (SNpc) and substantia nigra pars reticulata (SNr), plays a crucial role in the regulation of movement, with the pars compacta providing dopaminergic input to the striatum, and the SNr serving as an output nucleus (Tisch et al. 2004). The subthalamic nucleus (STN), a small, lens-shaped structure, receives excitatory inputs from the cortex and sends inhibitory projections to the globus pallidus, thereby influencing the overall output of the basal ganglia (Groenewegen 2003; Wichmann and DeLong 2008). The STN receives afferents from a broad spectrum of cortical areas involved in decision-making and movement control and is therefore thought to be a central hub in determining when and how vigorously a movement should be performed (Jahanshahi et al. 2015; Aron et al. 2016). Through these interconnected structures and their functional relationships with the cerebral cortex and thalamus, the STN, and the basal ganglia are involved in a variety of processes, such as the facilitation of desired motor programs, the suppression of competing or unintended movements, and the integration of cognitive, limbic, and motor information (Groenewegen 2003; Wichmann and DeLong 2008).

The basal ganglia form three cortico-thalamic pathways that start in the cortex and converge in the internal globus pallidus, an output structure which projects through the thalamus back to the cortex. The three main pathways are the direct pathway, the indirect pathway and the hyperdirect pathway (Figure 1).

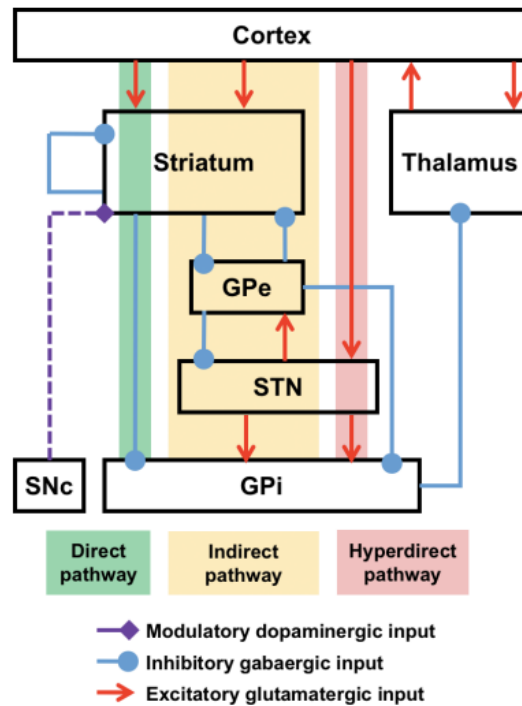


**Figure 1: Box and arrow diagram of the corticobasal ganglia network and pathways.**  
Figure from (Héricé et al. 2016).

The direct pathway originates in the cortex and projects via excitatory glutamatergic neurons to the striatum. The inhibitory GABAergic neurons from the striatum then send their axons to the medial globus pallidus and SNr. Inhibitory neurons from the GPi and SNr, project their axons to the thalamus. Excitatory pathways then extend from the thalamus back to the cortex. This system operates on the principle of positive feedback. The serial connection of the two inhibitory synapses means the first inhibitory neuron suppresses the activity of the second; resulting in a reduction of the inhibitory influence the globus pallidus has over the thalamus, a process known as disinhibition. This disinhibition is equivalent to excitation of the motor cortex, and thus the final function of the direct pathway is to increase motor activity.

The indirect pathway originates in the cortex and terminates in the striatum, similar to the direct pathway. However, instead of sending axons directly to the striatum or the STN, the neurons project to the external globus pallidus. The neurons from the GPe send inhibitory fibers to the STN instead of directly to the thalamus. From the subthalamic nucleus, neurons send their axons to the GPi/SNr and continue as the direct pathway with GABAergic inhibitory neurons to the thalamus and glutamate excitatory efferents to the cortex. The

striatum inhibits the GPe, resulting in disinhibition of the subthalamus. This causes the neurons of the subthalamus to become more active and excite the GPi, thereby inhibiting the thalamic nuclei. The result of this pathway is a decrease in activity of cortical motor neurons and the suppression of unplanned movements.

The direct pathway is involved in initiating movement, while the indirect pathway is involved in suppressing movement. In Parkinson's disease, there is an imbalance between these two pathways, with the indirect pathway becoming too active (Foster NN. et al. 2021).

The hyperdirect pathway comprises neurons that extend from the cortex directly to the STN. These fibers transmit robust excitatory signals to the GPi/SNr with a shorter conduction time than the direct and indirect pathways, circumventing the striatum.

When the cerebral cortex sends glutamatergic inputs directly to the subthalamic nucleus, it subsequently stimulates the GPi/SNr, thereby suppressing thalamic activity on the cerebral cortex and increasing inhibitory influences on the upper motor neurons. Consequently, in conjunction with the indirect pathway, only the chosen motor program is executed, while other competing motor programs are halted.

In brief, when a specific motor pattern is computed by the cerebral cortex, it is initially transmitted to the basal ganglia via glutamatergic projections to the striatum. The purpose of this is to release the intended movement and suppress unintended ones. The direct pathway transfers information from the striatum to GPi/SNr through GABAergic inhibitory projections, thereby selectively reducing its activity and initiating movement by releasing firing from the thalamocortical neurons. Moreover, the cerebral cortex suppresses competing motor programs via the indirect and hyper-direct pathways in addition to the initial signal to the striatum. When the striatum receives glutamatergic inputs from the cerebral cortex, it sends inhibitory signals to the GPe, which typically exerts GABAergic inhibition on the STN. As a result, the glutamatergic excitatory neurons of the STN can then stimulate the GPi/SNr, thereby suppressing thalamic activity on the cerebral cortex and increasing inhibitory influences on the upper motor neurons.

## 2.3 Spontaneous neural activity

A goal of neuroscience is to understand the intricate relationship between brain function and underlying neural activity, with a key aspect being the exploration of spontaneous neuronal activity. This term refers to intrinsic activities not directly triggered by external events. Spontaneous activity, characterized by the activity pattern of neurons in the absence of sensory input, is a fundamental property of nervous systems, a deep knowledge of this baseline activity is essential for understanding brain function (Liu et al. 2022). Spontaneous neuronal activity provides valuable insights into resting-state networks of the brain, shedding light on intrinsic neural patterns that underlie various cognitive processes. It illustrates how the inherent activity of neurons can generate oscillations, providing internal context to sensory input and influencing global functional states such as attention and consciousness (Llinás 1988). The spontaneous firing of single neurons is intricately linked to the cortical networks in which they are embedded (Uddin 2020). This leads to synchronized activity across a large population of neurons. The structured nature of spontaneous activity in cortical populations, both spatially and temporally, reflects the underlying connectivity of the cortical network. This spatio-temporal structure interacts dynamically with external stimulation, shaping responses to individual presentations of stimuli (Ringach 2009).

Examining the spontaneous activity of neurons offers a unique perspective on the intricate workings of the brain at resting state, offering crucial information about intrinsic neural patterns, functional connectivity, and the modulation of brain states. These investigations are instrumental in deepening our understanding of brain function and cognition and have significant implications for various fields of neuroscience research.

Spontaneous neural activity can be recorded using various techniques, each with its specific advantages and challenges. Electroencephalography (EEG) is a non-invasive method that measures oscillatory electrical activity from the brain through electrodes placed on the scalp, offering valuable information about overall brain activity and useful for studying large-scale brain networks. Functional magnetic resonance imaging (fMRI) is a powerful and non-invasive imaging technique that detects changes in blood flow and oxygenation levels in the brain, providing a higher spatial resolution than EEG and is commonly used as a proxy to investigate brain activity during rest and task-based activities. Optical methods, such as calcium imaging, allow an invasive visualization of the activity of individual neurons by

detecting changes in intracellular calcium levels, offering high spatial and temporal resolution. The implantation of multielectrode arrays (MEA) enables invasive simultaneous recordings from multiple brain regions with high temporal and also good spatial resolution, providing insights into the spatiotemporal dynamics of neural circuits, particularly valuable for studying interactions between different brain regions.

In this study, multi-electrode arrays were employed to record spontaneous, extracellular neuronal activity simultaneously from the STN and two motor cortical areas, allowing me to capture the dynamic interactions between these regions and investigate their functional and effective connectivity.

The recorded raw signal can be divided into two components: multi-unit activity and local field potential (LFP). Multi-unit activity refers to the high frequency (>1000 Hz) portion of recordings, which reflects the action potentials generated by local neurons. In contrast, LFP represents the summation of excitatory and inhibitory dendritic potentials that are recorded from a population of neurons. By analyzing LFP, physiological features such as functional connectivity, power, or phase coupling can be analysed, providing valuable insights into the dynamic landscape of spontaneous neural activity.

The low-pass filtered LPF signal is traditionally divided into different frequency band intervals, namely delta ( $\delta$ , 0.1-3 Hz), theta ( $\theta$ , 4-7 Hz), alpha ( $\alpha$ , 8-15 Hz), beta ( $\beta$ , 16-31 Hz), low gamma (low  $\gamma$ , 32-49 Hz), medium gamma (medium  $\gamma$ , 51-75 Hz), and high gamma (high  $\gamma$ , 76-100 Hz (Penttonen and Buzsáki 2003). Each band is linked to specific physiological functions and contributes differently to information processing (Pevzner et al. 2016).

Delta waves ( $\delta$ ) are generated by prolonged hyperpolarization of pyramidal neurons and are mainly observed during non-rapid-eye-movement sleep in various species such as mice (Hubbard et al. 2020), rats (Franken et al. 1991), and humans (Dijk et al. 1987; Achermann and Borbély 1997). Additionally, the  $\delta$ -frequency band is associated with cognitive processes such as decision-making and attentional processes (Güntekin and Başar 2016). Neuronal activity in the  $\delta$ -frequency band is also linked to memory consolidation and synaptic plasticity (Assenza and Di Lazzaro 2015).

Theta ( $\theta$ ) frequency band activity has first been observed in the hippocampus and is associated with memory formation and spatial navigation. These oscillations are thought to

have a crucial role in the encoding and retrieval of memories (Salari et al. 2012; Ostrowski and Rose 2024).

Additionally, the  $\theta$  band has been identified in frontal and central cortical regions (Wiecki and Frank 2010), to be involved in various functions distinct from voluntary movement control, sensory processing, working memory, and memory consolidation in healthy individuals (Ekstrom et al. 2005; Cohen 2014; Karakaş 2020; Ostrowski and Rose 2024). Multiple studies have indicated that  $\theta$ -frequency activity is important during inhibitory control (Dippel et al. 2017; Pscherer et al. 2019; Adelhöfer and Beste 2020). For instance, the strength of resting state  $\theta$  activity was found to modulate the effects of conflicts during motor inhibitory control trials known as Go/Nogo task on healthy human subjects at the parietal cortex level (Pscherer et al. 2019). Similarly, several research works showed that middle frontal gyrus-related resting state  $\theta$  activities influence response inhibition processes (Lansbergen et al. 2007, 2007; Schiller et al. 2014).

The alpha ( $\alpha$ ) frequency band is known to modulate sensory processing, particularly in the visual cortex (Klimesch 2012). Neuronal activity in the  $\alpha$ -frequency band is associated with relaxed wakefulness (Barry et al. 2007) and selective attention (Klimesch 2012). Moreover,  $\alpha$  waves are instrumental in inhibitory control by filtering out irrelevant information, and facilitating attention and cognitive processes (Knyazev 2007; Klimesch 2012). Palva and Palva's work indicates that cross-frequency phase synchrony between  $\alpha$ ,  $\beta$ , and  $\gamma$  oscillations is crucial for working memory, perception, and consciousness (Palva S and Palva JMatias 2007). Furthermore, deviations from normal alpha wave patterns have been linked to various neurological conditions including depression, anxiety, and ADHD, serving as potential biomarkers (McVoy et al. 2019).

The  $\beta$ - and  $\gamma$ -frequency bands are fundamental within the motor network, serving a critical function in controlling voluntary movements and coordinating motor activities (Engel and Fries 2010; Athanasiou et al. 2018). Changes in  $\beta$  activity have been linked to conditions like Parkinson's disease, underscoring its importance for sustaining motor functionality (Kühn et al. 2009; Schor et al. 2021). A thorough discussion of these frequency bands will be presented in the subsequent section of this introduction.

### 2.3.1 Relevance of beta band activity

The  $\beta$ -frequency band, typically characterized by oscillations within the 16 to 31 Hz span, was initially documented by Hans (Berger 1929). Beta oscillations are a prominent component of neuronal activity across multiple brain areas and species and play a critical role in various cognitive functions, such as attention, sensory perception, and motor control (Pfurtscheller and Da Lopes Silva 1999; Baker 2007; Engel and Fries 2010; Kilavik et al. 2013). Moreover, increased cortical  $\beta$ -band activity has been observed in healthy individuals where it facilitates memory encoding through inhibitory processes (Waldhauser et al. 2012).

Physiological  $\beta$ -band activity has been extensively studied in the sensorimotor cortex (Kilavik et al. 2013) and is crucial for the planning, initiation, and execution of voluntary movements. It is partly generated by corticospinal-projecting pyramidal neurons in the motor cortex (Jackson et al. 2002). In this region,  $\beta$  activity helps maintain the current motor set and suppress unnecessary movements, promoting motor stability, precision, and postural maintenance (Baker et al. 1997; Spinks et al. 2008; Engel and Fries 2010). During movement preparation and execution,  $\beta$  power typically decreases, a phenomenon known as event-related desynchronization (ERD) (Toro et al. 1994), and increases at the cessation of movements ( $\beta$  rebound) (Engel and Fries 2010). This decrease in  $\beta$  activity facilitates motor actions by reducing inhibitory control and allowing greater motor cortex activity (Pfurtscheller and Da Lopes Silva 1999). Conversely, an increase in  $\beta$ -band activity is associated with the successful, voluntary stopping of movement (Jana et al. 2020).

The basal ganglia are another known source of  $\beta$  oscillations (Mirzaei et al. 2017). There is debate over whether these oscillations originate independently in each area or if they are an emergent property of the cortico-basal ganglia networks (Sherman et al. 2016; Reis et al. 2019). LFP activity in the basal ganglia exhibits prominent  $\beta$  oscillations during movement planning, motor plan initiation, reaching and grasping, muscular contraction, and attention tasks (Engel and Fries 2010; Khanna and Carmena 2015; Barone and Rossiter 2021).

The STN is a crucial component of the basal ganglia circuit and demonstrates significant  $\beta$  oscillations. Beta activity in the STN plays a role in controlling motor output and undergoes modulation during movement (Kühn et al. 2008). Research investigating LFP recorded from the STN alongside simultaneous recordings from scalp EEG or MEG has shown that  $\gamma$ - and  $\beta$ -frequency band activities are coherent between cortical sources and the STN (Fogelson et al.

2006; Litvak et al. 2012). Similar to the motor cortex, a reduction in EEG  $\beta$  power during voluntary movements is observed in the STN, which is essential for normal motor function. The  $\beta$  oscillations within the STN are also believed to be involved in coordinating motor commands and inhibiting competing motor actions (Levy et al., 2002). Studies have reported that oscillatory activity in the  $\beta$ -band of the motor cortex can trigger  $\beta$  oscillations in the STN through what is known as the "hyper-direct pathway" (Oswal et al. 2021). Furthermore, it is suggested that  $\beta$ -band oscillations within the STN aids communication and coordination with other structures such as globus pallidus externa (GPe) and substantia nigra pars reticulata (SNr) (Jahanshahi et al. 2015; Aron et al. 2016).

Increased neuronal activity within the  $\beta$ -band, particularly in the basal ganglia, the sensorimotor cortex and the STN, is a significant indicator of movement disorders like Parkinson's disease (PD) (Oswal et al. 2021; Mirzac et al. 2023). While  $\beta$  activity is present in both healthy and pathological states, its precise role remains under debate (Barone and Rossiter 2021). Some studies suggest a functional subdivision within the  $\beta$ -band, with low- $\beta$  (15-20 Hz) in the STN being tightly linked to Parkinsonian symptoms, while high- $\beta$  (25-30 Hz) reflects the coupling between cortical and STN activity (Oswal et al. 2013).  $\beta$  oscillations are greatly enhanced at different sites within the BG circuit in both PD patients and animal models of PD (Kühn et al. 2009; Deffains et al. 2018; Deffains and Bergman 2019). Over recent years, a large body of evidence links pathophysiological  $\beta$ -activity with bradykinesia and rigidity in patients with PD (Kühn et al. 2009; Duchet et al. 2021; Muthuraman et al. 2021; Khawaldeh et al. 2022). Additionally, excessive cortical  $\beta$  oscillations are an indicator of slow-wave sleep dysfunction in mild parkinsonism (Verma et al. 2023). Animal models of Parkinson's disease indicate, that dopamine depletion in the basal ganglia leads to an increase of  $\beta$  power and coherence in the sensorimotor cortex and the STN (Sharott et al. 2005).

Beta oscillations come and go in transient bursts that can be determined on a patient-specific level (Bange et al. 2024). Short  $\beta$ -bursts are an indicator of physiological activity in the motor cortex (Deffains et al. 2018; Torrecillos et al. 2018; Duchet et al. 2021; Lai et al. 2022). However, recent studies proposed that longer bursts with large amplitudes or bursts with characteristic non-linearity are related to bradykinesia in PD (Deffains et al. 2018; Torrecillos et al. 2018; He et al. 2023; Bange et al. 2024).

### 2.3.2 Relevance of gamma band activity

Gamma oscillations typically span a frequency range of 32 to 100 Hz and were first identified in the olfactory bulb (ADRIAN 1950) and visual cortex (Gray et al. 1989). These oscillations are generally more localized in both time and space compared to slower neuronal oscillations, as they reflect the synchronous activation of smaller groups of cells (Mann et al. 2005; Brunet and Fries 2019). Gamma band activity are observed during various states of vigilance, ranging from active behaviour to awake rest, sleep, and anaesthesia (Fernandez-Ruiz et al. 2023). One notable aspect of  $\gamma$ -band activity is its association with emotional processing. Studies have revealed that unpleasant stimuli elicit a stronger response in the lateral-occipital and occipitaltemporal areas of the brain, while pleasant pictures evoke stronger responses in the same frequency range (Yang et al. 2020). The  $\gamma$ -band has also been associated with sensory and cognitive processing (Başar und Güntekin 2008), attention, long-term memory, and language (Başar and Güntekin 2008; Abreu et al. 2018); Jerbi et al. 2009; Paller et al. 1987). Furthermore,  $\gamma$ -band activity has been implicated in the coordination of information processing across distributed brain regions (Yang et al. 2020). Emotion, being a complex cognitive function, requires the cooperation of multiple brain areas, and the  $\gamma$ -mediated synchronization of neuronal ensembles may facilitate this integration. Increased EEG  $\gamma$  power may indicate major depressive disorder and could potentially be used to differentiate between bipolar disorder and depression (Fitzgerald and Watson 2018). Cortical  $\gamma$  oscillations are thought to arise from the simultaneous activation of excitatory pyramidal neurons and inhibitory interneurons (Nowak et al. 2018). These oscillations are a prominent feature of the motor cortex and are associated with various motor functions and cognitive processes. They play an important role in motor control, including motor planning, execution, and coordination of movements (Nowak et al. 2018). They are particularly prominent during voluntary movements and motor (Miller KJ. et al. 2007; Smith et al. 2014; Salvadè et al. 2016; Thürer et al. 2016). Research has shown an increase in oscillatory activity in the  $\gamma$ -frequency band during movement (Nowak et al. 2018). In contrast to  $\beta$ -band activity, cortical  $\gamma$  activity is considered prokinetic in nature (Muthukumaraswamy 2010; Jenkinson et al. 2013). Additionally, the role of  $\gamma$  oscillations in motor imagery tasks is

particularly intriguing, as they appear to be heavily involved in the "goal-driven executive control" of imagined movements (Jahangiri and Sepulveda 2018).

Gamma oscillations are involved in the synchronization of different regions of the motor cortex and between the motor cortex and other brain areas involved in motor control, such as the basal ganglia and cerebellum. Multiple studies have shown that alterations in  $\gamma$ -band activity in the motor cortex are associated with motor disorders such as Parkinson's disease, dystonia, and epilepsy. Dysregulation of  $\gamma$  oscillations can disrupt normal motor function and contribute to the manifestation of motor symptoms. For example, an increase in  $\gamma$ -band activity in the motor cortex is associated with dyskinesia in Parkinson's disease patients (Olaru et al. 2024) as well as animal models of Parkinson's disease (Salvadè et al. 2016; Grandi et al. 2018)

## 2.4 High frequency stimulation of the STN

Deep brain stimulation (DBS) is a surgical treatment that has been used to treat a variety of neurological disorders, including Parkinson's disease, essential tremor, dystonia, epilepsy, chronic pain, and obsessive-compulsive disorder (Dorval et al. 2010; Xie P et al. 2023). DBS involves implanting electrodes in specific areas of the brain and then connecting them to a pulse generator, which delivers electrical stimulation to the brain (Deuschl et al. 2013). This targeted stimulation causes the modulation of the activity of specific neural circuits involved in the pathogenesis of the disease. A variety of targets have been tested and are being used to treat different diseases, e.g. globus pallidus interna (Dorval et al. 2010), the thalamus, the subthalamic nucleus (Gonzalez-Escamilla et al. 2022), the nucleus accumbens or the ventral capsule/ventral striatum. The therapeutic benefits of high frequency DBS resemble those obtained from surgical lesions in the same brain regions (Lozano et al. 2019). However, DBS possesses several advantages over other surgical approaches for neuromodulation, namely its adjustability and reversibility (Okun and Vitek 2004). For example, DBS can safely be implanted bilaterally, while bilateral lesioning often results in unacceptable side effects. As a scientific tool, DBS enables the investigation of the physiological basis of brain dysfunction, facilitating the identification and correction of pathological neuronal signatures, and driving technological innovation to enhance safety and clinical outcomes (Kühn et al. 2008).

Although over 160,000 patients worldwide have undergone DBS for a variety of neurological and non-neurological conditions, the precise mechanisms of action remain unclear (Lozano and Lipsman 2013; Gonzalez-Escamilla et al. 2022).

DBS is most commonly applied in the treatment of movement disorders, especially in Parkinson's disease (Lozano et al. 2019). The STN is a key target for DBS in Parkinson's disease, as this structure is known to play a central role in the dysfunctional basal ganglia circuitry that underlies the motor impairments characteristic of PD (Lozano et al. 2019). It can alleviate tremor, bradykinesia, dyskinesias and rigidity and can enable a reduction in medication dose (Deuschl et al. 2013; Gonzalez-Escamilla et al. 2022), this leads to a significant improvement in the quality of life for the patients. Numerous studies in both animal models and human patients have demonstrated the efficacy of STN DBS (Kühn et al. 2008; Schor and Nelson 2019; Shin et al. 2023).

High frequency stimulation (HFS) of the STN was observed to reduce the firing activity of STN neurons (Vissani et al. 2021), which causes inhibition in the SNr and activation in GPe neurons during and after a stimulus (Benazzouz et al. 1995). The decreased activity in SNr neurons induces disinhibition of motor thalamic nuclei, which in turn leads to increased activity in motor cortical areas (Benazzouz et al. 2000). Several studies observed an inhibition of STN activity during STN-stimulation; however, there are also studies showing an increase in STN activity during STN DBS (Galati et al. 2006). This is in line with a study by Li et al. (2007), who reported changes in membrane potential and spiking activity in neurons located in several layers of the mouse motor cortex with STN stimulation.

DBS of the STN has been shown to normalize pathological neuronal activity and restore normal motor function (Li et al. 2007; Schor et al. 2022). It has been shown that STN DBS can reduce  $\beta$ -band activity in the motor cortex (Li et al. 2007; Schor et al. 2022). Similarly, in patients with Parkinson's disease, STN DBS has been found to modulate abnormal  $\beta$ -band oscillations associated with the disease, leading to significant improvements in motor symptoms (Boëx et al. 2023). Oswal et al. (Oswal et al. 2016; Oswal et al. 2021) showed that cortical areas are leading the STN activity specifically in high  $\beta$ -band power in Parkinson's disease patients and during STN stimulation. The effect of STN stimulation on oscillations in the  $\gamma$ -band is also recognized (Trottenberg et al. 2006).

However, given inconclusive outcomes in previous studies concerning the impact of STN

DBS, how STN DBS induces improvements in motor function remains unclear (Moran et al. 2011; Li Q et al. 2012; Chiken and Nambu 2014; Johnson LA. et al. 2020). It is thought to work by disrupting abnormal signalling in the basal ganglia, a network of brain structures that are involved in movement control. Currently, there are three principal hypotheses under scrutiny (Hashimoto et al. 2003; Chiken and Nambu 2014; Schor et al. 2022): (1) STN-DBS inhibits STN activity restoring normal function; (2) STN-DBS modulates cortical neurons via antidromic activation facilitated by the hyperdirect pathway; or (3) STN-DBS disrupts pathological activity within the STN and interconnected regions. The mechanism of action likely involves an interaction of various effects. As mentioned by recent studies (Gonzalez-Escamilla et al. 2022), STN stimulation not only modulates neural activity within the STN itself but also triggers activation of adjacent fiber tracts, consequently influencing more than one basal ganglia-cortical circuits (Li et al. 2007; Gonzalez-Escamilla et al. 2022).

The STN is a crucial element in controlling movement. However, the specific ways in which it interacts with other regions of the brain and its contributions to motor control are not fully understood. Deep brain stimulation of the STN is a standard treatment for Parkinson's disease and other movement disorders. However, the effect it has on the Rostral Frontal Area (RFA), Caudal Frontal Area (CFA), and STN network remains unclear. As these regions are vital for motor function, it is essential to understand how STN stimulation affects their interactions.

Therefore, the second aim of this study is to investigate the impact of high frequency STN stimulation on the RFA-CFA-STN network.

Understanding the effects of STN DBS on healthy neuronal networks is essential to deciphering its effect on the pathological state of PD. Moreover, the description of the frequency-dependent layer-specific effects of DBS is almost completely lacking, thereby hampering the development of effective closed-loop interventions as well as impeding its use for brain-computer interface developments in humans.

## 2.5 Aims of the thesis

I aimed to analyze the effect of high frequency STN stimulation on the premotor-motor-STN network in wildtype mice.

To this end, the first step was analyzing the properties of and the connectivity between the two motor cortical areas RFA and CFA in wildtype mice (Aim1).

By collaborating with Prof.Dr.-Ing Muthuraman Muthuraman (Section of Movement Disorders and Neurostimulation, Biomedical statistics and multimodal signal processing unit, Department of Neurology, University Medical Center of the Johannes Gutenberg University Mainz, Mainz, Germany), I was able to compare the results gathered from the mouse motor cortex data, with data recorded in healthy humans at rest. This collaboration allowed me to address the following questions:

Aim 1.1:

Are the two mouse motor cortex areas, the RFA and CFA, electrophysiologically distinct?

Aim 1.2:

What are the features of functional and effective connectivity between the RFA and CFA?

Aim 1.3:

Can the connectivity of the RFA-CFA network be used as a valid model for the human PMC-M1 network?

Second, I answered the question of how high frequency STN stimulation influences the RFA-CFA STN network (Aim 2).

Aim 2.1:

Does high HFS of the STN influence the layer-specific activity in RFA, CFA and STN?

Aim 2.2:

Does HFS of the STN influence the bursting activity in the  $\beta$ -frequency band in RFA, CFA and STN?

Aim 2.3:

How does HFS of the STN influence the layer-specific bursting activity in the  $\gamma$ -frequency band in RFA, CFA and STN?

Aim 2.4:

Does HFS of the STN influence the layer-specific synchronization between RFA and CFA in the  $\beta$  and high  $\gamma$ -frequency band?

Aim 2.5:

Does HFS of the STN affect the layer-specific effective and functional connectivity between the RFA, the CFA, and the STN?

By answering these questions, I aim to make a valuable contribution to better understanding the mechanism of action of STN stimulation.

### 3 Materials and Methods

#### 3.1 Animals

All animal experiments were done in accordance with National and European (European Communities Council Directive, 86/609/EEC) laws for the use of animals in research and were approved by the local ethical committee (Landesuntersuchungsamt Rheinland-Pfalz, TVA #23 177-07/G 19-1-081 and #23 177-07/G 14-1-080). Male C57BL/6NCrl wild-type mice (Charles River Laboratory, USA) were used for all experiments. 8- to 16-week-old (24-32g) mice were obtained from the Translational Animal Research Center (TARC, Mainz, Germany) or Charles River Laboratory (Wilmington, USA) and housed in the Institute of Physiology, University Medical Center of the Johannes Gutenberg University Mainz (Mainz, Germany) facility. Mice were kept at a 12-hour dark/light cycle and received standard food and water at libitum. In total 26 mice were used. 21 mice were included in the analysis. Four recordings had to be excluded due to incorrect placement of the STN electrode. One recording had to be excluded due to a low signal-to-noise ratio.

#### 3.2 Surgery

All experiments were performed in anaesthetized animals. For craniotomy preparation, anaesthesia was initialized by inhalation of 3.0 % isoflurane (AbbVie Inc., Illinois, USA) in air. Anaesthesia was maintained with 1-2 % isoflurane and an i.p. injection of 1 mg/g Urethane in Ringer solution. During the surgical preparation and electrophysiological recordings, the mice were placed on a heating pad (37 °C) to prevent hypothermia. The depth of anaesthesia (surgical tolerance stage) was assessed preoperatively and intraoperatively by monitoring the absence of the tail and inter-toe reflex, the eyelid reflex and the respiration rate. Lidocaine gel (Aspen Germany GmbH, München; Germany) was applied to the skin in the area of the incision before the surgery to avoid any pain during the incision. Eyes were covered with eye ointment (Bepanthen Augen- und Nasensalbe, Bayer, Leverkusen;

Germany) to prevent dryness. After removing the skin from between the ears to between the eyes a custom-made head holder was glued onto the skull using acrylic glue. This allowed stable fixing of the animal's head in a suitable frame. A small hole was drilled over the cerebellum and a silver wire was implanted into the cerebellum as a reference electrode. Subsequently, two cranial windows were prepared by skull thinning under a dissecting microscope using dental drills. It is essential to avoid damaging the dura, as this would lead to brain damage and drying of the cortex during the long recording session. The first craniotomy was performed over the front paw representation of the motor cortex; the second was performed to allow for the insertion of the STN recording electrode (Figure 2). Because of the size of the multi-electrode array (MEA) head stages, the STN recording electrode could not be positioned over the same hemisphere as the two motor cortex recording electrodes, which would have allowed a vertical insertion of the MEA. However, since it is essential to stimulate the STN and record its neuronal activity in the same hemisphere as recording cortical activity, the electrode was inserted at a 52° angle from the contralateral hemisphere.

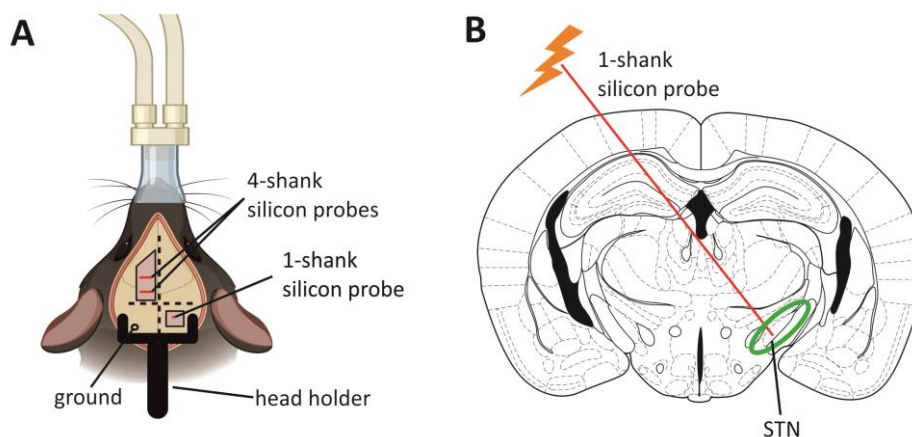


**Figure 2: Schematic overview of the area of interest for MEA recordings.** (A) Schematic overview of the surgery, including the position of the head holder (black), position of the craniotomies (pink) and position of the reference and recording electrodes (red) (Created in <https://BioRender.com>). (B) Schematic view of a brain slice containing the STN(right) (Paxinos and Franklin 2019); green ellipse marks the location of the STN; the red lines represent the electrode tracks.

### 3.3 Electrophysiological recordings

After the surgery was complete, the animal was transferred to the recording setup, and the isoflurane anaesthesia was discontinued. This is necessary since isoflurane anaesthesia has been shown to reduce neural activity, especially in cortical areas and to modulate the functional connectivity between multiple brain areas (Williams et al. 2010; Bukhari et al. 2018; Paasonen et al. 2018). Extracellular MEA recordings were performed simultaneously in the STN and all layers of RFA and CFA. To this end three MEAs were coated with a fluorescent lipophilic dye (DiI, D282, Invitrogen) and slowly inserted into the areas of interest, using a motorized micromanipulator. Firstly, a 32-channel MEA with a single shank configuration (A1x32, 50  $\mu\text{m}$  vertical distance between contacts; Neuronexus, Ann Arbor, Michigan, USA), was inserted into the STN at a 52° angle in 10  $\mu\text{m}$  steps, the final coordinates of the electrode tip were -1.7 mm anterior-posterior, 1.5 mm medial-lateral, and 4.5 mm dorsal-ventral (Paxinos and Franklin 2019). The correct placement of the STN electrode was estimated at the beginning of each recording session by assessing the distinct activity patterns characteristic of the STN. After the STN electrode was placed successfully, two 32-channel MEAs with a 4-shank configuration (A4x8-A32, 100  $\mu\text{m}$  vertical distance between contacts; 200  $\mu\text{m}$  horizontal distance between shanks; Neuronexus, Ann Arbor, Michigan, USA) were gradually inserted into the RFA (2.5 mm anterior-posterior, 1.2 mm medial-lateral) and CFA (0.5 mm anterior-posterior, 0.8 mm medial-lateral) to a maximum depth of 0.8 - 1 mm, following established coordinates (Tennant et al. 2011). This electrode layout allows to record from several contacts in each cortical layer.

After electrode placement, a stabilization period of approximately 30 min allowed the brain tissue to settle and build strong contacts with the recording electrodes. This leads to an increase in signal-to-noise ratio. During this interval, any residual effects of isoflurane dissipated, ensuring that the subsequent electrophysiological recordings were conducted under pure urethane anaesthesia. Pure Urethane anaesthesia ensures conditions are as close as possible to the non-anaesthetized settings. Urethane application leads to stable long-lasting anesthesia (Soma 1983; Maggi and Meli 1986). Urethane has been shown by multiple studies to be a suitable anaesthetic regime for long recordings of spontaneous neuronal activity (Maggi and Meli 1986; Sceniak and Maciver 2006; Devonshire et al. 2010; Masamoto and Kanno 2012). The influence of urethane on neuronal discharge patterns,

neurotransmitter receptors, and synaptic interactions is minimal (Hara and Harris 2002). The functional connectivity pattern under urethane anaesthesia is similar to the non-anaesthetized state, with a particularly robust preservation of cortical and thalamocortical connectivity (Paasonen et al. 2018). During the electrophysiological recordings, anaesthesia depth was monitored using indicators such as breathing rate and the presence or absence of the toe pinch reflex.

All electrophysiological signals were recorded at a sampling rate of 20 kHz using the ME2100 system (multi-channel systems, Reutlingen, Germany). The first recording of each recording session was a 10-minute segment of spontaneous neuronal activity ('stim off') in order to establish the baseline activity in and connectivity between the analyzed brain areas for subsequent analyses. Subsequently, STN stimulation was applied to two contacts located within the STN with varying frequencies (50, 100-200 Hz in 10 Hz steps) in a burst with a duration of 400 ms. I varied the stimulation frequency while holding the current amplitude and pulse width constant (-25  $\mu$ A and 60  $\mu$ s monopolar, square waves, see Figure 3D). The number of individual pulses is determined by the stimulation frequency. The choice of the -25 mA stimulation amplitude was based on the electrode's resistance and a balance between achieving effective stimulation while minimizing the stimulation artefact. During the first experiments, multiple stimulation intensities were tested. When analyzing the early experiments, -25  $\mu$ A stimulation intensity was identified to be sufficient to elicit noticeable changes in the STN-motor network without causing tissue damage. Therefore, all future experiments were performed using this stimulation intensity. The stimulation setting was designed to mirror the typical DBS settings used in humans and rodent models (Li Q et al. 2012; Brocker et al. 2017; Schor and Nelson 2019; Knorr et al. 2022; Schor et al. 2022), however, due to the stimulation artefact, it was not possible to apply continuous stimulation. Therefore, a burst stimulation approach was chosen with an inter-stimulus interval of 7 s. Each STN stimulation recording lasted 10 minutes, comprising 81 trials, followed by a 10-minute recording of spontaneous activity ('stim off') to eliminate potential effects from the preceding stimulation frequency on subsequent recordings. The stimulating contacts are chosen based on the location within the STN. Since it is not reliably possible to determine the exact electrode location during the recording, post-mortem histology is necessary to identify the exact electrode location (Figure 3). For each recording session, the

order in which the different stimulation frequencies were applied was determined randomly. A representative recording of both spontaneous neuronal activity and the responses during 160 Hz stimulation is shown in Figure 10. The stimulation contacts were chosen based on the location within the STN. Since it is not reliably possible to determine the exact electrode location during the recording, post-mortem histology is necessary to identify the exact electrode location (Figure 4).

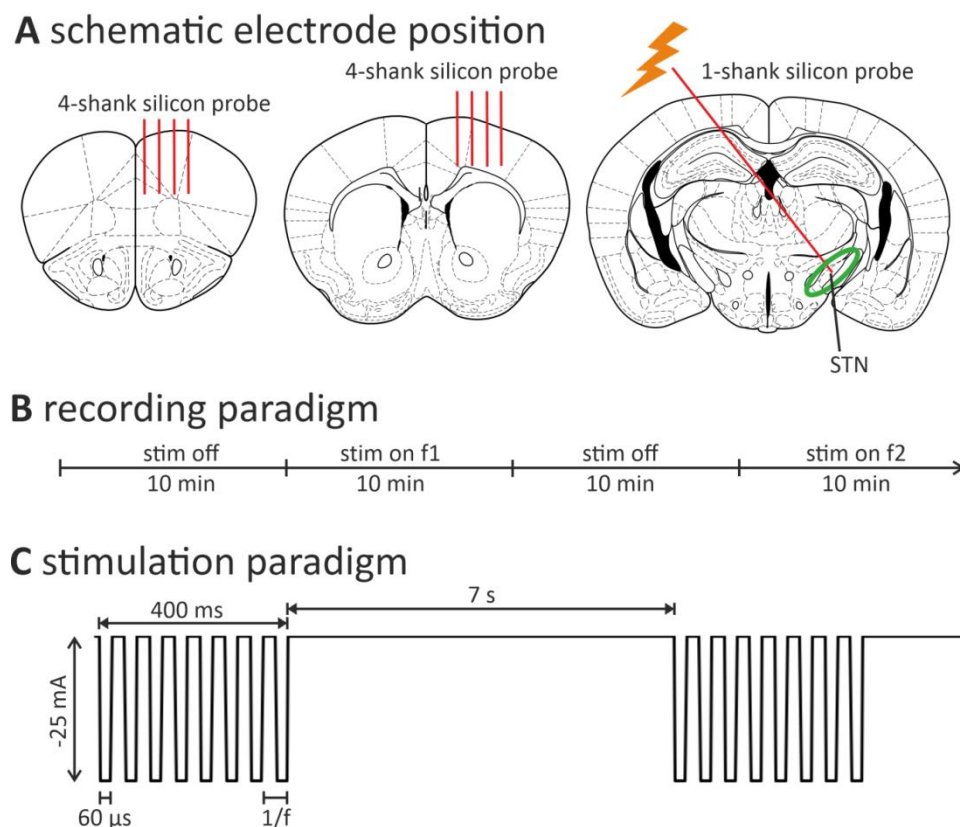


**Figure 3: Schematic representation of a recording session.**

(A) Schematic view of a brain slice containing the RFA (left) CFA (middle) and STN(right) (Paxinos and Franklin 2019); green ellipse marks the location of the STN; the red lines represent the electrode tracks. (B) Schematic representation of the recording regime, showing 10 min of recording without stimulation followed by 10 min of STN stimulation. (C) Details representation of the STN burst stimulation paradigm.

### 3.4 Tissue preparation and Immunohistochemistry

All animals were sacrificed after electrophysiological recordings. After the experiment, animals were deeply anaesthetized with urethane (2 mg/g) or xylazine hydrochloride (30 mg/kg) and transcardially perfused with cold PBS. The brain was carefully removed and submerged in cold 4% PFA for overnight fixation at 4°C. The fixation of tissues with aldehydes (in this case using paraformaldehyde, PFA) serves to prevent the autolytic process of enzymes and the denaturation of proteins in the examined preparation in order to ensure the best possible preservation of cellular structures. The brains are then washed several times in 0.01 M PBS on an oscillating shaker to remove all residues of the PFA. The fixed brains were prepared for cryosections with incubation in 10% sucrose dissolved in PBS for 12 hours, then replaced by 30% sucrose in PBS overnight. Next, the brains were quickly frozen and histological brain slices of 200 µm thickness were prepared using a freezing microtome (Leica, Wetzlar, Germany). The cryosections are then collected directly on microscope glass slides. After thawing, cryosections were stained for 30 min without movement at RT with Sytox Green Nucleic Acid Stain (Invitrogen, 0.1µM) diluted in PBS.

### 3.5 Analysis of Electrophysiology

The analysis in this study is primarily divided into two distinct sections, each addressing specific aspects of the research objectives: The first section involves the examination of spontaneous neural activity within the RFA and CFA, along with an exploration of the functional connectivity between these regions (Aim 1). To achieve this, 10 min segments of spontaneous neuronal activity were analyzed.

The second section was the investigation of the impact of STN stimulation on neural activity in, and the connectivity between RFA, CFA and STN (Aim 2). To this end, the last 10 trials of each recording with stimulation were analyzed, and the intervals from 2 seconds after the stimulus onset until the onset of the subsequent burst were selected. This led to the derivation of a 5-second data segment for each trial. This approach facilitated the exclusion of the stimulation artefact from the analysis. Trials of identical length were analyzed from the end of the first recording of spontaneous recording to be compared to the 'stim on' condition. Additionally, one segment of spontaneous activity recorded in the middle, and at

the end of each recording session was analysed, to ensure the stability of the recording throughout the several hour-long recording.

### 3.5.1 Raw data processing

Data analysis was performed using the FieldTrip toolbox (Oostenveld et al. 2011) and self-written scripts in MATLAB (version 2019b; Mathworks, Natick, MA, USA). Firstly, the recorded raw signal was divided into local field potential (LFP) data and multi-unit activity (MUA). For LFP data, the recorded signals were high-pass filtered at 0.1 Hz and low-pass filtered at 250 Hz. Additionally, the recorded wide-band signals were high-pass filtered (0.3–3 kHz) for spike detection and MUA analysis. For a comprehensive analysis, the complete sampling rate of 20 kHz was used to analyze spectral power, LFP coherences, spike detection, sorting, and single unit (SU) analysis. For time-resolved partial directed coherence (tPDC) and  $\beta$ - and  $\gamma$ -burst analysis, data was down-sampled to 200 Hz (tPDC) and 300 Hz ( $\beta$ - and  $\gamma$ -burst analysis). For in-depth analysis of spectral power, coherence, and tPDC results were separated into the different frequency bands, namely delta (0-3 Hz), theta (4-7 Hz), alpha (8-15 Hz),  $\beta$  (16-31 Hz), low gamma (32-49 Hz), medium gamma (51-75 Hz), and high gamma (76-100 Hz).

All data presented in section 4.1 (Premotor-motor network in the mouse motor cortex) was calculated from a continuous 10-minute recording, performed simultaneously in RFA and CFA at the beginning of each recording session.

The data presented in section 4.2 (Effect of high frequency stimulation in the RFA-CFA-STN network), was calculated from multiple 5 s segments, starting 2s post-stimulus onset until the onset of the next stimulus.

I evaluated the final 10 stimulation trials for each stimulation frequency and selected the intervals starting 2 seconds after stimulus initiation until the onset of the subsequent burst, resulting in a 5-second data segment for each trial (Figure 10). This approach enabled me to exclude the stimulation artefact from the analysis. To compare recordings with and without STN stimulation, I analyzed spontaneous activity segments of equivalent duration and spacing.

I chose to analyse the last 10 trials of each stimulation frequency since I noticed an increase in effect on the RFA-CFA-STN network throughout the 10 min recording during preliminary analysis. This is in line with results in PD patients, who show continuous improvement of the symptoms after the stimulation onset in humans (Muthuraman et al. 2020). Rigidity and bradykinesia improve in the first 10-20 seconds after stimulation onset. A recent study, that analysed the electrophysiological primers of these clinical effects, showed an involvement of  $\beta$  to narrow-band  $\gamma$  synchronization that rises over ca 60 seconds to achieve a plateau (Muthuraman et al. 2020). These cross-frequency effects were related to the bradykinesia improvement in patients.

### 3.5.2 Local Field Potential Power

LFP power was determined through a multitaper frequency transformation approach, by applying the `ft_freqanalysis` script in Fieldtrip (Oostenveld et al. 2011). Initially, the recorded signals underwent high-pass filtering at 0.1 Hz and low-pass filtering at 250 Hz to extract the local field potential from the raw recording. To further mitigate 50 Hz noise interference, additional notch filtering at 50, 100, and 150 Hz was applied. Sub-harmonics like 25 Hz or 12.5 Hz are less likely to be directly related to powerline interference. The recorded neuronal signals exhibit dominant frequencies in the lower range (e.g.,  $\theta$ ,  $\alpha$ ,  $\beta$ ), which are distinct from the harmonic frequencies of powerline noise. Therefore, these sub-harmonics were not removed from the signal to avoid the risk of over-processing the signal and potential distortion or elimination of genuine neural activity.

The spectral power computations were performed on 500 ms segments spanning the frequency range of 0.1-100 Hz, with a step size of 0.25 Hz. The resulting spectra were sorted to the area and layer of the recording, pooled across all subjects, and subsequently partitioned into distinct frequency bands. The resulting spectra are presented in Figure 6 and Figure 17.

In order to compare the power spectrum with and without STN stimulation in section 4.2 (Effect of high frequency stimulation in the RFA-CFA-STN network), I performed linear normalization to maximum and minimum power in the range of 0-100 Hz.

The power spectrum in section 4.1 (Premotor-motor network in the mouse motor cortex) was not normalized to ensure comparability between RFA and CFA.

The resulting power spectra were averaged across the different frequency bands, namely delta (0-3 Hz), theta (4-7 Hz), alpha (8-15 Hz), beta (16-31 Hz), low gamma (32-49 Hz), medium gamma (51-75 Hz), and high gamma (76-100 Hz). The resulting boxplots are presented in Figure 6 and Figure 18.

### 3.5.3 Beta and gamma-burst detection

The detection of  $\beta$ - and  $\gamma$ -bursts was carried out in accordance with the methods outlined by Tinkhauser et al. (2017). Initially, the raw signal was filtered using high-pass and low-pass filters to isolate the LFP signal, with a cutoff frequency of 0.5 Hz and 250 Hz, respectively. The data was then resampled to a rate of 300 Hz and subjected to wavelet transformation to identify frequency components within the range of 13-30 Hz ( $\beta$ -bursts) and 76-100 Hz ( $\gamma$ -bursts), with a frequency resolution of 1 Hz. Next, the peak frequency of each  $\beta$ - or  $\gamma$ -burst was selected, and the corresponding wavelet amplitude was smoothed over a period of 0.2 seconds. A burst was detected if the signal crossed a threshold defined as the 75th percentile of the amplitude distribution for at least 100 ms. The number, duration, and amplitude of both  $\beta$ - and  $\gamma$ -bursts were analyzed. The resulting data for the  $\beta$ -band is shown in Figure 19 and for the  $\gamma$ -band in Figure 21.

To further examine the distribution of bursts, I categorized the detected bursts based on their duration using the following bin sizes 100 to 225 ms, 225 to 350 ms, 350 ms to 475 ms, 475 ms to 600 ms, 600 to 725 ms, 725 to 800 ms, and longer than 800 ms. All bursts with a duration of more than 600 ms are considered long bursts.

### 3.5.4 Functional connectivity analysis

To assess functional connectivity between layers 2/3, 5, and 6 of RFA, CFA, as well as STN, I conducted an analysis of LFP coherence between every pair of recording electrodes for each area and subject. In summary, the raw signal underwent precise bandpass filtering within the frequency range of 0.5 to 250 Hz. Next, the spectral coherence was calculated for frequencies between 0.5 and 100 Hz with a step size of 0.6 Hz. The resulting coherence was

split into layers and frequency bands and pooled for all animals. Significance testing was carried out via a surrogate analysis, employing a Monte Carlo random permutation method involving 100 iterations, where 50 ms segments within each subject's data were shuffled. These surrogates were designed to maintain the same mean, variance, and histogram distribution as the original signal while erasing any temporal structure.

### 3.5.5 Effective connectivity

#### Spike sorting

Spike detection and sorting were conducted utilizing WaveClus 3 (Chaure et al. 2018). The continuously recorded wide-band signals underwent a high-pass filter (0.3–3 kHz). Spike detection was performed independently for each channel, by employing amplitude thresholding within the negative amplitude range. The threshold level was individually set for each channel at 5 times the standard deviation (SD) of the signal. Peaks exceeding 30 SD of the noise level were identified as artefacts and subsequently excluded.

Upon detecting a threshold crossing, all sampled amplitude values from this channel within the time window of  $-0.5$  to  $+3$  ms relative to the negative peak were extracted. Feature extraction involved selecting wavelet coefficients based on a Kolmogorov-Smirnov test of Normality (Quiroga et al. 2004). Super-paramagnetic clustering was employed to define single-unit (SU) clusters. SPC relies on simulated interactions between each data point and its K-nearest neighbours, implemented as a Monte Carlo iteration of a Potts model (for a detailed explanation, see Quiroga et al. (2004)).

Following automated clustering, outliers were removed from the single units utilizing the FieldTrip toolbox (Oostenveld et al. 2011). Subsequently, the quality of the SUs was assessed using the MLIB toolbox (Maik Stüttgen 2020). Incomplete separations or unstable SUs were excluded from the analysis.

#### Time-resolved partial directed coherence (tPDC)

The time-resolved partial directed coherence analysis is a powerful technique that allows to investigate the directional and time-varying relationships between multiple time series data, such as brain signals or physiological measurements. This method builds upon the traditional

partial directed coherence analysis, which has been widely used in various fields, including neuroscience, finance, and engineering (Dichter et al. 2015). The time-resolved partial-directed coherence analysis involves sliding a time window over the input data and calculating the partial-directed coherence within each window, providing a detailed understanding of how the directional relationships between the time series evolve over time (Rad et al. 2014). This approach is particularly useful for studying dynamic interactions between different brain areas, as it enables the measurement of the directional information transfer between different areas of the brain in both time and frequency domains (Leviashvili et al. 2022).

The time-frequency causality estimation method of temporal partial directed coherence is based on dual-extended Kalman filtering, which allows for the estimation of time-dependent autoregressive coefficients. One extended Kalman filter estimates the system states and provides this information to a second extended Kalman filter that estimates the model parameters, sharing the information between the two. Using two Kalman filters in parallel enables the estimation of the states and model parameters of the system at each time point. Time-dependent multivariate coefficients were used to calculate the causality between the time series, and the time-dependent multivariate autoregressive coefficients were used to calculate the partial directed coherence at each time point. A details description of the tPDC analysis is described elsewhere (Muthuraman et al. 2012).

To reduce the intensive computational power required by this tPDC method, the LFP data was down-sampled to 200 Hz before applying the tPDC analysis (Muthuraman et al. 2018). Additionally, we chose one channel per layer and animal, based on the highest power. The resulting data was separated into the different frequency bands and pooled for all analysed animals. Significance was tested by means of the time-reversal technique (Haufe et al. 2013).

### 3.5.6 Statistical analysis

All statistical analysis was performed in MATLAB (version R2019a, Mathworks, Natick, MA, USA). In the first and second sections of this thesis (Results sections 4.1 and 4.2), an explorative approach was used to investigate the region-, layer-, frequency-, and direction-specificity of the neuronal signals in RFA, CFA and STN. To achieve this, a total of 16 mice were employed to investigate the activity and connectivity between the RFA and CFA.

Additionally, nine mice had appropriately placed STN electrodes. Data obtained from these nine mice was utilized to analyze the connectivity between the STN and both cortical regions, as well as the impact of high frequency STN stimulation on the connectivity within the RFA-CFA-STN network (Results sections 4.2). The second part of the thesis aimed to explore the influence of high frequency STN stimulation on the RFA-CFA-STN network through a hypothesis-driven approach. For each animal, between 3 and 12 electrode contacts were recorded from each area or layer of interest. Data from multiple contacts within one animal was treated as repeated measures. To account for intra-animal correlation, linear mixed-effects models (LMM) were used to identify significant effects. Additionally, two-sampled t-tests were performed for LMM results that showed significant effects of specific factors. All post-hoc tests were Bonferroni corrected to account for multiple comparisons, such as different layer combinations or frequency bands.

### 3.6 Microscopy and image processing

All Microscope images were performed using an inverse light microscope (Olympus). First, the Dil- traces left by the electrode were located in the brain slice. Then two images are taken, without shifting the position of the microscope. The first contains the Dil signal and the second contains the green fluorescence signal from the Sytox green staining. For the Sytox Green Nucleic Acid Stain, a 488nm laser was used for excitation and a 525/50 emission filter was used. Next, the whole brain slice is imaged in sections by taking slightly overlapping images. Images were acquired with magnifications varying from 4x to 10x.

Afterwards, the original TIF files were imported into Adobe Photoshop for automated stitching. The exact electrode position can be reconstructed, by overlaying the first two images of each slice, containing the Dil signal and the Sytox-Green signal of the identical location. Examples of reconstructed slices showing the electrode track are presented in Figure 4.

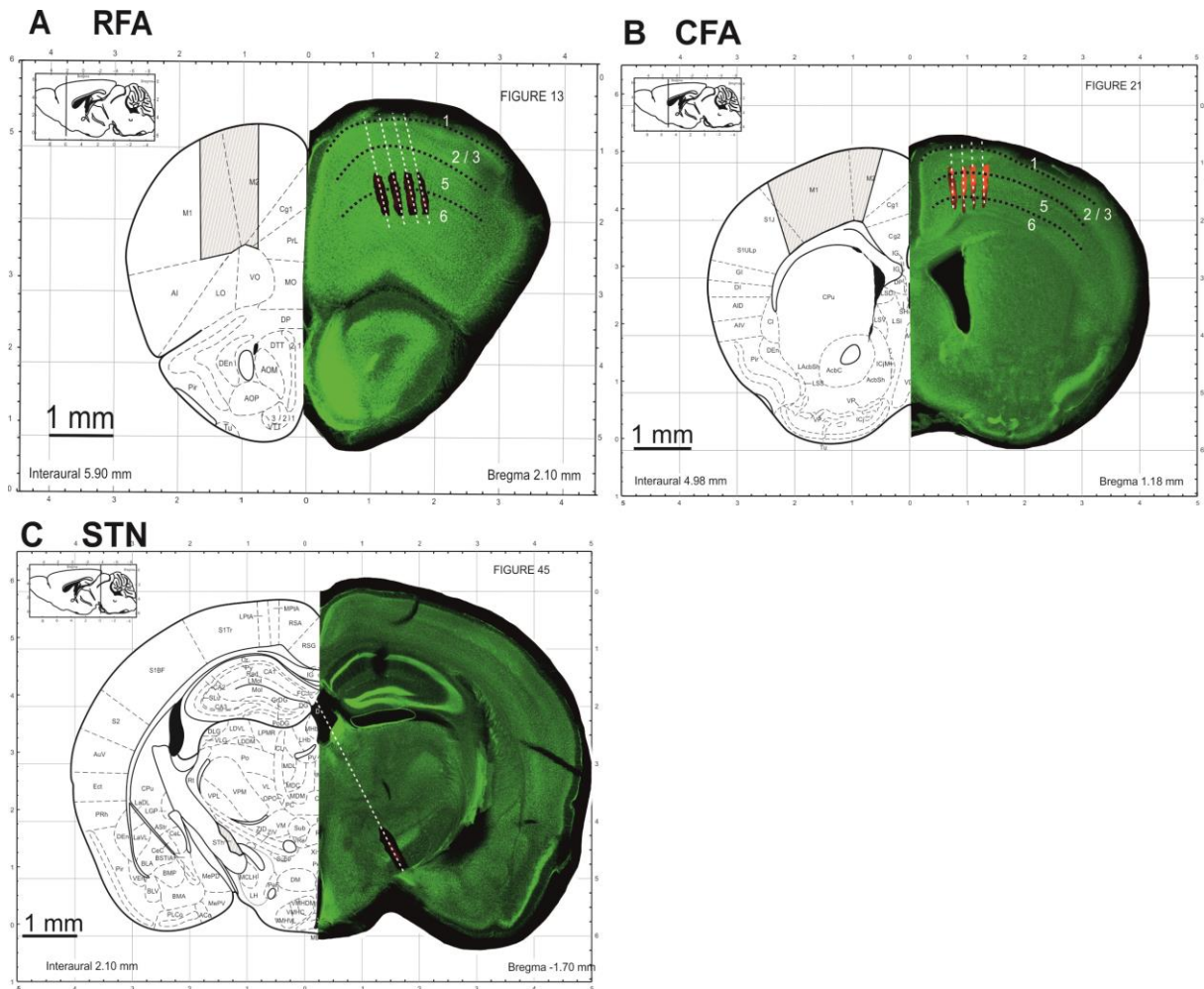


**Figure 4: Reconstruction of MEA localization.**

Localization and configuration of the MEA for simultaneous recordings in the RFA (A), CFA (B) and STN (C) of an adult C57Bl6-N mouse *in vivo*. The left panels of (A) and (B) are adapted from Paxinos and Franklin (2019), shaded areas indicate RFA, CFA and STN; the right panels show Sytox green staining. Black dotted lines indicate cortical layers 1-6 indicate cortical layer; white dashed lines indicate tracks of the MEAs.

Next, the cortical layers were identified using the reconstructed images, this enabled me to identify the exact location of each contact of the electrodes. Thereby make a layer-specific analysis possible. In order to confirm the correct placement of the STN stimulation electrode, I overlaid the reconstructed image with the corresponding map from a mouse brain atlas (Paxinos and Franklin 2019).

## 4 Results

High frequency stimulation (HFS) of the subthalamic nucleus (STN) is an evidence-based and highly effective therapeutic option for patients with Parkinson's disease (PD) with motor fluctuations (Deuschl et al. 2013; Gonzalez-Escamilla et al. 2022). However, the underlying mechanisms are not thoroughly understood (Moran et al. 2011; Deuschl et al. 2013; Chiken and Nambu 2014; Gonzalez-Escamilla et al. 2022). The first step to deciphering the effect of HFS of the STN in PD patients would be understanding the motor cortex network in healthy subjects. This is commonly done by using animal models, e.g. mouse models. Therefore, understanding the physiological patterns of motor network connectivity is a prerequisite to elucidate aberrant oscillatory transformations and elaborate robust translational models of movement disorders.

### 4.1 Premotor-motor network in the mouse motor cortex

The rostral forelimb area (RFA) and caudal forelimb area (CFA) are two motor cortex areas in mice that have been proposed as a suitable model for the human premotor-motor network. To validate this proposal, I simultaneously recorded spontaneous neuronal activity in layers 2/3, 5, and 6 of RFA and CFA in lightly anaesthetized mice in vivo. This careful investigation aimed to clarify the degree of comparability and functional equivalence between these mouse motor cortex areas and their human counterparts, thereby making a significant contribution to our understanding of motor network dynamics (Aim 1).

#### 4.1.1 Spontaneous activity in the mouse motor cortex

Firstly, I wanted to answer the question of whether the two mouse motor cortex areas RFA and CFA are electrophysiologically distinct areas (Aim 1.1). To this end, I addressed the question of whether RFA and CFA show differences in their spontaneous neuronal activity. Therefore simultaneous recordings of 10 min of spontaneous neuronal activity were performed in layers 2/3, 5, and 6 of the RFA and CFA in lightly anesthetized mice in vivo. To analyze the data, the recordings were separated into local field potential (LFP; 0.1-250 Hz) and multi-unit activity (MUA; 0.3–3 kHz) by filtering for the relevant frequencies.

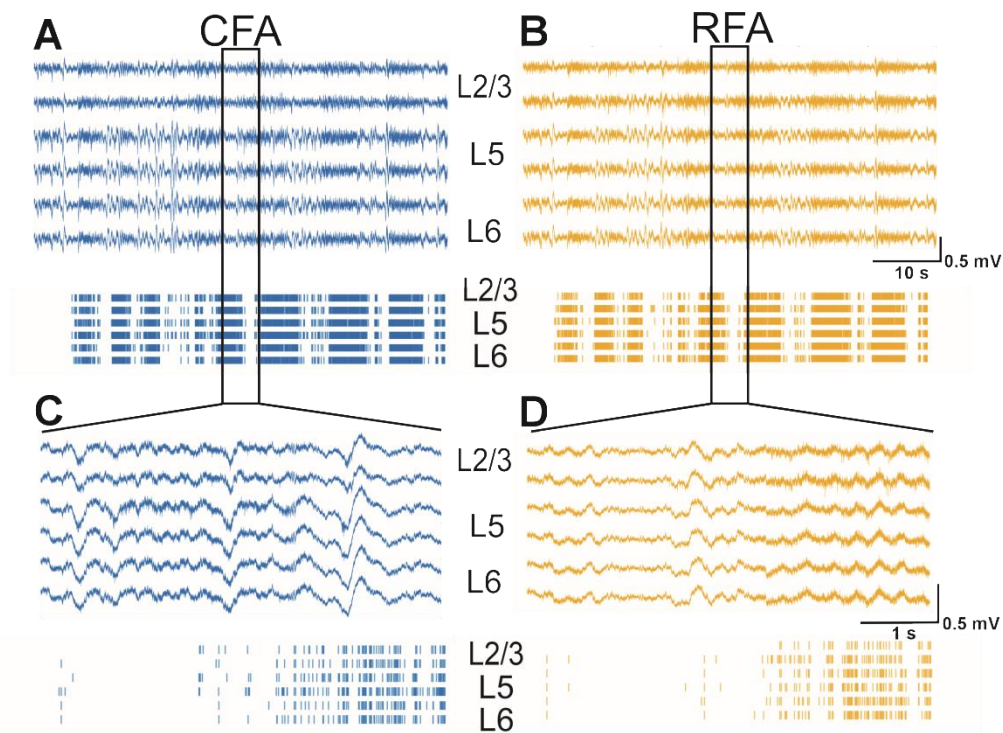


**Figure 5: Spontaneous activity recorded simultaneously in all layers of RFA and CFA.** (A-D) Simultaneous recordings of spontaneous activity from layers L2/3 (first and second trace), L5 (third, fourth trace) and L6 (fifth, sixth trace) of CFA (A, blue) and RFA (B, yellow). Representative 60 s segments of local field potentials (LFP, A and B) and multi-unit activity (MUA, bottom panel) were recorded simultaneously in RFA and CFA (top). Lower traces show a 5 s segment at higher temporal resolution C, D) (adapted from Kreis et al. 2022).

Both the LFP and MUA recorded from the RFA and CFA exhibit distinct patterns of activity characterized by alternating periods of higher and lower activity. Notably, the LFP signal demonstrates pronounced similarities across different layers within each region. This observed consistency in LFP patterns is also evident in the MUA recorded from both the RFA and CFA.

In order to further analyse the LFP signals, a spectral power analysis was performed on data recorded from layers 2/3, 5, and 6 in both the RFA and CFA. The resulting power spectrum was segmented into frequency bands.

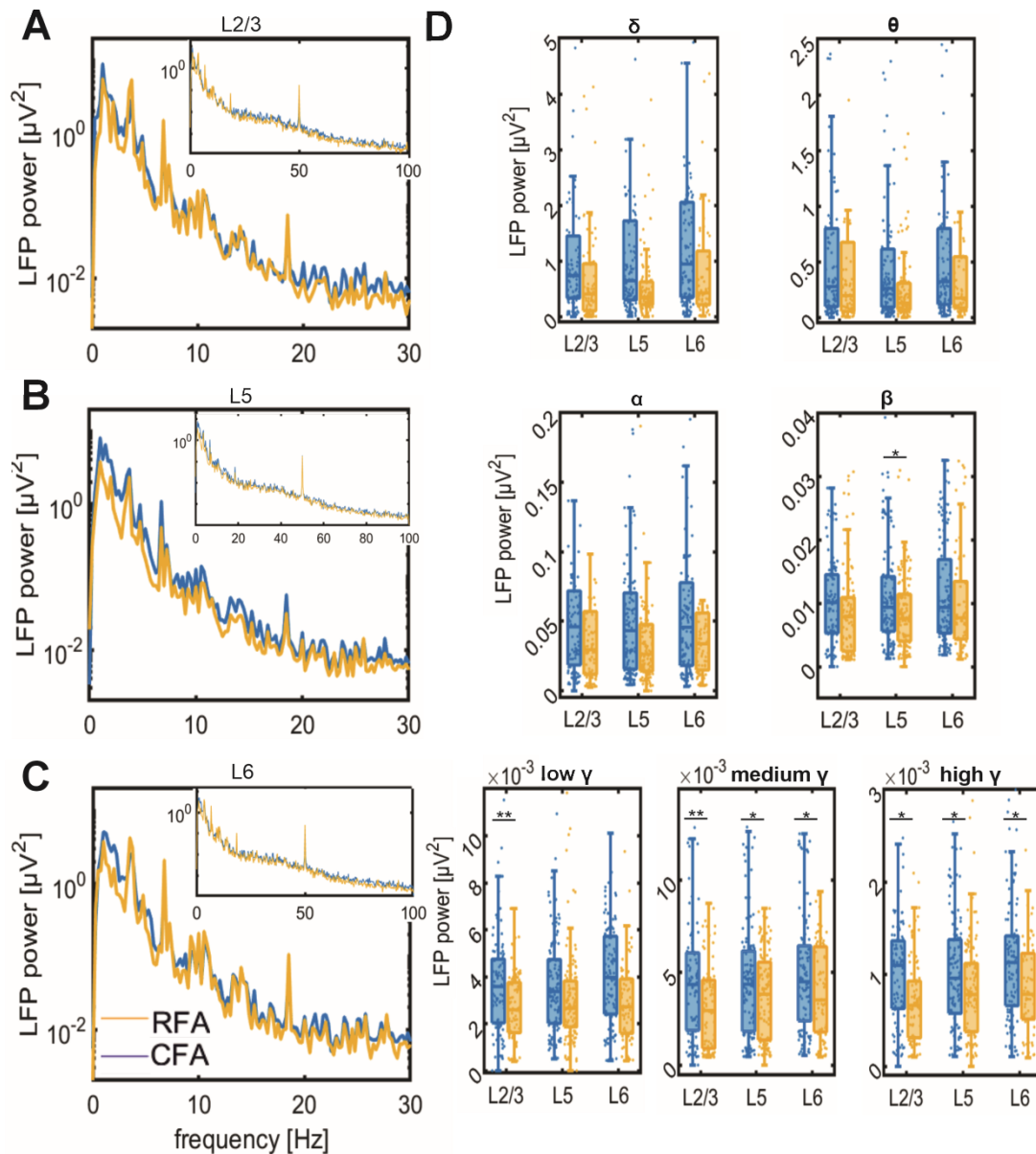


**Figure 6: Spectral power in mice RFA and CFA.**

Spectral power of spontaneous LFP activity recorded in CFA (blue) and RFA (yellow). The LFP power spectrum for L2/3 (A), L5 (B) and L6 (C) for 0-30 Hz of CFA (blue) and RFA (yellow). Inset figures show the corresponding spectrum for 0-100 Hz. (D) Boxplots of the spectral power separated into seven frequency bands averaged across 16 mice. Each analyzed channel is represented by a dot; the scale is different in every boxplot to visualize the differences between RFA and CFA. \* represents  $p < 0.05$ , \*\*  $p < 0.001$ . (Kreis et al. 2022)

The highest LFP power was observed at low frequencies in both motor cortex areas (Figure 6). All layers of RFA and CFA exhibited the highest LFP power in the  $\delta$ -frequency band, the lowest LFP power was detected in the high  $\gamma$ -frequency band. The LFP power in the  $\beta$ - and

low to high  $\gamma$ -bands was significantly higher in the CFA as compared to the RFA (Figure 6, Table 1).

**Table 1: Spectral power of spontaneous LFP activity recorded in CFA and RFA.**

frequency band	layer	LFP power CFA (mean $\pm$ SD)	LFP power RFA (mean $\pm$ SD)	p-value
$\delta$	L2/3	2.4867 $\pm$ 5.4194	1.5323 $\pm$ 5.4835	
	L5	2.8941 $\pm$ 8.3070	1.2634 $\pm$ 3.6845	
	L6	2.2777 $\pm$ 4.8551	1.2119 $\pm$ 2.5145	
$\theta$	L2/3	0.6979 $\pm$ 1.0824	0.9055 $\pm$ 1.6830	
	L5	0.7867 $\pm$ 1.3837	0.4580 $\pm$ 0.9375	
	L6	0.7408 $\pm$ 1.0973	0.8484 $\pm$ 1.4794	
$\alpha$	L2/3	0.0704 $\pm$ 0.0906	0.0697 $\pm$ 0.1027	
	L5	0.0701 $\pm$ 0.0905	0.0498 $\pm$ 0.0772	
	L6	0.0726 $\pm$ 0.0866	0.0741 $\pm$ 0.1086	
$\beta$	L2/3	0.0105 $\pm$ 0.0067	0.0086 $\pm$ 0.0072	
	L5	0.0112 $\pm$ 0.0083	0.0085 $\pm$ 0.0059	0.0024
	L6	0.0116 $\pm$ 0.0082	0.0101 $\pm$ 0.0082	
low $\gamma$	L2/3	0.0045 $\pm$ 0.0032	0.0032 $\pm$ 0.0023	9.7975e <sup>-04</sup>
	L5	0.0045 $\pm$ 0.0030	0.0037 $\pm$ 0.0024	
	L6	0.0049 $\pm$ 0.0032	0.0040 $\pm$ 0.0026	
medium $\gamma$	L2/3	0.0010 $\pm$ 0.0006	0.7311e <sup>-03</sup> $\pm$ 0.5304e <sup>-03</sup>	6.3662e <sup>-04</sup>
	L5	0.0010 $\pm$ 0.0006	0.8348e <sup>-03</sup> $\pm$ 0.5221e <sup>-03</sup>	0.0090
	L6	0.0011 $\pm$ 0.0006	0.8895e <sup>-03</sup> $\pm$ 0.5833e <sup>-03</sup>	0.0080
high $\gamma$	L2/3	3.6413e-04 $\pm$ 2.0489e <sup>-04</sup>	0.2825e-03 $\pm$ 0.1971e <sup>-03</sup>	0.0051
	L5	3.6109e-04 $\pm$ 2.0389e <sup>-04</sup>	0.3014e-03 $\pm$ 0.1967e <sup>-03</sup>	0.0171
	L6	4.1706e-04 $\pm$ 2.4914e <sup>-04</sup>	0.3028 e-03 $\pm$ 0.2008e <sup>-03</sup>	0.0013

Mean + standard deviation (n=16 mice) is shown separately for each layer and frequency band; p-values resulted from two-sample t-tests. P-values < 0.017 were considered significant and are highlighted in grey (Kreis et al. 2022).

For the subsequent analysis of spontaneous activity, spike detection followed by threshold-based clustering was employed, resulting in the isolation of 436 single units (SUs) from 16 animals. The mean firing rate of SUs did not exhibit significant differences among different layers in both the RFA and CFA (Table 2). However, the number of SUs was higher in the CFA (n=302) compared to the RFA (n=134). Notably, a substantially greater number of SUs were detected in L6 of the CFA (n=154) compared to L2/3 of both the RFA and CFA. Taken together, these results indicate that RFA and CFA are topologically distinct areas.

**Table 2: Number and mean firing rates of SU in RFA and CFA in different layers** (Kreis et al. 2022).

	RFA		CFA	
	number of SU	SU firing rate (mean ± SD)	number of SU	SU firing rate (mean ± SD)
L2/3	26	3.11 ± 4.10	48	1.97 ± 3.00
L5	54	3.83 ± 6.20	100	2.85 ± 4.29
L6	54	3.07 ± 4.10	154	3.23 ± 5.65
all layers	134	3.11 ± 4.67	302	2.98 ± 4.84

#### 4.1.2 Functional connectivity between RFA and CFA

Next, I addressed the question of whether and how the two motor cortical areas, RFA and CFA, are functionally interconnected in a frequency- and layer-specific manner (Aim 1.2). To this end, LFP coherence was calculated from simultaneous recordings of spontaneous activity recorded in layers 2/3, 5, and 6 from both RFA and CFA. The resulting coherence values were divided into the different frequency bands and averaged across all 16 animals (Figure 7, Table 3). The LFP coherence between RFA and CFA was significant across all layer combinations and frequency bands, as compared to a Monte Carlo random permutation

sequence. The coherence was higher in the  $\beta$ -frequency band as compared to all other frequency bands ( $p < 10^{-12}$ ). The highest coherence was found in the  $\beta$ -frequency band between CFA layer 6 and RFA layer 5 ( $0.7670 \pm 0.1293$ , Table 3) (Kreis et al. 2022).

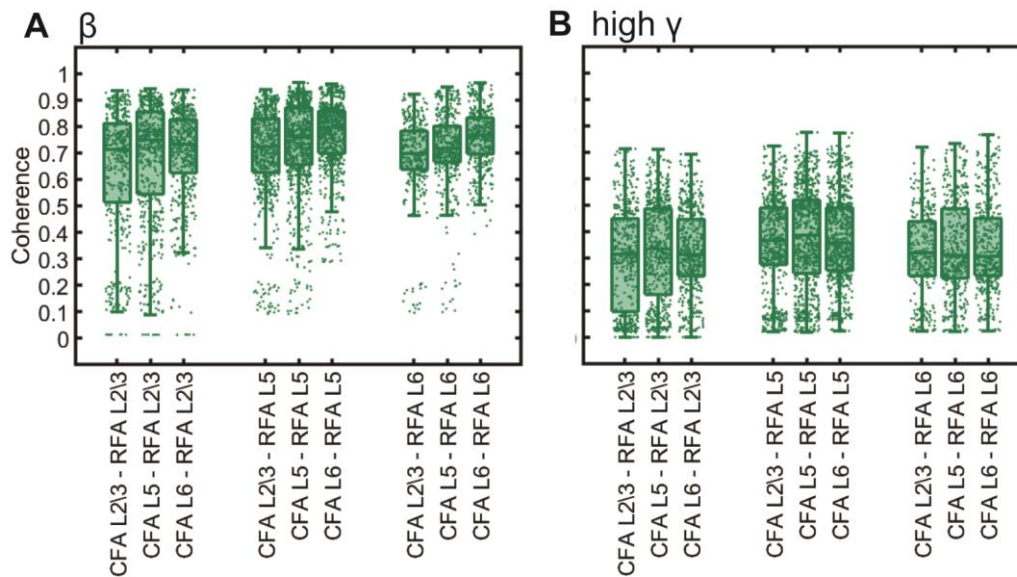


**Figure 7: Coherence in mice CFA and RFA layers.**

Comparison of LFP coherence between layers 2/3, 5, and 6 of RFA and CFA. Boxplots for the beta (A) and high gamma (B) frequency bands averaged across 16 mice, each analyzed channel is represented by a dot (Kreis et al. 2022).

**Table 3: Mean  $\pm$  SD of LFP coherence separated by frequency band and layer averaged across 16 mice** (Kreis et al. 2022)

		CFA L2/3	CFA L5	CFA L6
<b>delta</b>	<b>RFA L2/3</b>	0.3814 $\pm$ 0.2610	0.4667 $\pm$ 0.2281	0.4647 $\pm$ 0.1932
	<b>RFA L5</b>	0.3972 $\pm$ 0.2407	0.5060 $\pm$ 0.2112	0.5641 $\pm$ 0.1819
	<b>RFA L6</b>	0.3749 $\pm$ 0.2269	0.4707 $\pm$ 0.1911	0.5589 $\pm$ 0.1828
<b>theta</b>	<b>RFA L2/3</b>	0.5538 $\pm$ 0.2978	0.6300 $\pm$ 0.2918	0.6472 $\pm$ 0.2423
	<b>RFA L5</b>	0.6027 $\pm$ 0.2416	0.6874 $\pm$ 0.2347	0.7425 $\pm$ 0.1850
	<b>RFA L6</b>	0.5770 $\pm$ 0.2108	0.6482 $\pm$ 0.1870	0.7245 $\pm$ 0.1426
<b>alpha</b>	<b>RFA L2/3</b>	0.5950 $\pm$ 0.2732	0.6524 $\pm$ 0.2762	0.6780 $\pm$ 0.2185
	<b>RFA L5</b>	0.6497 $\pm$ 0.2062	0.7048 $\pm$ 0.2117	0.7473 $\pm$ 0.1616
	<b>RFA L6</b>	0.6134 $\pm$ 0.1865	0.6625 $\pm$ 0.1827	0.7153 $\pm$ 0.1416
<b>beta</b>	<b>RFA L2/3</b>	0.6369 $\pm$ 0.2367	0.6743 $\pm$ 0.2286	0.6969 $\pm$ 0.1726

	<b>RFA L5</b>	0.6960± 0.1792	0.7309±0.1738	0.7670±0.1293
	<b>RFA L6</b>	0.6858± 0.1583	0.7138± 0.1488	0.7586±0.1075
<b>low gamma</b>	<b>RFA L2/3</b>	0.6127±0.2168	0.6430±0.2044	0.6615±0.1823
	<b>RFA L5</b>	0.6604±0.1838	0.6913±0.1793	0.7216±0.1564
	<b>RFA L6</b>	0.6637±0.1765	0.6896±0.1744	0.7250±0.1530
<b>medium gamma</b>	<b>RFA L2/3</b>	0.4202±0.2060	0.4483±0.1961	0.4647±0.1638
	<b>RFA L5</b>	0.4762±0.1730	0.5062±0.1812	0.5207±0.1560
	<b>RFA L6</b>	0.4670±0.1689	0.4967±0.1758	0.5171±0.1591
<b>high gamma</b>	<b>RFA L2/3</b>	0.3037±0.1888	0.3264±0.1876	0.3249±0.1562
	<b>RFA L5</b>	0.3554±0.1767	0.3760±0.1876	0.3717±0.1645
	<b>RFA L6</b>	0.3228±0.1670	0.3400±0.1792	0.3473±0.1647

Linear Mixed-Effects Models (LMM) were employed to investigate significant differences in LFP coherence between all layer combinations of RFA and CFA. Significant differences were identified in the  $\beta$ -frequency band, specifically in the coherence between RFA L5 and L6 with all CFA layers (RFA L5:  $p=3.85e^{-08}$ ; RFA L6:  $p=9.52e^{-05}$ ) and between CFA L5 and L6 with all RFA layers (CFA L5:  $p= 0.0006$ , CFA L6:  $p=8.06e^{-08}$ ). Consistent patterns were observed across all frequency bands (Table 3). Additionally, the coherence between RFA L5 and L6 with CFA L6 surpassed that of any other layer combination in the  $\delta$ - and  $\theta$ -frequency band. Collectively, these findings suggest a layer-specific functional coupling between both cortical regions across all frequency bands.

**Table 4: P-values resulting from LMM analysis of LFP coherence separated by layer and frequency band**

	$\delta$	$\theta$	$\alpha$	$\beta$	low $\gamma$	medium $\gamma$	high $\gamma$
<b>RFA L5</b>	-	$6.017e^{-04}$	$2.447e^{-05}$	$3.851e^{-08}$	$1.715e^{-05}$	$2.155e^{-07}$	$1.627e^{-06}$
<b>RFA L6</b>	-	-	-	$9.519e^{-05}$	$8.082e^{-05}$	$1.992e^{-04}$	-
<b>CFA L5</b>	$1.285e^{-10}$	$1.265e^{-07}$	$1.201e^{-05}$	$5.752e^{-04}$	$6.816e^{-03}$	0.010	0,037
<b>CFA L6</b>	$1.018e^{-09}$	$3.172e^{-10}$	$8.022e^{-10}$	$8.061e^{-08}$	$2.419e^{-05}$	$7.418e^{-05}$	$5.802e^{-0.2}$
<b>RFA L5 :</b>	-	-	-	-	-	-	-

<b>CFA L5</b>							
<b>RFA L6 : CFA L5</b>	-	-	-	-	-	-	-
<b>RFA L5 : CFA L6</b>	2.995e <sup>-06</sup>	0.017	-	-	-	-	-
<b>RFA L6 : CFA L6</b>	1.170e <sup>-06</sup>	0.016	-	-	-	-	-

- indicates not significant;  $p < 0.05$ . RFA L5 : CFA L5 indicates an interaction of the factors RFA layer and CFA layer on the resulting coherence (Kreis et al. 2022).

### 4.1.3 Effective connectivity between RFA and CFA

In order to further analyse the connectivity between RFA and CFA (Aim 1.2), tPDC analysis was applied to identify directionality in the information transmission. To quantify the direction of connectivity between RFA and CFA based on the recorded LFP, Time-Resolved Partial Directed Coherence (tPDC) analysis was performed. Mean tPDC values were calculated for each layer combination and frequency band for both the direction from RFA towards CFA and vice versa (Figure 8). This analysis revealed that despite the extensive bidirectional connectivity between RFA and CFA, there exists a subtle bias towards information flow from RFA towards CFA across a broad spectrum of frequencies. (Table 5). LMM was applied to identify significant effects of the different layers from RFA and CFA as well as for a possible effect of the direction of interaction between the two areas in the different frequency bands. LMM revealed a statistically significant and consistent higher flow of information from all RFA layers towards CFA L2/3 across all frequency bands (Figure 8). This directionality of connectivity was further corroborated by two-sample t-tests, which demonstrated significant differences between the tPDC values for the RFA-to-CFA and CFA-to-RFA directions (Table 5). Notably, the information flow from RFA L6 to CFA L2/3 was significantly higher in all frequency bands compared to the opposite direction (Table 5). Additionally, the flow from RFA L5 to CFA L2/3 was significantly higher as compared to CFA → RFA in all frequency bands except  $\alpha$ - and  $\beta$ - frequency bands.

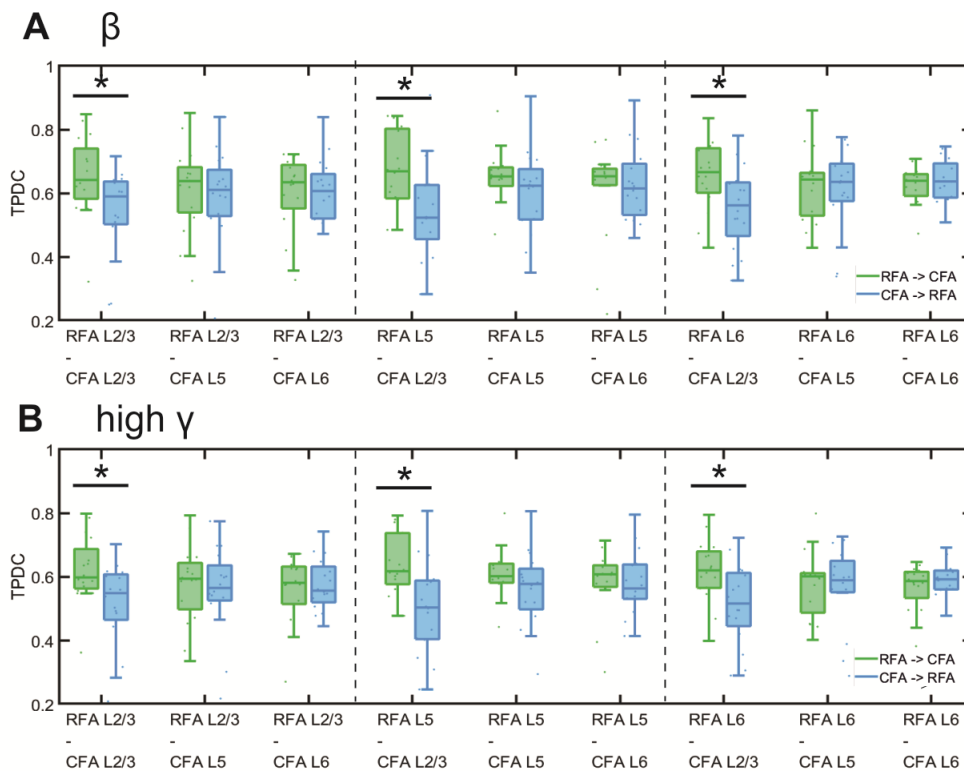


**Figure 8: The TPDC connectivity between mice RFA and CFA.**

Layer-specific directionality of information flow between layers 2/3, 5, and 6 of RFA and CFA in  $\beta$  (A) and high  $\gamma$  (B) bands. Boxplots of TPDC for the directions RFA  $\rightarrow$  CFA (green) and CFA  $\rightarrow$  RFA (blue); averaged across 16 animals. \* indicates significant effects of transmission direction as identified by LMM. (Kreis et al. 2022)

**Table 5: TPDC results, separated by layer combination, direction and frequency band;** mean + standard deviation averaged across n=16 mice: p-values correspond to two-sample t-tests. (Kreis et al. 2022)

frequency	layer combination	RFA $\rightarrow$ CFA	CFA $\rightarrow$ RFA	p
$\delta$	CFA 2/3-RFA 2/3	0.6852 $\pm$ 0.1458	0.5904 $\pm$ 0.1472	
	CFA 5-RFA 2/3	0.6225 $\pm$ 0.1459	0.5904 $\pm$ 0.1472	
	CFA 6-RFA 2/3	0.5960 $\pm$ 0.1264	0.6189 $\pm$ 0.1152	
	CFA 23-RFA 5	0.6756 $\pm$ 0.1718	0.5358 $\pm$ 0.1583	0.0231
	CFA 5-RFA 5	0.6300 $\pm$ 0.1514	0.6049 $\pm$ 0.1425	

	CFA 6-RFA 5	0.6092±0.1540	0.6229±0.1359	
	CFA 23-RFA 6	0.6685±0.1235	0.5456±0.1317	0.0107
	CFA 5-RFA 6	0.6195±0.1310	0.6099±0.1473	
	CFA 6-RFA 6	0.6087±0.1012	0.6321±0.0870	
θ	CFA 2/3-RFA 2/3	0.6616±0.1291	0.5405±0.1497	0.0203
	CFA 5-RFA 2/3	0.6328±0.1341	0.5931±0.1560	
	CFA 6-RFA 2/3	0.6148±0.1084	0.6147±0.1060	
	CFA 2/3-RFA 5	0.6700±0.1595	0.5465±0.1534	0.0332
	CFA 5-RFA 5	0.6494±0.1380	0.5970±0.1364	
	CFA 6-RFA 5	0.6241±0.1491	0.6246±0.12/35	
	CFA2/3-RFA 6	0.6717±0.1046	0.5564±0.1293	0.0095
	CFA 5-RFA 6	0.6436±0.1150	0.6027±0.1343	
	CFA 6-RFA 6	0.6247±0.0889	0.6340±0.0772	
α	CFA2/3-RFA 2/3	0.6437±0.1296	0.5273±0.1426	0.0220
	CFA 5-RFA 2/3	0.6092±0.1327	0.5763±0.1501	
	CFA 6-RFA 2/3	0.5907±0.1141	0.5957±0.1011	
	CFA2/3-RFA 5	0.6494±0.1627	0.5384±0.1565	
	CFA 5-RFA 5	0.6267±0.1403	0.5904±0.1421	
	CFA 6-RFA 5	0.6056±0.1489	0.6135±0.1248	
	CFA2/3-RFA 6	0.6487±0.1070	0.5464±0.1271	0.0198
	CFA 5-RFA 6	0.6185±0.1137	0.5984±0.1342	
	CFA 6-RFA 6	0.6046±0.0867	0.6279±0.0736	
β	CFA2/3-RFA 2/3	0.6528±0.1291	0.5401±0.1368	0.0230
	CFA 5-RFA 2/3	0.6167±0.1354	0.5897±0.1507	
	CFA 6-RFA 2/3	0.5959±0.1251	0.5959±0.1251	
	CFA2/3-RFA 5	0.6554±0.1645	0.5485±0.1530	
	CFA 5-RFA 5	0.6305±0.1408	0.6037±0.1340	
	CFA 6-RFA 5	0.6092±0.1514	0.6037±0.1340	
	CFA2/3-RFA 6	0.6568±0.1103	0.5547±0.1298	0.0229
	CFA 5-RFA 6	0.6254±0.1125	0.6091±0.1343	

	CFA 6-RFA 6	0.6134±0.0869	0.6403±0.0667	
low $\gamma$	CFA2/3-RFA 2/3	0.6613±0.1251	0.5379±0.1354	
	CFA 5-RFA 2/3	0.6222±0.1333	0.5891±0.1499	
	CFA 6-RFA 2/3	0.6003±0.1312	0.6104±0.0939	
	CFA2/3-RFA 5	0.6595±0.1602	0.5450±0.1518	0.0465
	CFA 5-RFA 5	0.6315±0.1373	0.6045±0.1323	
	CFA 6-RFA 5	0.6069±0.1539	0.6304±0.1091	
	CFA2/3-RFA 6	0.6641±0.1088	0.5503±0.1396	0.0153
	CFA 5-RFA 6	0.6298±0.1087	0.6090±0.1423	
	CFA 6-RFA 6	0.6145±0.0846	0.6407±0.0631	
medium $\gamma$	CFA2/3-RFA 2/3	0.6462±0.1227	0.5375±0.1458	
	CFA 5-RFA 2/3	0.6026±0.1329	0.5883±0.1450	
	CFA 6-RFA 2/3	0.5839±0.1246	0.6085±0.0889	
	CFA2/3-RFA 5	0.6513±0.1536	0.5352±0.1523	0.0399
	CFA 5-RFA 5	0.6192±0.1368	0.5958±0.1266	
	CFA 6-RFA 5	0.5952±0.1484	0.6192±0.1025	
	CFA2/3-RFA 6	0.6540±0.1010	0.5431±0.1401	0.0154
	CFA 5-RFA 6	0.6139±0.1080	0.6010±0.1382	
	CFA 6-RFA 6	0.5994±0.0785	0.6325±0.0584	
high $\gamma$	CFA2/3-RFA 2/3	0.6206±0.1072	0.5104±0.1368	0.0166
	CFA 5-RFA 2/3	0.5776±0.1234	0.5563±0.1404	
	CFA 6-RFA 2/3	0.5633±0.1078	0.5758±0.0818	
	CFA2/3-RFA 5	0.6188±0.1509	0.5050±0.1469	0.0388
	CFA 5-RFA 5	0.5867±0.1342	0.5615±0.1208	
	CFA 6-RFA 5	0.5633±0.1417	0.5815±0.0985	
	CFA2/3-RFA 6	0.6182±0.0996	0.5149±0.1267	0.0157
	CFA 5-RFA 6	0.5800±0.1056	0.5673±0.1285	
	CFA 6-RFA 6	0.5669±0.0746	0.5938±0.0573	

#### 4.1.4 Structural equation modelling

In addressing the question of whether the SU activity can be inferred based on spectral measures of LFPs, which were recorded from the mouse RFA and CFA, Prof.Dr.-Ing Muthuraman Muthuraman conducted structural equation modelling. This robust statistical technique was employed to assess the hypothesized causal relationships between RFA-CFA connectivity and subsequent activity measures within the network. By simultaneously evaluating direct and indirect effects among the modelled variables, SEM provided a more comprehensive understanding of the underlying neural dynamics.

The first model examined the causal relations of TPDC from RFA L5 to CFA L2/3 (considered as the input variable) on both LFP coherence and power in the  $\beta$ -frequency band within the RFA-CFA network, acting as potential mediating variables. Additionally, the model incorporated the single unit activity (SU) of both regions. Fit indices indicated a good model fit (RFA L5:  $s = 0.75$ ,  $p < 0.01$ ; CFA L2/3:  $s = 0.69$ ,  $p < 0.01$ ), suggesting the model adequately captured the observed data and provided robust estimates of causal relationships. Specifically, RFA-to-CFA TPDC positively impacted the SU of both RFA L5 and CFA L2/3, with the former mediated by RFA-L5 to L2/3 coherence. This finding suggests that stronger information flow from RFA to CFA (tPDC), leads to increased neural synchronization (coherence) within RFA and higher SU activity in both regions. Furthermore, the second model revealed similar causal relationships in the high  $\gamma$ -frequency band (Figure 9). TPDC significantly predicted the SU activity of both RFA L5 and CFA L2/3, demonstrating consistent frequency-independent modulation of network activity by RFA-to-CFA information flow.

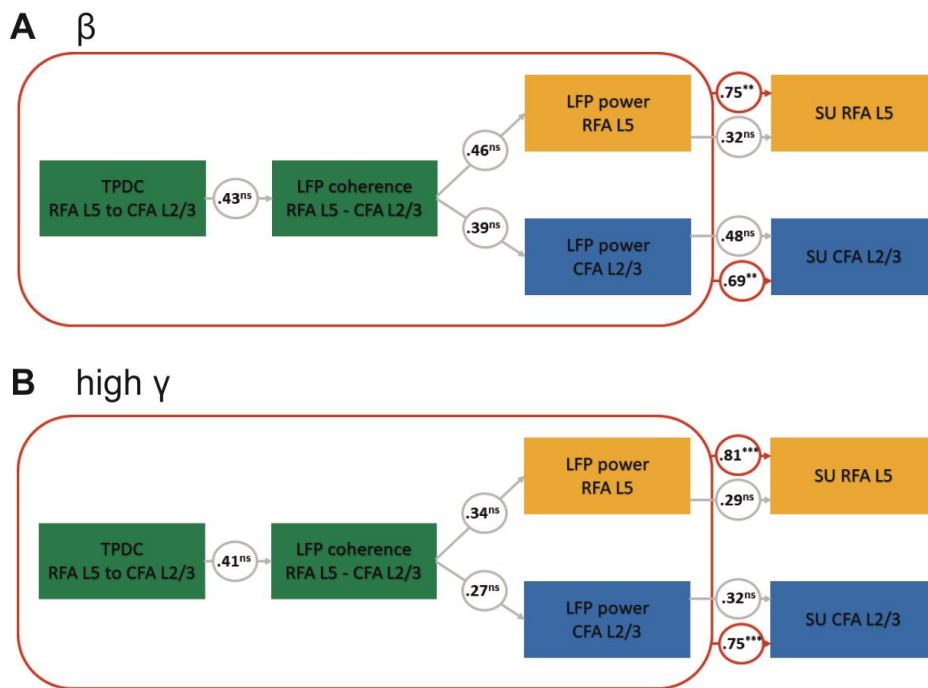


**Figure 9: Structural equation modelling (SEM).**

Results from the SEM analysis for the  $\beta$ -frequency band (A) and the high  $\gamma$ -frequency band (B). Numbers in circles represent standardized coefficients; grey lines and circles indicate the relationship between the individual parameters; red lines and circles indicate significant coefficients in the overall performance of the model; ns stands for not significant, \*\* indicates  $p < 0.001$ , \*\*\* indicates  $p < 0.0001$  (Kreis et al. 2022). This analysis was performed by Prof.Dr.-Ing Muthuraman Muthuraman.

## 4.2 Effect of high frequency stimulation in the RFA-CFA-STN network

The STN plays a critical role in motor control. However, its precise contributions and the mechanisms by which it interacts with other brain regions remain incompletely understood. High frequency stimulation of the STN is a well-established treatment for Parkinson's disease and other movement disorders. However, its effect on the connectivity within the Rostral Frontal Area (RFA), Caudal Frontal Area (CFA), and STN network remains an open question. Given the pivotal role of these regions in motor function, understanding how STN stimulation influences their interplay is of paramount importance.

Therefore, the primary aim of this study (Aim 2) was to elucidate the impact of high frequency STN stimulation on the RFA-CFA-STN network. By addressing this question, I

aimed to gain a deeper understanding of how HFS of the STN modulates the dynamics and communication patterns within the RFA-CFA-STN network, potentially contributing to a more comprehensive understanding of its therapeutic effects in movement disorders.

The resulting data were analyzed and illustrated as local field potential (LFP; 0.1-250 Hz). A 60 s segment of LFP raw signal of spontaneous activity recorded simultaneously in RFA, CFA and STN is shown in Figure 10 A and below a 7 s segment in higher magnification (Figure 10 C). The LFP signal recorded in RFA and CFA is very similar between the two areas and across all layers. As described in section 4.1.1 ( Spontaneous activity in the mouse motor cortex), the activity in RFA and CFA consists of alternating periods of higher and lower activity that each last for several seconds. Typical STN recordings on the other hand consist of longer periods with relatively low activity interrupted by short burst-like periods of higher activity (see Figure 10 A, C).

The high frequency STN stimulation leads to a strong stimulation artefact in all areas (Figure 10 B, D). To avoid falsifying the analysis, I did not analyse any data recorded within a 1s segment after stimulus onset. As shown in Figure 10 D, this time window is sufficient for the stimulation artefact to subside.

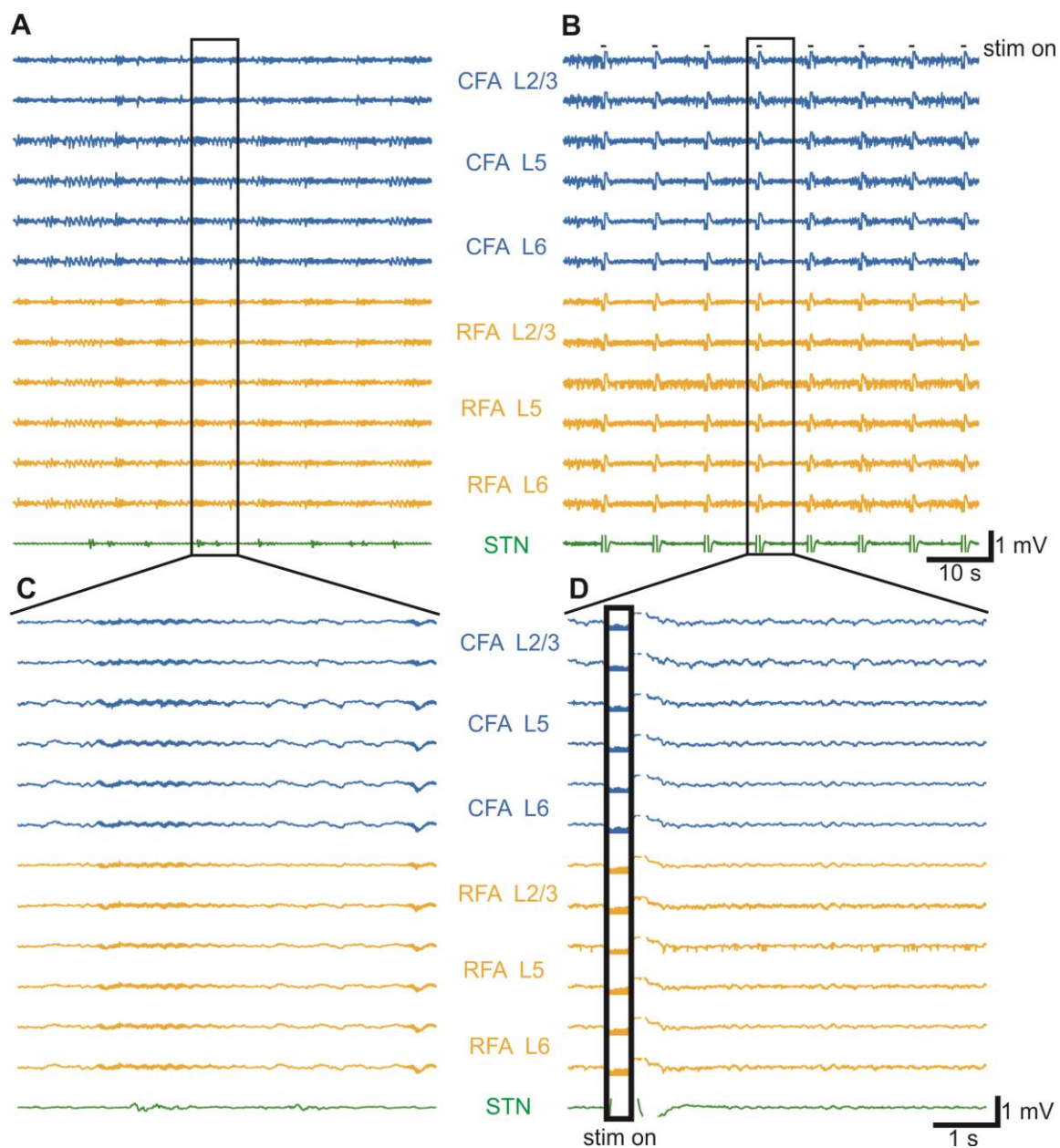


**Figure 10: Neuronal activity recorded in CFA, RFA and STN with and without 160 Hz STN stimulation.** (A) 60s segment of simultaneous recordings of spontaneous activity from CFA (blue), RFA (yellow) and STN (green). (B) Representative 60s segments of local field potentials were recorded in the same channels during 160 Hz STN stimulation from CFA, RFA and STN. (C) 7s segment of simultaneous recordings of spontaneous activity from CFA (blue), RFA (yellow) and STN (green). (D) Representative 7s segments of local field potentials were recorded during 160 Hz STN stimulation from CFA, RFA and STN.

#### 4.2.1 Neuronal activity in all layers of RFA, CFA and the STN returns to baseline within 10 min after STN stimulation

Before examining the impact of varying stimulation frequencies on activity and connectivity in RFA, CFA, and STN, it is essential to assess any alterations in spontaneous activity during the lengthy recording session. In this regard, I evaluated all analyzed features in all layers of RFA and CFA, as well as the STN at three different time points within the recording sessions: initial recording (labelled 'first'), mid-session recording (labelled 'middle'), and final recording (labelled 'last').

Neither LFP power (see Figure 11) nor coherence (see Figure 14) between RFA, CFA, and STN exhibited significant changes throughout the extended recording session with multiple stimulation frequencies applied in random order. Utilizing linear mixed-effects models demonstrated that there were no noticeable fluctuations in LFP signal power or coherence over time. This suggests that a 10-minute period without stimulation between each analyzed frequency was adequate for the areas of interest to return to their baseline activity before testing subsequent frequencies. Consequently, this approach ensures the sequential evaluation of the effect of different stimulation frequencies on neuronal activity and connectivity without previous stimuli affecting the results.

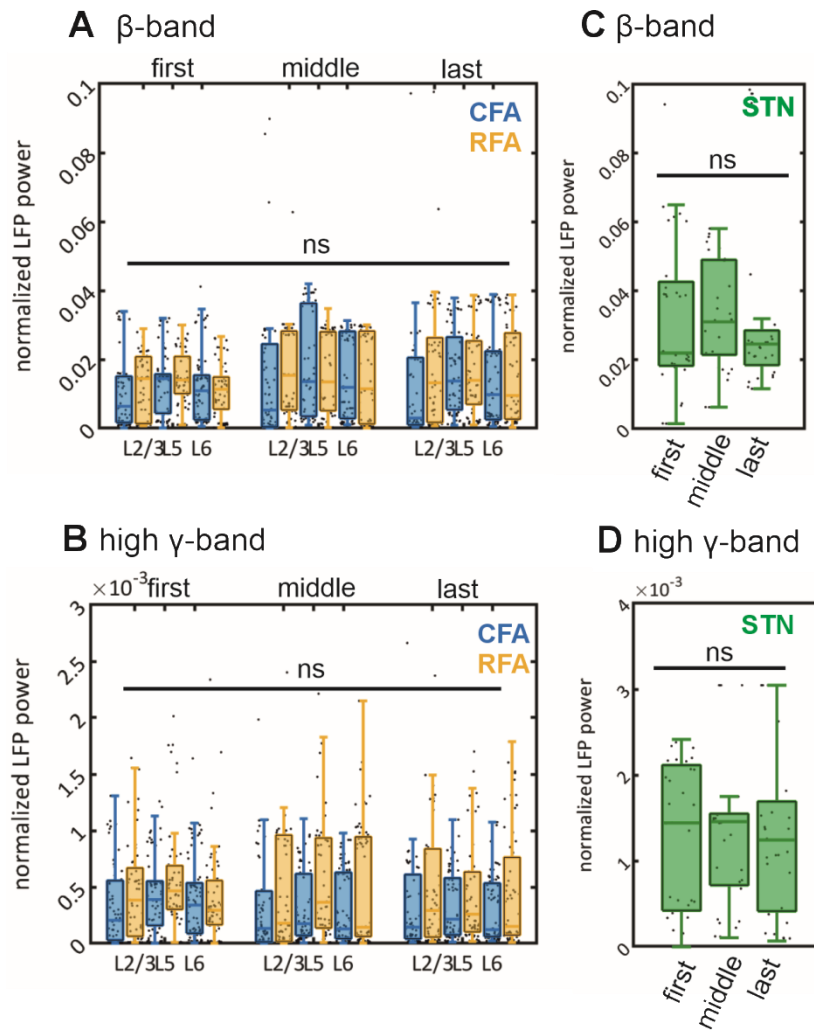


**Figure 11: LFP power in the  $\beta$ - and high  $\gamma$ -frequency band in RFA, CFA and STN returns to baseline after STN stimulation.** LFP power in L2/3, 5, and 6 of CFA (blue) and RFA (yellow) in  $\beta$ - (A) and high  $\gamma$ - (B) frequency band and LFP power in STN in  $\beta$ - (C) and high  $\gamma$ - (D) frequency band at the different time points during the recording session; ‘first’ represents the first recording of spontaneous activity of each session; ‘middle’ represents a recording at the middle of each recording session and ‘last’ represents the last recording of spontaneous activity of each session. All boxplots contain data from nine mice. In each box, the central mark indicates the median, and the bottom and top edges of the box indicate the 25th and 75th percentiles, respectively. The whiskers extend to the most extreme data points not considered outliers. ns represents not significant. (Kreis et al., in preparation)

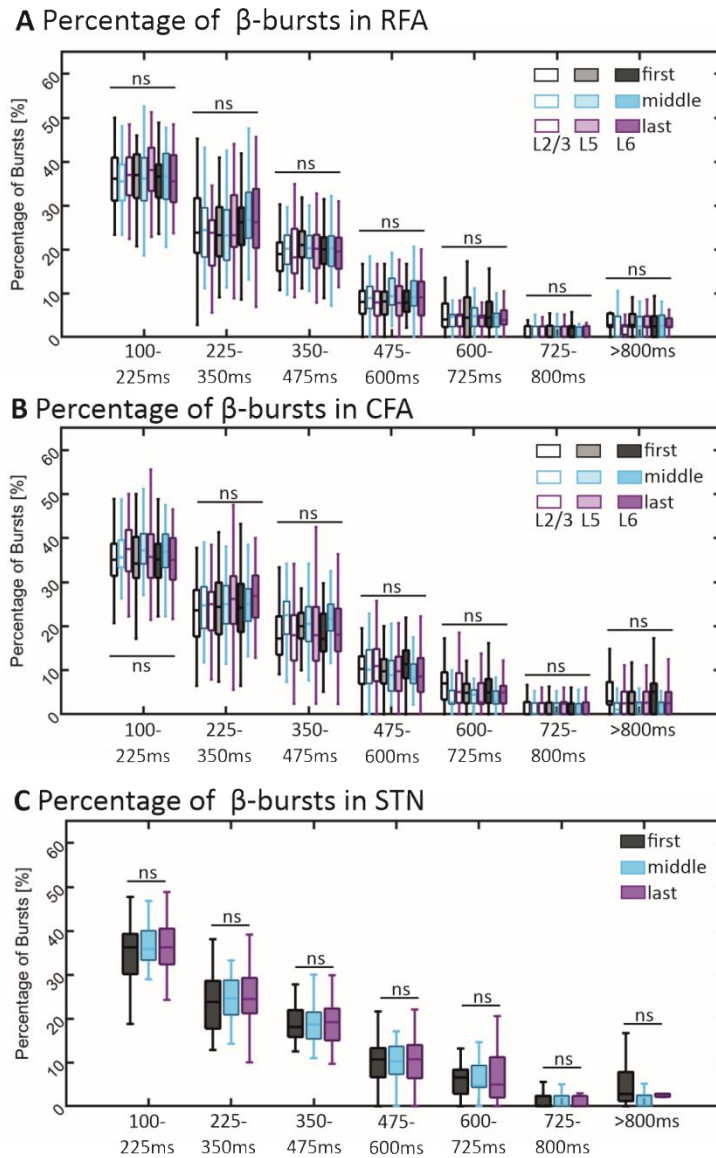


**Figure 12: Distribution of long and short  $\beta$ -bursts in RFA, CFA and STN returns to baseline after STN stimulation.** Percentage of  $\beta$ -bursts of different durations in L2/3, 5, and 6 of RFA (A), CFA (B) and STN (C) at the different time points during the recording session; ‘first’ (black) represents the first recording of spontaneous activity of each session; ‘middle’ (blue) represents a recording at the middle of each recording session and ‘last’ (purple) represents the last recording of spontaneous activity of each session. All boxplots contain data from nine mice. In each box, the central mark indicates the median, and the bottom and top edges of the box indicate the 25th and 75th percentiles, respectively. The whiskers extend to the most extreme data points not considered outliers. ns represents not significant. (Kreis et al., in preparation)

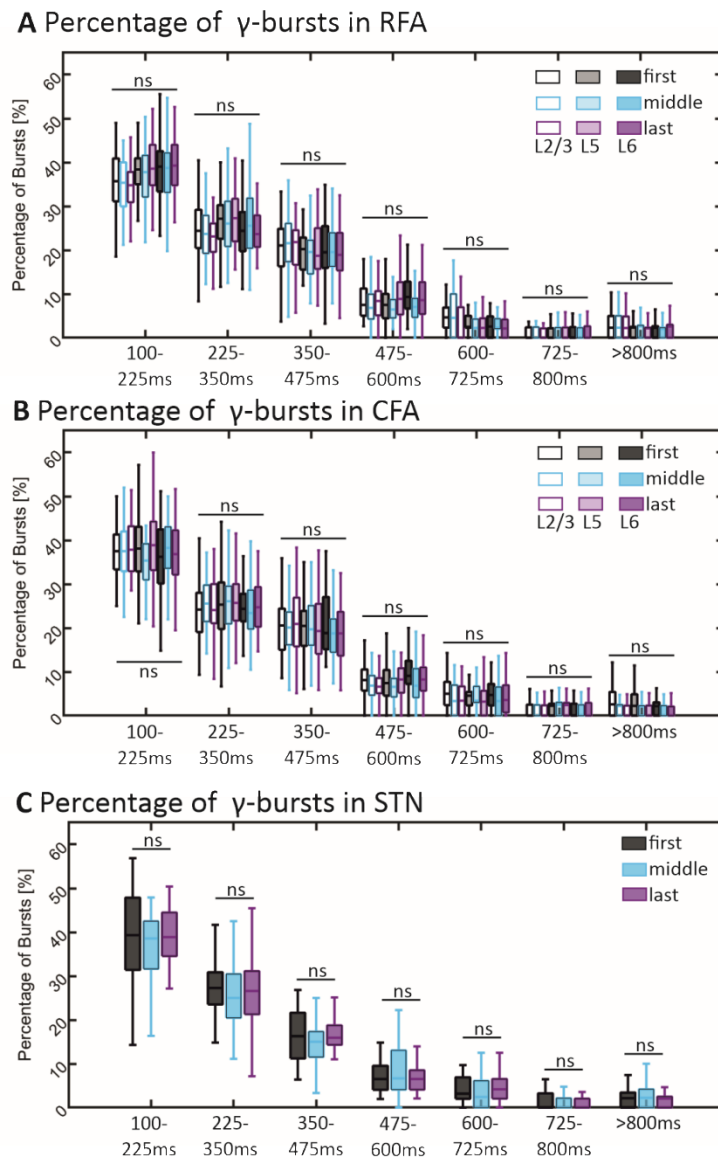


**Figure 13: Distribution of long and short  $\gamma$ -bursts in RFA, CFA and STN returns to baseline after STN stimulation.** Percentage of  $\gamma$ -bursts of different durations in L2/3, 5, and 6 of RFA (A), CFA (B) and STN (C) at the different time points during the recording session; ‘first’ (black) represents the first recording of spontaneous activity of each session; ‘middle’ (blue) represents a recording at the middle of each recording session and ‘last’ (purple) represents the last recording of spontaneous activity of each session. All boxplots contain data from nine mice. In each box, the central mark indicates the median, and the bottom and top edges of the box indicate the 25th and 75th percentiles, respectively. The whiskers extend to the most extreme data points not considered outliers. ns represents not significant. (Kreis et al., in preparation)

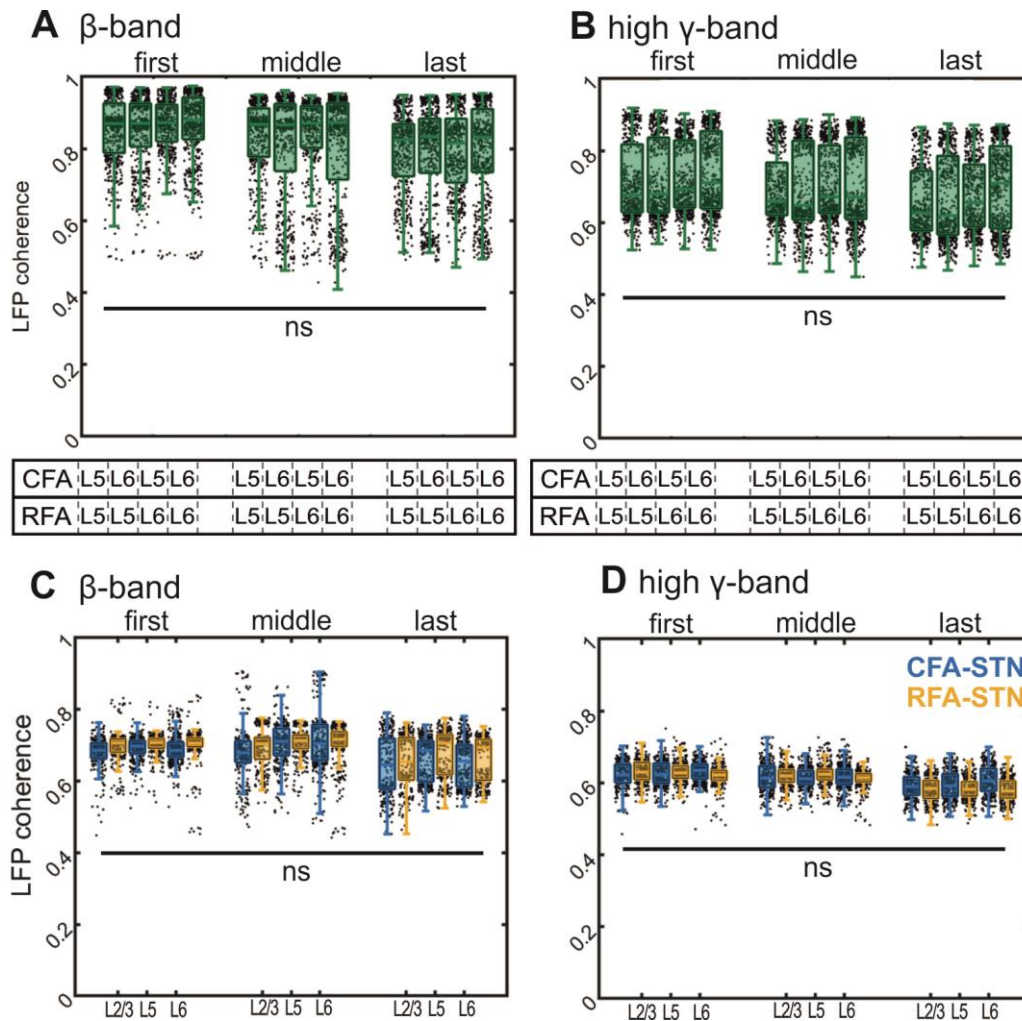


**Figure 14: LFP coherence of spontaneous activity between RFA, CFA and STN in the  $\beta$ - and high  $\gamma$ - frequency band returns to baseline after STN stimulation.** Coherence between spontaneous activity recorded in CFA, RFA and STN at the different time points during the recording session; ‘first’ represents the first recording of spontaneous activity of each session; ‘middle’ represents a recording at the middle of each recording session and ‘last’ represents the last recording of spontaneous activity of each session. (A, B) Comparison of LFP coherence between L2/3, 5, and 6 of RFA and CFA in the  $\beta$ - and high  $\gamma$ - frequency band (C, D) Comparison of LFP coherence between STN and L2/3, 5, and 6 of RFA and CFA  $\beta$ - and high  $\gamma$ - frequency band. All boxplots contain data from 9 mice. In each box, the central mark indicates the median, and the bottom and top edges of the box indicate the 25th and 75th percentiles, respectively. The whiskers extend to the most extreme data points not considered outliers. Each analyzed channel is represented by a dot. n.s. represents not significant. (Kreis et al., in preparation)

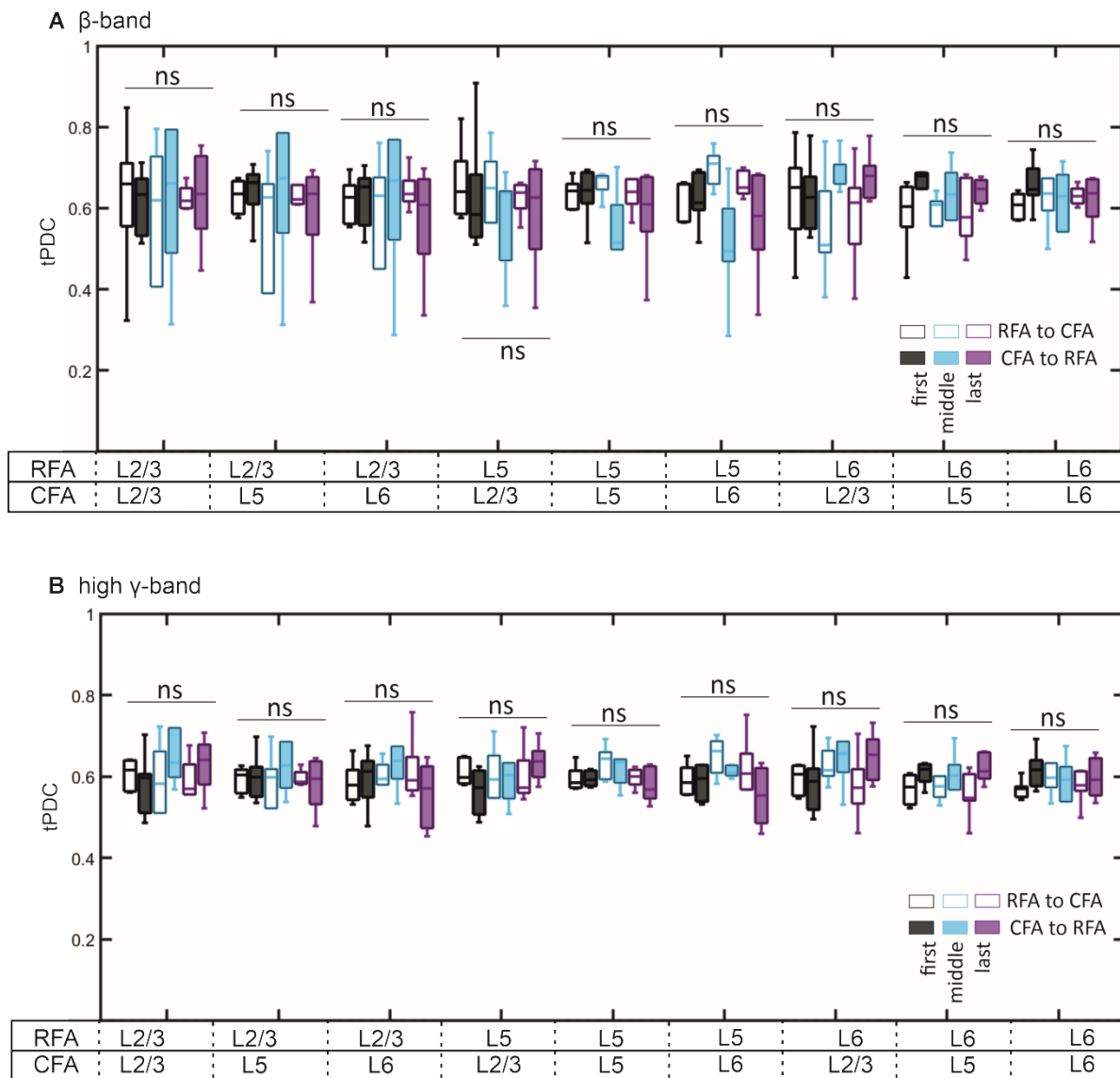


**Figure 15: Information flow between RFA and CFA in the  $\beta$ - and high  $\gamma$ -frequency band returns to baseline after STN stimulation.** The tPDC connectivity between L2/3, 5 and 6 of RFA and CFA. Layer-specific directionality of information flow between L2/3, 5, and 6 of RFA and CFA in  $\beta$ - (A) and high  $\gamma$ -frequency band (B) at the different time points during the recording session; ‘first’ (black) represents the first recording of spontaneous activity of each session; ‘middle’ (blue) represents a recording at the middle of each recording session and ‘last’ (purple) represents the last recording of spontaneous activity of each session. Boxplot of tPDC for the directions RFA→CFA (unshaded) and CFA→RFA (shaded). All boxplots contain data from nine mice. In each box, the central mark indicates the median, and the bottom and top edges of the box indicate the 25th and 75th percentiles, respectively. The whiskers

extend to the most extreme data points not considered outliers. ns represents not significant. (Kreis et al., in preparation)

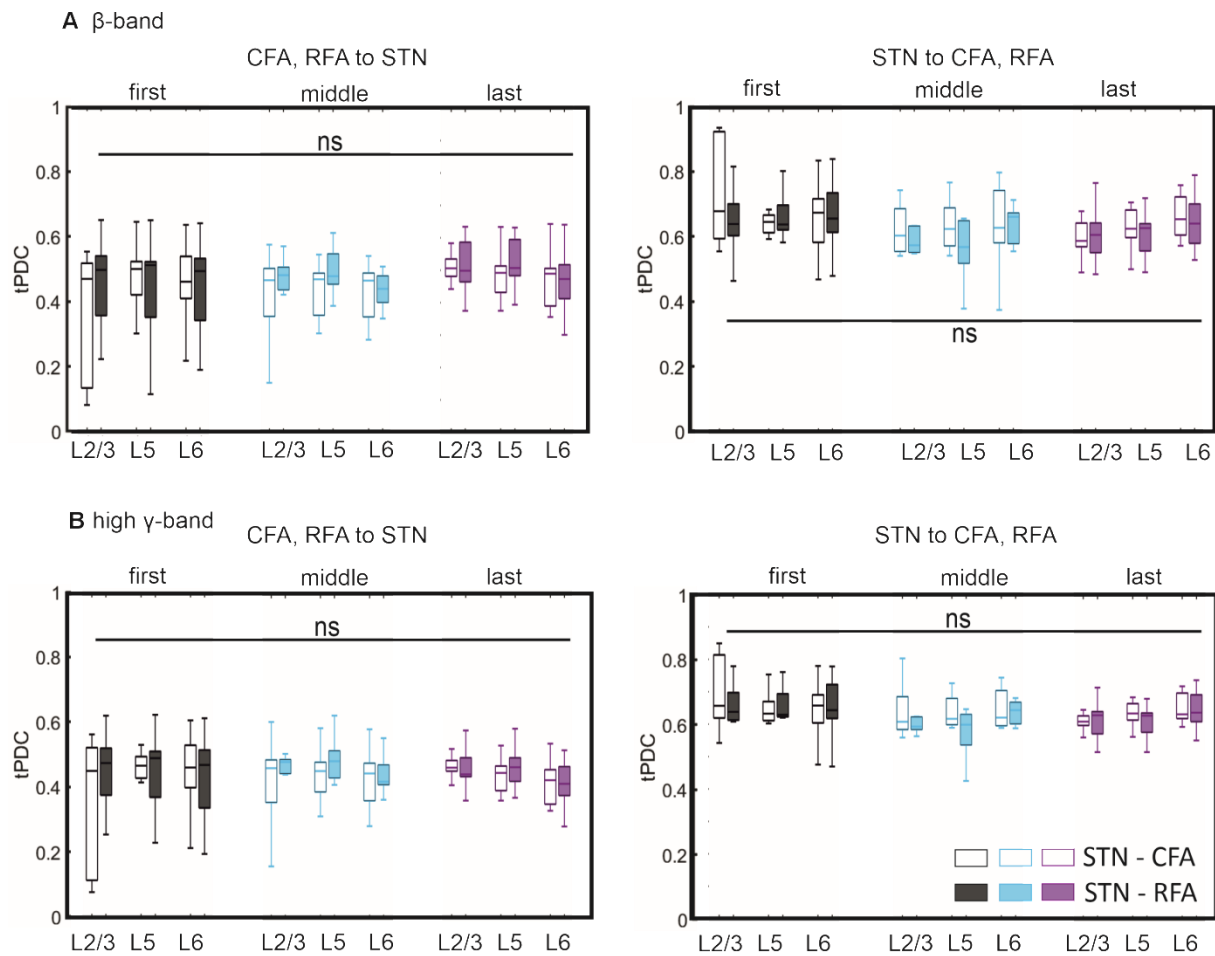


**Figure 16: Information flow between STN, RFA and CFA in the  $\beta$ - and high  $\gamma$ -frequency band returns to baseline after STN stimulation.** tPDC connectivity between STN and L2/3, 5 and 6 of RFA and CFA. Layer-specific directionality of information flow between STN and L2/3, 5, and 6 of RFA and CFA in  $\beta$ - (A) and high  $\gamma$  (B) frequency band, at the different time points during the recording session; ‘first’ (black) represents the first recording of spontaneous activity of each session; ‘middle’ (blue) represents a recording at the middle of each recording session and ‘last’ (purple) represents the last recording of spontaneous activity of each session. Boxplot of tPDC for the connectivity between STN-CFA (unshaded) and STN-RFA (shaded). All boxplots contain data from nine mice. In each box, the central mark indicates the median, and the bottom and top edges of the box indicate the 25th and 75th percentiles, respectively. The whiskers extend to the most extreme data points not considered outliers. ns represents not significant. (Kreis et al., in preparation)

#### 4.2.2 High frequency STN stimulation induces a decrease in spectral LFP power in the $\beta$ -frequency band in RFA, CFA and STN

To investigate the impact of different stimulation frequencies on spectral LFP power in RFA, CFA, and STN, I calculated spectral power, performed linear normalization and averaged over all contacts recorded from each area, across all animals (Figure 17). Next, I utilized linear mixed-effects models to analyze changes in  $\beta$ - and high  $\gamma$ -frequency bands induced by STN stimulation. Our findings revealed that low-frequency (50 Hz) stimulation had no significant effect on  $\beta$  power in RFA and CFA (Figure 9 A). However, high frequency stimulation, particularly at 140 Hz ( $p = 2.67^{-14}$ ), 160 Hz ( $p = 8.86^{-06}$ ), and 180 Hz ( $p = 1.09^{-09}$ ), led to a significant decrease in RFA and CFA  $\beta$ -power (Figure 18).

In contrast, STN stimulation had no significant effect on high  $\gamma$ -frequency power in RFA and CFA (Figure 18). When analyzing the effect of STN stimulation on LFP power recorded in the STN itself, I observed a significant reduction in power across a wide frequency range for all tested stimulation frequencies (Figure 18). Linear mixed-effects models for STN showed a significant reduction in LFP power in the  $\beta$ - and high  $\gamma$ -frequency bands for all tested stimulation frequencies ( $\beta$ : 50 Hz  $t=-8.72$ ,  $p<0.0001$ ; 140 Hz  $t=-12.76$ ,  $p<0.0001$ ; 160 Hz  $t=-9.96$ ,  $p<0.0001$ ; 180 Hz  $t=-11.416$ ; high  $\gamma$ : 50 Hz  $t=-5.86$ ,  $p<0.002$ ; 140 Hz  $t=-6.87$ ,  $p<0.0001$ ; 160 Hz  $t=-4.51$ ,  $p<0.0001$ ; 180 Hz  $t=-6.66$ ).

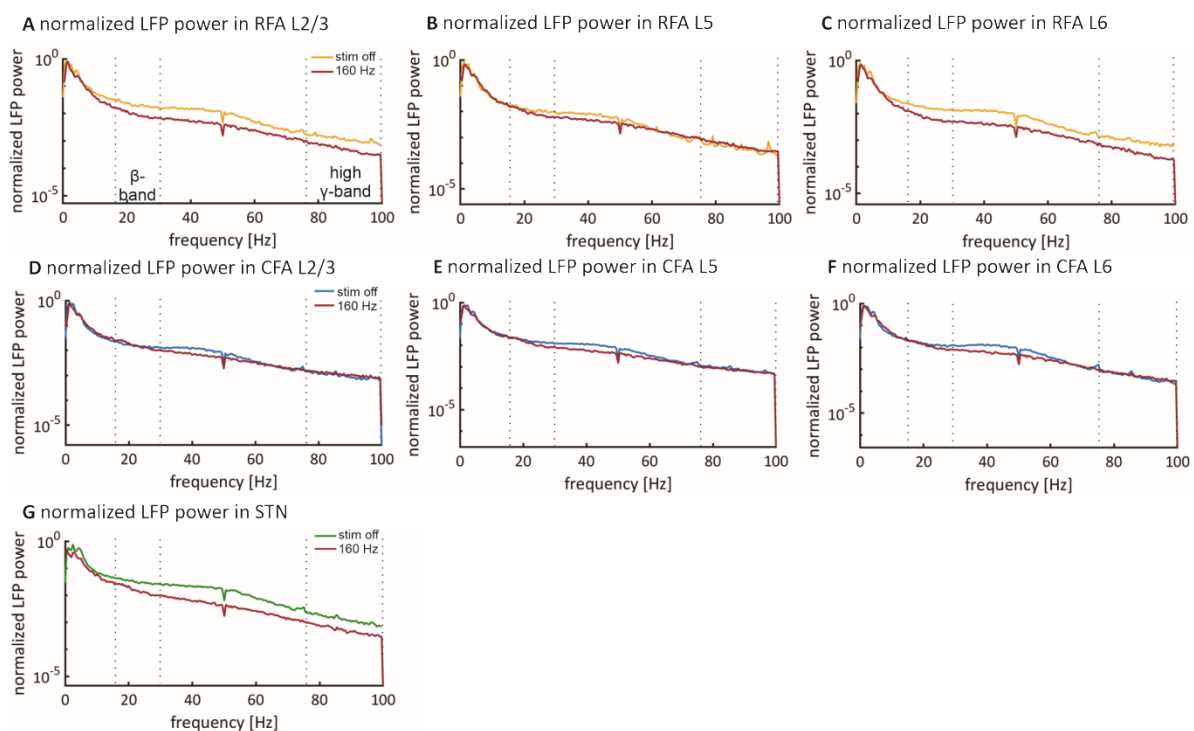


**Figure 17: 160 Hz STN stimulation reduces LFP power in RFA, CFA and STN.** Spectral power of LFPs recorded in different layers of RFA (A-C), CFA (D-F) and STN (G) with and without 160 Hz STN stimulation. The red line in each plot represents the recording with 160 Hz STN stimulation. Lines represent averaged across 9 mice. Dotted lines indicate the borders of the beta and high  $\gamma$ -frequency bands. (Kreis et al., in preparation)

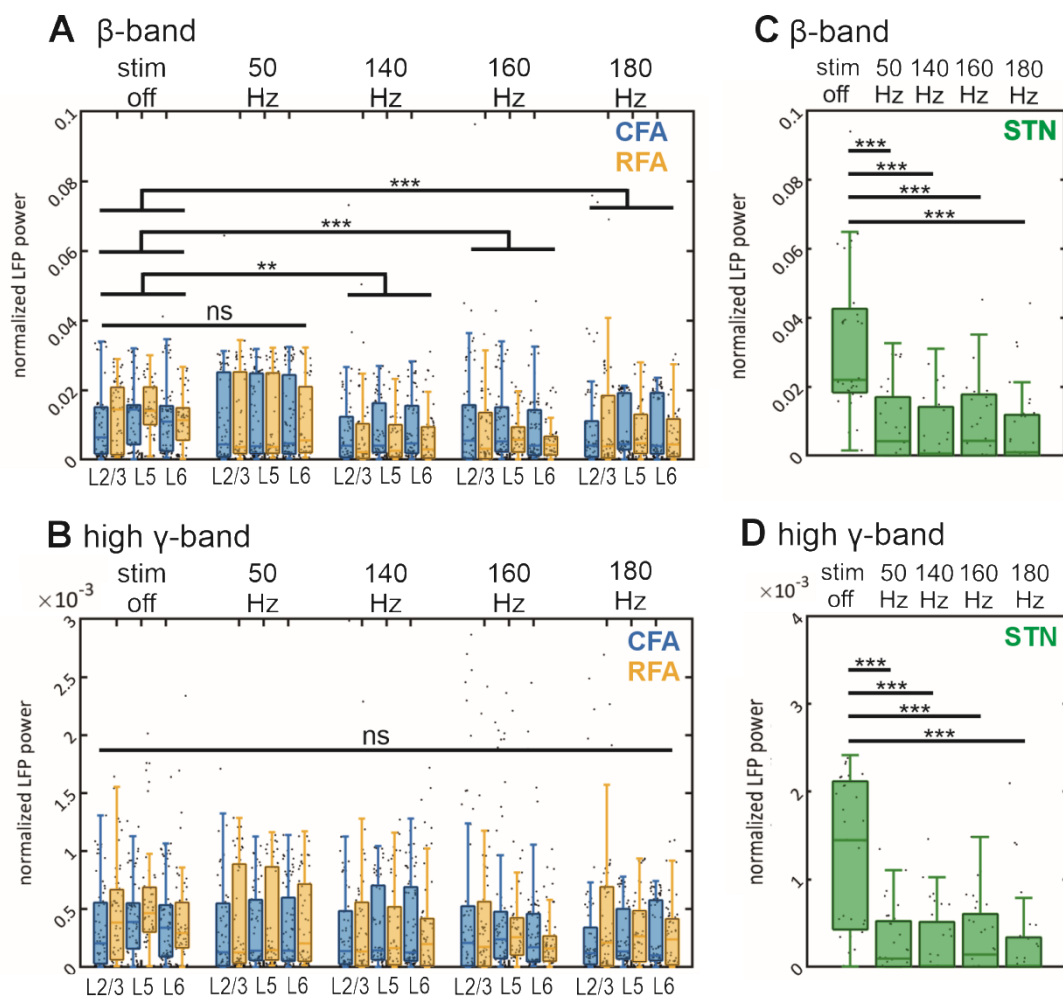


**Figure 18: The influence of high frequency STN stimulation on the LFP power in the  $\beta$ - and high  $\gamma$ -frequency band in RFA, CFA and STN.** LFP power in L2/3, 5, and 6 of CFA (blue) and RFA (yellow) in  $\beta$ - (A) and high  $\gamma$ - (B) frequency band without (stim off) and with STN stimulation at different frequencies. LFP power in STN in  $\beta$ - (C) and high  $\gamma$ - (D) frequency band without and with STN stimulation. All boxplots contain data from 9 mice; All boxplots contain data from 9 mice. In each box, the central mark indicates the median, and the bottom and top edges of the box indicate the 25th and 75th percentiles, respectively. The whiskers extend to the most extreme data points not considered outliers. \* represents  $p < 0.01$ ; \*\*  $p < 0.001$ ; \*\*\*  $p < 0.0001$  (Kreis et al., in preparation)

### 4.2.3 High frequency stimulation modulates cortical and subcortical long $\beta$ -bursts

Next, I examined the impact of high frequency STN stimulation on the duration of  $\beta$ -bursts in RFA, CFA, and the STN itself. The results of this analysis indicated that the average duration of  $\beta$ -bursts during spontaneous activity was significantly higher in RFA as compared to CFA in L5 and L6. In the STN, the average duration of  $\beta$ -bursts during spontaneous activity was 660 ms. However, I did not observe any significant changes in the number or duration of  $\beta$ -bursts (with a duration of more than 100 ms) in any of these regions.

Previous studies have shown that long  $\beta$ -bursts with a duration of more than 475 ms are positively correlated with the worsening of motor symptoms in Parkinson's disease, while short  $\beta$ -bursts are indicative of physiological activity in the motor cortex. Therefore, I analyzed the percentage of bursts with different lengths. My findings revealed that very short bursts (100 to 225 ms) comprised approximately 35-40% of all  $\beta$ -bursts, while longer bursts occurred less frequently (725 to 800 ms: <5%). It is worth noting that the percentage of  $\beta$ -bursts decreased with increasing burst length during spontaneous activity. Furthermore, I examined the effect of STN stimulation on the distribution of  $\beta$ -burst durations. My results showed that there were no significant changes in the number of  $\beta$ -bursts (with a duration of 100-225 ms) in any layer of RFA and CFA during 160 Hz STN stimulation. However, I did observe a significant increase in the percentage of short 100-225 ms bursts in the STN during 160 Hz STN stimulation ( $p < 0.0001$ ). When analyzing the second segment of 225-350 ms burst duration, I found a significant increase in L2/3 and L5 of RFA (L2/3:  $p < 0.001$ ; L5:  $p < 0.001$ ) and L2/3 and L6 of CFA (L2/3:  $p < 0.0001$ ; L6:  $p < 0.001$ ). When analyzing the segments of 350-475 ms, I found a significant increase in the percentage of bursts in L2/3 of RFA ( $p < 0.001$ ) and CFA ( $p < 0.0001$ ) as well as in STN ( $p < 0.001$ ). The appearance of medium-length  $\beta$ -bursts (475-600 ms) was not significantly changed in any of the analyzed areas with 160 Hz STN stimulation.

Further, I found a significant decrease in the percentage of  $\beta$ -bursts with a duration of 600-725 ms in CFA L2/3 ( $p < 0.001$ ), L6 ( $p < 0.001$ ) and STN ( $p < 0.001$ ). When analyzing the percentage of  $\beta$ -bursts in the longest segment (>800 ms), I observed a significant decrease in all layers of RFA and CFA as well as in the STN ( $p < 0.0001$ ).

Taken together, these results indicate an increase in the appearance of short  $\beta$ -bursts (100-475 ms) and a decrease of long  $\beta$ -bursts (>600 ms) in all three brain areas.

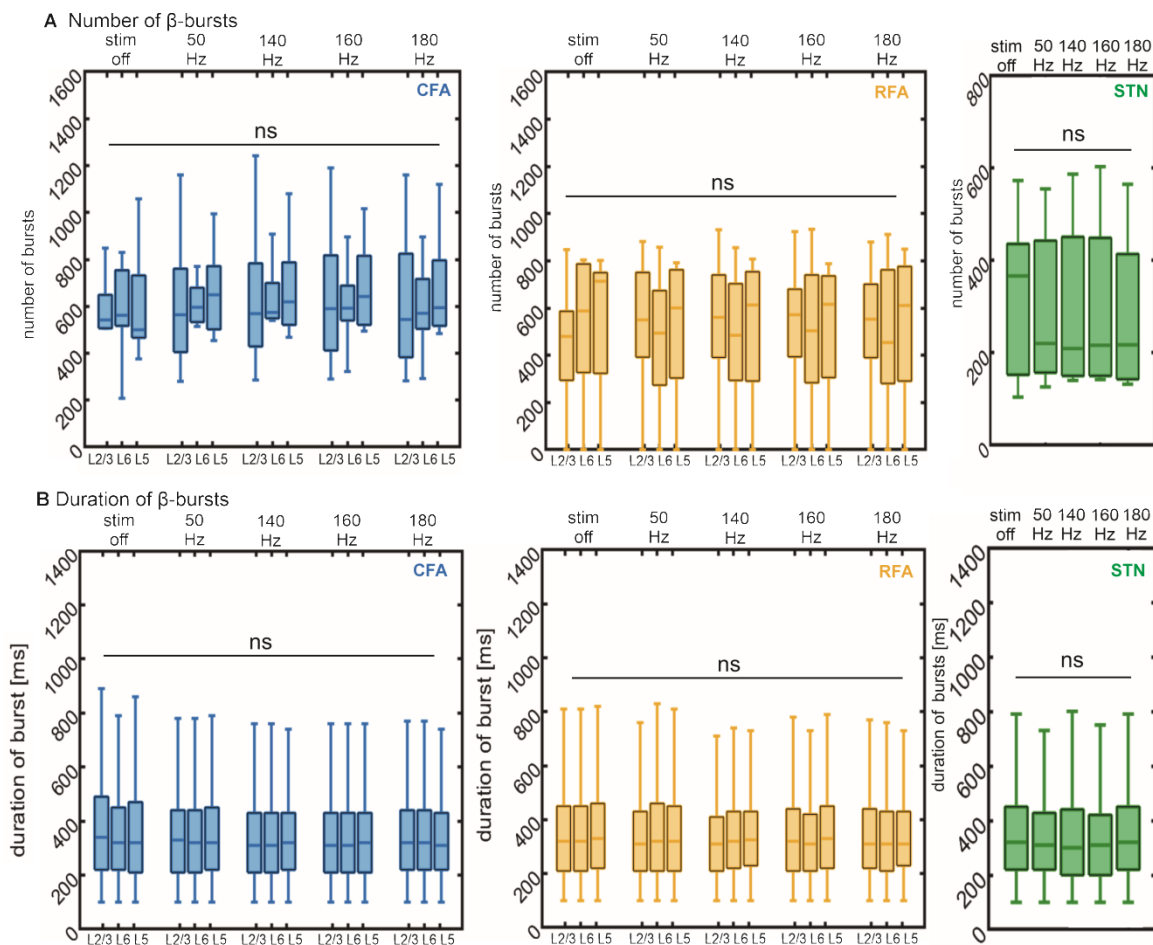


**Figure 19: High frequency STN stimulation does not change the number or duration of  $\beta$ -bursts in RFA, CFA and STN.** Number (A) and duration (B) of  $\beta$ -bursts (duration >100 ms) in L2/3, 5, and 6 of RFA (yellow), CFA (blue) and STN (green) without (stim off) and with STN stimulation. All boxplots contain data from 9 mice. In each box, the central mark indicates the median, and the bottom and top edges of the box indicate the 25th and 75th percentiles, respectively. The whiskers extend to the most extreme data points not considered outliers. (Kreis et al., in preparation)

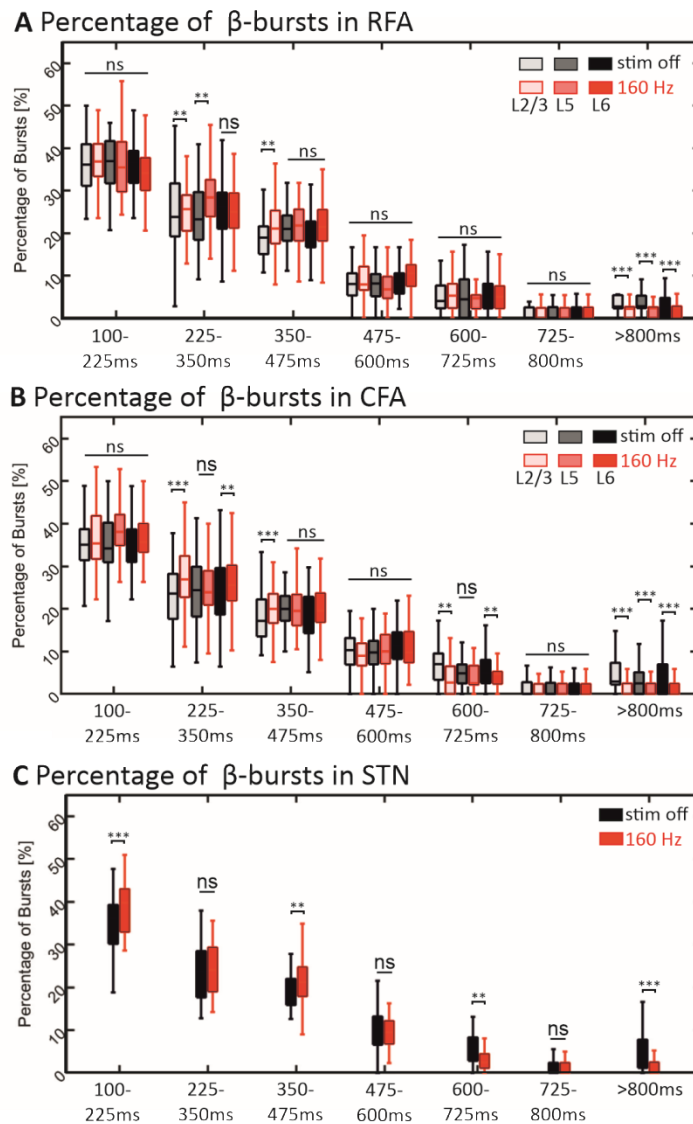


**Figure 20: Reduction of the percentage of long  $\beta$ -bursts in RFA, CFA and STN induced by high frequency STN stimulation.** Percentage of  $\beta$ -bursts of different durations in L2/3, 5, and 6 of RFA (A), CFA (B) and STN (C) without (stim off black) and with 160 Hz STN stimulation (red). All boxplots contain data from nine mice. In each box, the central mark indicates the median, and the bottom and top edges of the box indicate the 25th and 75th percentiles, respectively. The whiskers extend to the most extreme data points not considered outliers. \*\* represents  $p < 0.001$ ; \*\*\*  $p < 0.0001$ , ns represents not significant. (Kreis et al., in preparation)

**Table 6: Reduction of the percentage of long  $\beta$ -bursts in RFA, CFA and STN induced by high frequency STN stimulation.**

Percentage of $\beta$ - Bursts		225-350 ms	100-225 ms	225-350 ms	350-475 ms	475-600ms	600-725 ms	725-800ms
F [Hz]	area	Mean $\pm$ std	Mean $\pm$ std	Mean $\pm$ std	Mean $\pm$ std	Mean $\pm$ std	Mean $\pm$ std	Mean $\pm$ std
Stim off	RFA L2/3	36.26 $\pm$ 7.14	24.66 $\pm$ 8.66	18.81 $\pm$ 4.81	8.30 $\pm$ 3.58	4.89 $\pm$ 3.85	1.37 $\pm$ 1.59	5.70 $\pm$ 6.73
	RFA L5	36.25 $\pm$ 6.37	23.78 $\pm$ 8.18	20.87 $\pm$ 5.28	8.12 $\pm$ 4.26	5.31 $\pm$ 4.89	1.21 $\pm$ 1.96	4.46 $\pm$ 4.10
	RFA L6	36.05 $\pm$ 5.55	25.30 $\pm$ 7.16	19.61 $\pm$ 5.26	8.45 $\pm$ 4.09	5.18 $\pm$ 3.96	1.76 $\pm$ 2.18	3.66 $\pm$ 5.01
	CFA L2/3	34.76 $\pm$ 7.09	22.88 $\pm$ 6.73	18.40 $\pm$ 5.70	10.09 $\pm$ 4.65	6.77 $\pm$ 3.94	1.75 $\pm$ 2.21	5.35 $\pm$ 5.56
	CFA L5	35.57 $\pm$ 6.92	24.71 $\pm$ 7.55	20.13 $\pm$ 5.26	10.01 $\pm$ 5.00	4.81 $\pm$ 3.03	1.47 $\pm$ 1.66	3.31 $\pm$ 4.37
	CFA L6	34.78 $\pm$ 6.45	24.19 $\pm$ 7.82	18.36 $\pm$ 6.26	11.36 $\pm$ 4.55	5.37 $\pm$ 4.03	1.10 $\pm$ 1.55	4.85 $\pm$ 4.86
	STN	34.74 $\pm$ 6.76	23.76 $\pm$ 7.22	19.22 $\pm$ 5.07	10.28 $\pm$ 4.85	6.19 $\pm$ 3.63	1.23 $\pm$ 2.26	4.58 $\pm$ 4.3
50 Hz	RFA L2/3	37.53 $\pm$ 5.54	25.03 $\pm$ 7.60	21.09 $\pm$ 5.90	10.07 $\pm$ 5.42	3.66 $\pm$ 3.07	1.27 $\pm$ 1.71	1.37 $\pm$ 1.81
	RFA L5	36.23 $\pm$ 6.48	23.14 $\pm$ 6.81	20.17 $\pm$ 5.43	12.10 $\pm$ 4.94	4.43 $\pm$ 2.93	1.63 $\pm$ 2.45	2.30 $\pm$ 2.06
	RFA L6	36.87 $\pm$ 5.66	23.28 $\pm$ 6.61	21.05 $\pm$ 5.49	9.82 $\pm$ 4.74	5.72 $\pm$ 3.27	1.25 $\pm$ 2.07	2.03 $\pm$ 2.29
	CFA L2/3	36.64 $\pm$ 6.66	22.45 $\pm$ 6.51	23.37 $\pm$ 5.64	10.62 $\pm$ 4.27	3.96 $\pm$ 3.39	0.92 $\pm$ 1.41	2.04 $\pm$ 2.55
	CFA L5	36.97 $\pm$ 5.89	24.01 $\pm$ 6.75	20.96 $\pm$ 5.90	10.25 $\pm$ 4.81	3.68 $\pm$ 2.91	1.55 $\pm$ 2.05	2.58 $\pm$ 2.59

	CFA L6	36.09 ± 6.28	23.78 ±7.01	21.48± 5.57	10.96 ±4.80	3.90 ±3.36	1.52 ±1.91	2.27 ±2.21
	STN	34.91 ±6.42	27.10 ±7.77	21.46± 7.15	8.81 ±3.06	4.80 ± 3.43	1.23 ±1.86	1.65 ±2.17
140 Hz	RFA L2/3	36.45 ±5.24	27.76 ± 7.27	22.09 ±4.83	7.75 ±4.15	3.31 ±2.80	0.83 ±1.42	1.81 ±2.08
	RFA L5	36.72 ±5.56	25.81 ± 6.77	22.05± 5.63	8.88 ±4.791	3.02 ±2.96	1.30 ±1.48	2.21 ±2.12
	RFA L6	35.70 ± 5.65	25.53 ± 7.86	23.28 ±6.18	8.69 ±4.33	3.66 ±3.04	1.18 ±1.69	1.96 ±1.74
	CFA L2/3	37.65 ± 5.36	25.31 ± 6.47	21.39 ±6.04	8.93 ±3.84	4.10 ±2.73	1.06 ±1.39	1.56 ±1.78
	CFA L5	36.30 ± 6.28	25.82 ± 6.15	22.23± 5.76	8.75 ±3.71	4.25 ± 3.16	1.43 ±1.78	1.22 ±1.58
	CFA L6	36.67 ± 5.33	26.27 ± 6.30	20.99 ±5.76	8.83 ±4.37	4.27 ± 3.13	1.34 ±1.38	1.63 ±1.79
	STN	41.07 ± 6.99	23.70 ± 7.54	18.08 ± 5.72	10.55 ± 5.83	3.98 ± 3.32	0.76 ±1.33	1.85 ±1.84
180 Hz	RFA L2/3	35.38 ±7.26	27.16 ±8.79	19.67 ±6.37	10.16 ±5.21	4.32 ±2.81	1.07 ±1.67	2.24± 2.39
	RFA L5	36.81 ±7.14	25.94 ±7.46	20.23 ±6.61	9.95 ±4.50	4.42±3 .50	0.99 ±1.62	1.67 ± 1.86
	RFA L6	33.99 ±7.23	29.70 ±7.97	20.02 ±5.92	9.17 ±4.08	3.82±2 .94	1.44 ±1.83	1.87 ± 2.45
	CFA L2/3	36.47 ±7.18	25.89 ± 8.02	20.29 ±5.48	9.96 ±4.84	3.93 ±2.80	1.52 ±1.83	1.95 ± 2.06
	CFA L5	35.80 ±6.38	26.71 ± 7.81	20.94 ±6.09	9.33 ±4.02	4.57 ±2.78	0.87 ±1.22	1.77 ± 1.91
	CFA L6	35.36 ±6.46	28.30 ± 8.31	20.21 ±5.23	8.68 ± 3.73	4.87 ±3.23	1.22 ±1.75	1.37 ± 1.76

	STN	34.56	24.86±	22.06±	11.10	4.17	1.01	2.24
		± 7.65	8.25	7.91	± 6.44	±3.99	± 1.78	±2.23

Percentage of  $\beta$ -bursts of different durations in L2/3, 5, and 6 of RFA, CFA and STN. Mean + standard deviation (n=9 mice) is shown separately for each stimulation frequency, area and segment length; p-values resulting from two-sample t-tests are represented by colour: significant reductions in percentage in the 'stim on' condition as compared to 'stim off' are highlighted in orange; significant increases in percentage in the 'stim on' condition as compared to 'stim off' are highlighted in green, light colour indicates  $p < 0.001$ ; darker colour indicate  $p < 0.0001$ ; not highlighted cells indicate no significant change in percentage compared to 'stim off'. (Kreis et al., in preparation)

#### 4.2.4 High frequency stimulation modulates cortical and subcortical $\gamma$ -bursts

Next, I examined the impact of high frequency STN stimulation on the quantity and duration of  $\gamma$ -bursts in RFA, CFA and STN. The average duration of  $\gamma$ -bursts during spontaneous activity was consistent across all regions (Figure 21). Comparable to the analysis of  $\beta$ -bursts, there were no notable alterations in either the duration or number of  $\gamma$ -bursts (duration  $> 100$  ms). Similar to how I approached  $\beta$ -burst analysis, the identified  $\gamma$ -bursts were categorized into differing lengths. Roughly 40-50% of all detected  $\gamma$ -bursts in RFA, CFA and STN lasted less than 225 ms compared to less than 10% lasting longer than 600 ms during spontaneous activity.

Our analysis revealed a substantial rise in the percentage of very short (100-225 ms)  $\gamma$ -bursts in all layers of RFA and CFA during 160 Hz stimulation of the STN ( $p < 0.0001$ ). Additionally, the appearance of  $\gamma$ -bursts with a duration of 225-350 ms was significantly increased in RFA L6 ( $p < 0.001$ ), CFA L2/3 ( $p < 0.0001$ ), and CFA L6 ( $p < 0.001$ ) during high frequency stimulation (HFS) of the STN. The analysis of long  $\gamma$ -bursts ( $> 600$  ms) showed a significant decrease in  $\gamma$ -bursts in RFA and CFA (Figure 22). When examining the effect of STN HFS on  $\gamma$ -burst duration in the STN itself, I found a significant increase in the segment of 350-475 ms ( $p < 0.001$ ) (Figure 22). Furthermore, the percentage of long  $\gamma$ -bursts was decreased in the

STN during 160 Hz STN stimulation (600-725 ms:  $p < 0.001$ ; 725-800 ms:  $p < 0.01$ ;  $>800$  ms:  $p < 0.001$ ). Collectively, these results demonstrate that STN stimulation leads to an increase in short  $\gamma$ -bursts and a decrease in long  $\gamma$ -bursts.

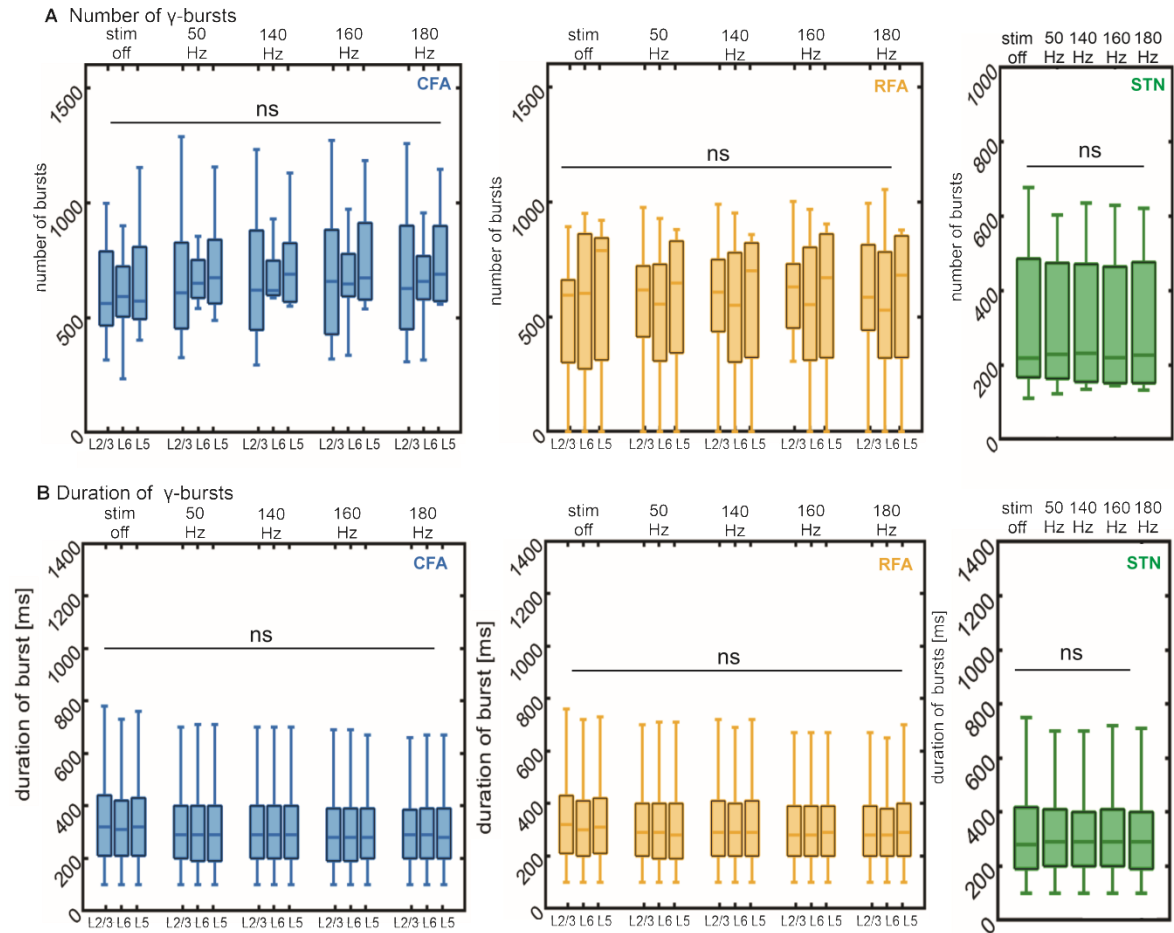


**Figure 21: High frequency STN stimulation does not change the number or duration of  $\gamma$ -bursts in RFA, CFA and STN.** Number (A) and duration (B) of short  $\gamma$ -bursts (duration  $>100$  ms) recorded in L2/3, L5, and L6 of RFA (yellow), CFA (blue) and STN (green) without (stim off) and with STN stimulation. All boxplots contain data from 9 mice. In each box, the central mark indicates the median, and the bottom and top edges of the box indicate the 25th and 75th percentiles, respectively. The whiskers extend to the most extreme data points not considered outliers. (Kreis et al., in preparation)

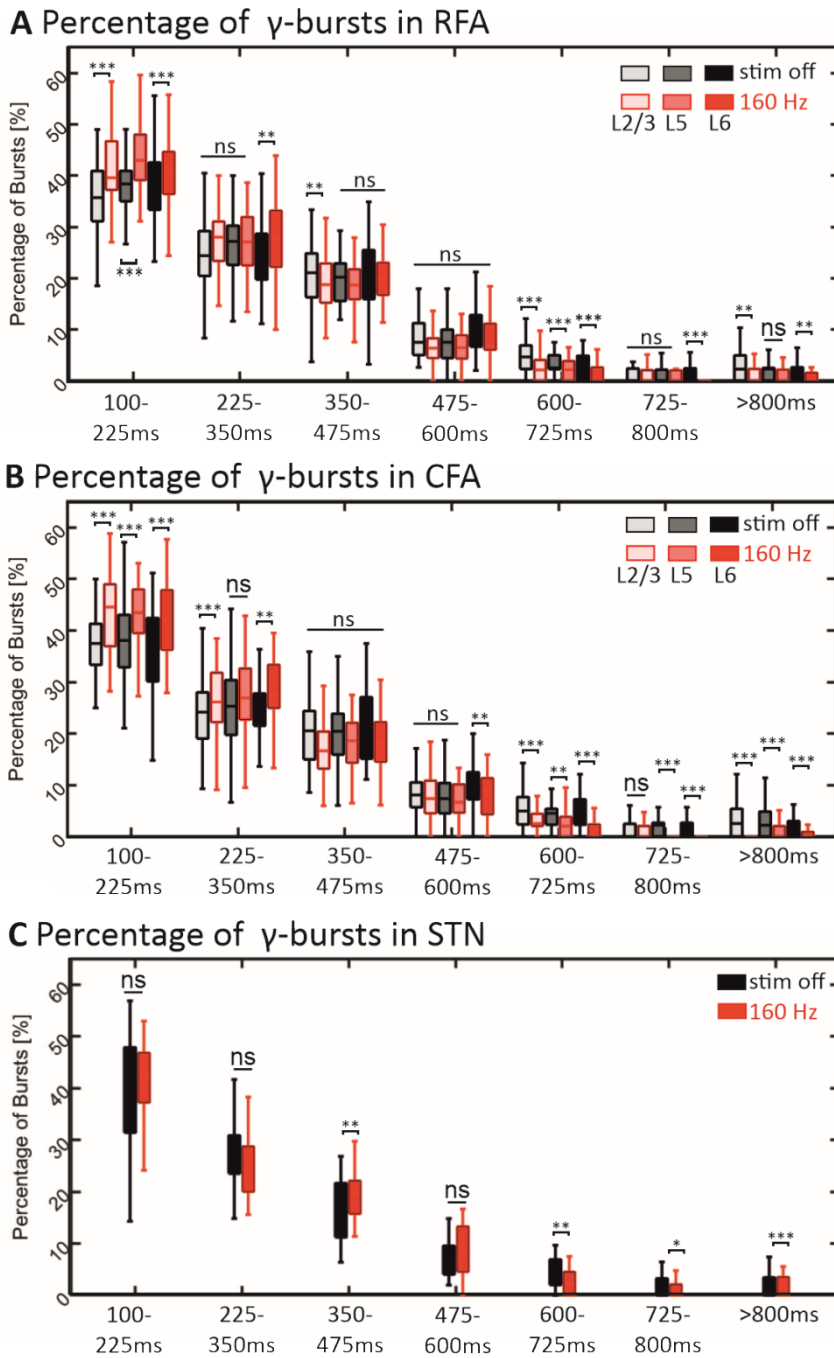


**Figure 22: Reduction in the percentage of long  $\gamma$ -bursts in RFA, CFA and STN induced by high frequency STN stimulation.** Percentage of  $\gamma$ -bursts of different lengths in L2/3, 5, and 6 of RFA (A), CFA (B) and STN (C) without (stim off, black) and with 160 Hz STN stimulation (red). All boxplots contain data from nine mice. In each box, the central mark indicates the median, and the bottom and top edges of the box indicate the 25th and 75th percentiles, respectively. The whiskers extend to the most extreme data points not considered outliers. \* represents  $p < 0.01$ ; \*\*  $p < 0.001$ ; \*\*\*  $p < 0.0001$ , ns represents not significant. (Kreis et al., in preparation)

**Table 7: Reduction of the percentage of long  $\gamma$  -bursts in RFA, CFA and STN induced by high frequency STN stimulation**

Percentage of $\gamma$ - Bursts		225-350 ms	100-225 ms	225-350 ms	350-475 ms	475-600ms	600-725 ms	725-800ms
F [Hz]	area	Mean $\pm$ std	Mean $\pm$ std	Mean $\pm$ std	Mean $\pm$ std	Mean $\pm$ std	Mean $\pm$ std	Mean $\pm$ std
Stim off	RFA L2/3	35.78 $\pm$ 7.51	24.46 $\pm$ 8.32	20.89 $\pm$ 6.36	9.22 $\pm$ 5.37	5.38 $\pm$ 4.81	1.26 $\pm$ 2.11	3.01 $\pm$ 3.63
	RFA L5	37.89 $\pm$ 6.14	26.70 $\pm$ 6.12	19.78 $\pm$ 4.74	7.87 $\pm$ 4.10	3.85 $\pm$ 2.80	1.10 $\pm$ 1.73	2.50 $\pm$ 2.81
	RFA L6	37.72 $\pm$ 7.13	24.89 $\pm$ 6.81	20.58 $\pm$ 6.45	9.74 $\pm$ 4.53	3.20 $\pm$ 2.74	1.28 $\pm$ 1.96	2.59 $\pm$ 4.39
	CFA L2/3	37.5 $\pm$ 6.67	23.84 $\pm$ 6.88	20.41 $\pm$ 6.06	8.16 $\pm$ 4.06	5.07 $\pm$ 3.95	1.30 $\pm$ 2.15	3.71 $\pm$ 3.93
	CFA L5	38.06 $\pm$ 7.55	24.72 $\pm$ 8.34	20.40 $\pm$ 6.42	7.86 $\pm$ 4.58	4.57 $\pm$ 4.03	1.70 $\pm$ 1.68	2.70 $\pm$ 3.29
	CFA L6	36.31 $\pm$ 7.94	24.00 $\pm$ 6.75	21.07 $\pm$ 7.28	9.37 $\pm$ 4.32	4.79 $\pm$ 3.76	1.78 $\pm$ 2.64	2.67 $\pm$ 3.65
	STN	39.13 $\pm$ 11.01	26.96 $\pm$ 6.40	16.45 $\pm$ 6.18	7.46 $\pm$ 4.69	4.99 $\pm$ 5.68	2.15 $\pm$ 3.37	2.86 $\pm$ 3.35
50 Hz	RFA L2/3	41.04 $\pm$ 6.43	26.77 $\pm$ 8.75	18.74 $\pm$ 6.28	7.78 $\pm$ 3.34	2.64 $\pm$ 2.83	0.98 $\pm$ 1.96	2.05 $\pm$ 2.58
	RFA L5	41.71 $\pm$ 6.79	26.59 $\pm$ 8.10	17.45 $\pm$ 6.14	8.69 $\pm$ 4.53	2.93 $\pm$ 2.68	0.43 $\pm$ 1.13	2.21 $\pm$ 1.96
	RFA L6	44.20 $\pm$ 6.57	24.79 $\pm$ 7.23	17.38 $\pm$ 6.54	7.93 $\pm$ 3.84	3.09 $\pm$ 2.60	0.87 $\pm$ 1.43	1.74 $\pm$ 2.78
	CFA L2/3	40.70 $\pm$ 6.08	28.03 $\pm$ 7.62	18.47 $\pm$ 6.49	7.02 $\pm$ 3.80	3.04 $\pm$ 2.62	0.94 $\pm$ 1.56	1.80 $\pm$ 2.25
	CFA L5	42.90 $\pm$ 6.57	26.26 $\pm$ 7.23	17.96 $\pm$ 6.54	6.99 $\pm$ 3.84	3.40 $\pm$ 2.60	0.62 $\pm$ 1.43	1.86 $\pm$ 2.78

		±6.42	±6.51	±6.05	±3.81	±2.61	±1.12	±2.66
	CFA L6	42.24	25.37	19.19	7.54	3.32	0.94	1.40
		±6.33	±6.06	±6.46	±3.38	±2.34	±1.36	±1.81
	STN	40.66	27.08	19.43	8.00'	2.37	0.61	1.85
		± 6.77	± 6.56	± 5.45	± 4.05	± 2.19	± 1.30	± 2.18
140 Hz	RFA L2/3	41.36	24.57	20.59	9.31	2.70	0.63	0.83
		±7.20	±5.63	±6.02	±4.59	±2.51	±1.24	±1.38
	RFA L5	41.07	25.38	22.16	8.17	2.02	0.63	0.56
		±6.48	±7.01	±6.71	±3.15	±2.10	±1.08	±1.21
	RFA L6	41.22	25.65	21.29	8.04	2.23	0.59	0.99
		±5.32	±6.47	±5.71	±3.66	±2.35	±1.18	±1.6
	CFA L2/3	41.46	26.04	20.27	8.28	2.77	0.62	0.57
	±5.79	±6.35	±5.42	±3.71	2.07	±1.09	±1.18	
	CFA L5	41.32	26.16	19.84	8.89	2.80	0.52	0.47
		±6.00	±7.04	±5.20	±4.25	±2.39	±1.07	±1.09
	CFA L6	41.92	26.48	18.18	9.31	2.77	0.68	0.69
		±5.69	±7.02	±4.70	±4.3	±2.50	±1.15	±1.04
	STN	39.13	29.76	19.06	7.32	3.14	0.86	0.73
		± 8.35	± 8.21	± 5.22	± 3.31	± 2.45	± 1.28	± 1.66
180 Hz	RFA L2/3	41.58	28.47	19.24	7.40	2.94	0.45	0.52
		±6.77	±6.35	±6.88	±4.26	±3.28	±0.98	±1.26
	RFA L5	43.82	29.47	18.95	6.70	2.78	0.80	0.58
		±6.27	±7.69	±6.17	±4.07	±2.95	±1.20	±1.10
	RFA L6	39.98	27.37	21.05	7.37	2.94	0.89	0.50
		±6.38	±6.13	±7.92	±3.90	±3.09	±1.42	±1.14
	CFA L2/3	43.16	27.84	20.50	6.01	2.43	0.96	0.81
	±7.42	±6.13	±5.29	±3.13	±2.15	±1.46	±1.31	
	CFA L5	43.15	29.25	20.57	6.18	2.48	0.56	0.90
		±6.13	±6.99	±5.65	±2.97	±2.08	±1.10	±1.43
	CFA L6	41.64	29.67	19.71	6.66	2.66	0.60	0.93

		±7.02	±6.04	±5.95	±3.35	±2.15	±1.09	±1.57
	STN	41.93	25.48	18.42	7.96	4.03	0.55±	1.62
		± 11.29	± 7.60	± 5.75	± 4.06	± 3.26	0.98	± 3.30

Percentage of  $\gamma$  -bursts of different duration in L2/3, 5, and 6 of RFA, CFA and STN. Mean + standard deviation (n=9 mice) is shown separately for each stimulation frequency, area and segment length; p-values resulting from two-sample t-tests are represented by colour: significant reductions in percentage in the 'stim on' condition as compared to 'stim off' are highlighted in orange; significant increases in percentage in the 'stim on' condition as compared to 'stim off' are highlighted in green, light colour indicates  $p < 0.001$ ; darker colour indicate  $p < 0.0001$ ; not highlighted cells indicate no significant change in percentage compared to 'stim off' (Kreis et al, in preparation)

#### 4.2.5 High frequency STN stimulation reduces functional connectivity between RFA, CFA and STN

The next step was to determine whether high frequency stimulation of the STN alters the frequency- and layer-specific functional connectivity between the two motor cortical regions, RFA and CFA, as well as the STN. To investigate this, I analyzed the LFP coherence of spontaneous activity recorded in layers 2/3, 5, and 6 from RFA and CFA, as well as from STN. Additionally, I calculated the LFP coherence during high frequency STN stimulation with different stimulation frequencies. The resulting coherence was averaged across all nine animals for each stimulation frequency and the "stim off" condition, and the resulting spectra are shown in Figure 23. The results revealed significant coherence between all recording sites in RFA, CFA, and STN in both the "stim off" condition and during the application of all tested stimulation frequencies. The baseline coherence was stronger between layers 5 and 6 of RFA and CFA as compared to layer 2/3 RFA (Table 8, Table 9) and CFA (L5:  $p < 2.2e^{-15}$ , L6:  $p < 1.9e^{-24}$ ). This is consistent with our previous findings (Kreis et al. 2022). Furthermore, I found that the coherence between RFA and CFA was significantly higher than the coherence between the STN and the two cortical areas for all layer combinations and stimulation conditions.

My research indicates a notable decrease in coherence between RFA, CFA, and STN during high frequency STN stimulation in the  $\beta$ - and high  $\gamma$ -frequency band (as depicted in Figure 24). Utilizing LMM, I discovered a significant effect of STN stimulation on LFP coherence between all RFA and CFA layers in the  $\beta$ - and high  $\gamma$ -frequency band. Specifically, I observed that 160 Hz STN stimulation resulted in a significantly greater decrease in LFP coherence between all three areas as compared to 50, 140, or 180 Hz stimulation (Figure 24). The strongest reduction was evident in the high  $\gamma$ -frequency band, particularly between L6 RFA and L6 CFA during 160 Hz STN stimulation (as shown in Figure 24,  $p < 0.005$ ).

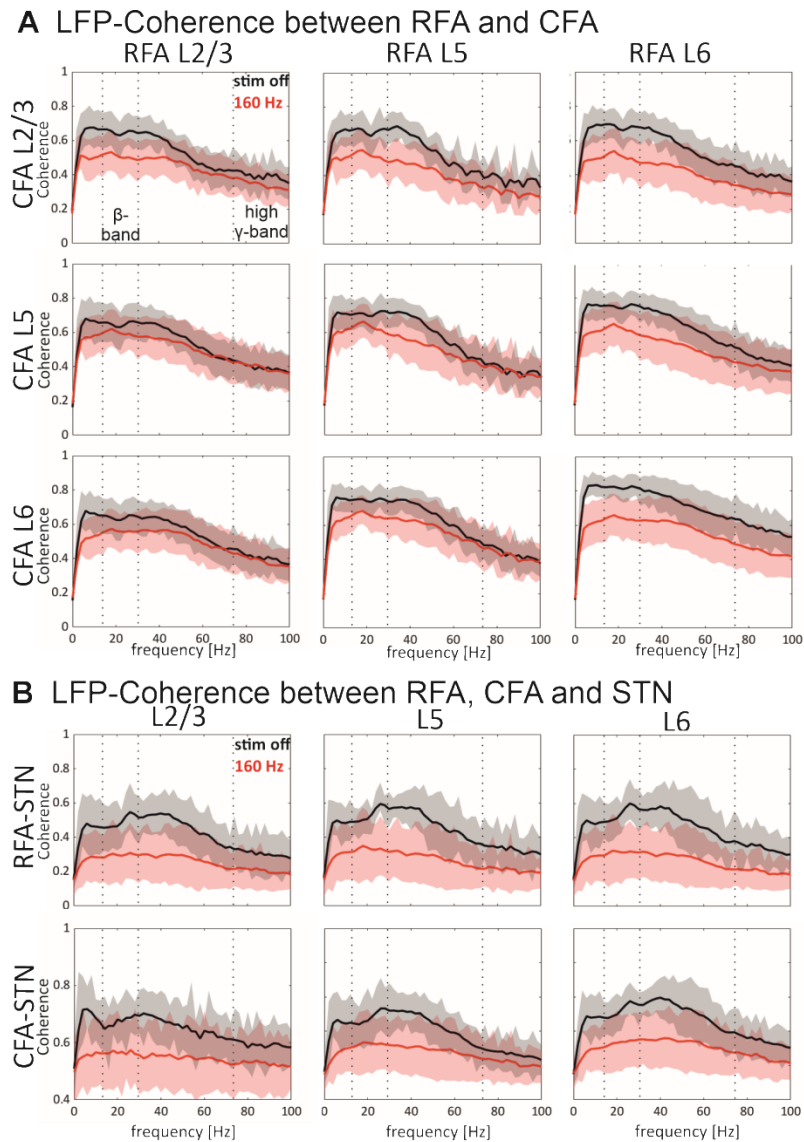


**Figure 23: Reduction of LFP coherence between RFA, CFA and STN during 160 Hz STN stimulation.** Coherence between CFA, RFA and STN without (black) and with STN stimulation (red). (A) Comparison of LFP coherence between L2/3, L5, and L6 of RFA and CFA without (black) and with 160 Hz STN stimulation (red). (B) Comparison of LFP coherence between STN and L2/3, L5, and L6 of RFA and CFA without and with 160 Hz STN stimulation. Lines represent averaged across 9 mice; the shaded area indicates standard deviation. Dotted lines indicate the borders of the  $\beta$  and high  $\gamma$ -frequency bands. (Kreis et al., in preparation)

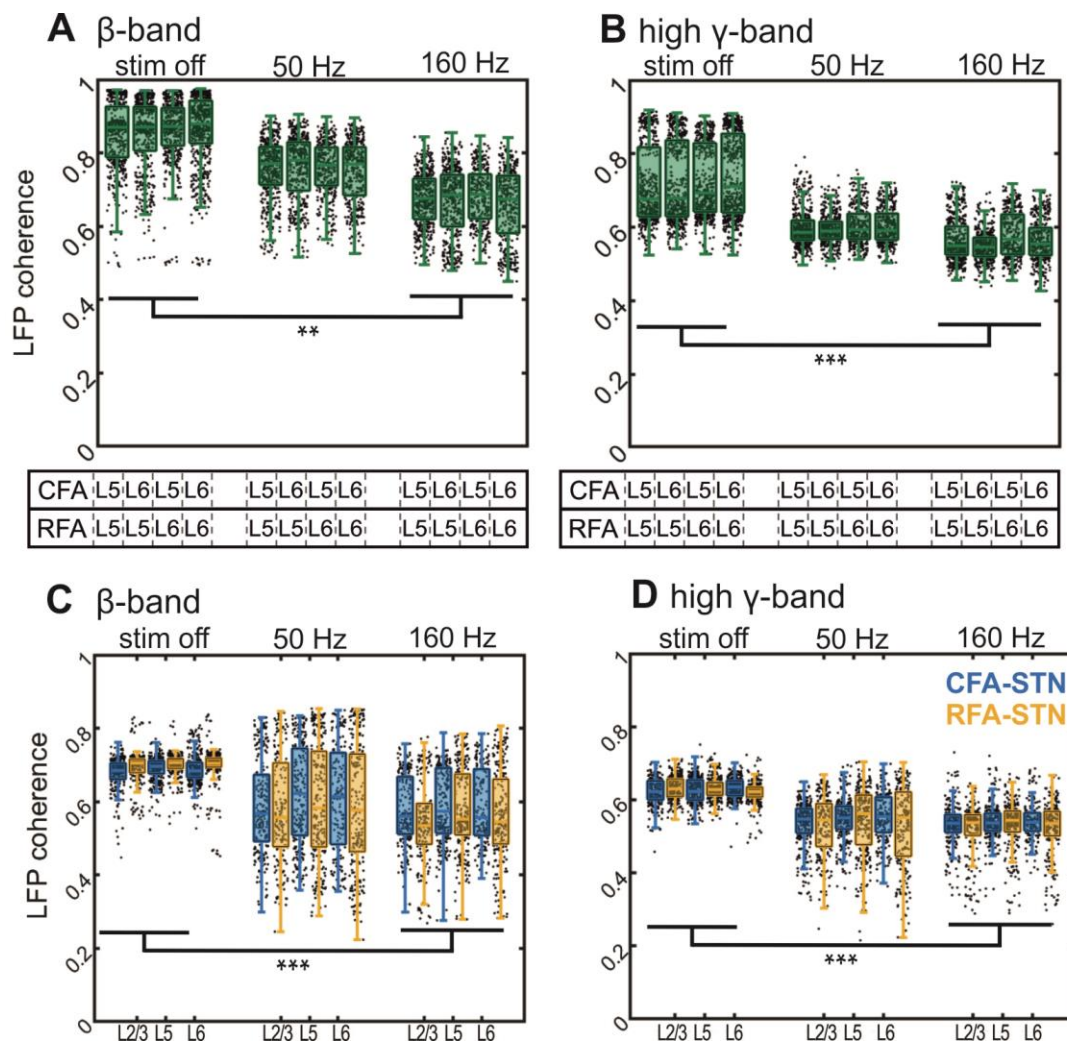


**Figure 24: STN stimulation induced reduction in LFP coherence between RFA, CFA and STN in the  $\beta$ - and high  $\gamma$ -frequency band.** Coherence between CFA, RFA and STN without (left) and with STN stimulation. (A, B) Comparison of LFP coherence between L2/3, 5, and 6 of RFA and CFA without and with STN stimulation. (C, D) Comparison of LFP coherence between STN and L2/3, 5, and 6 of RFA and CFA without and with STN stimulation. All boxplots contain data from 9 mice. In each box, the central mark indicates the median, and the bottom and top edges of the box indicate the 25th and 75th percentiles, respectively. The whiskers extend to the most extreme data points not considered outliers. \* represents  $p < 0.01$ ; \*\*  $p < 0.001$ ; \*\*\*  $p < 0.0001$ . (Kreis et al., in preparation)

**Table 8: Reduction in  $\beta$ -band LFP coherence between RFA and CFA during high frequency STN stimulation; \*\*\*  $p < 0.001$**

$\beta$ - frequency band	Spon	50 Hz		140 Hz		160 Hz		180 Hz	
	Mean $\pm$ std	Mean $\pm$ std	Stat off- 50	Mean $\pm$ std	Stat off- 140	Mean $\pm$ std	Stat off- 160	Mean $\pm$ std	Stat off- 180
RFA L2/3 – CFA L2/3	0.80 $\pm$ 0.09	0.67 $\pm$ 0.10	***	0.65 $\pm$ 0.10	***	0.66 $\pm$ 0.10	***	0.68 $\pm$ 0.11	***
RFA L2/3 – CFA L5	0.84 $\pm$ 0.09	0.72 $\pm$ 0.10	***	0.70 $\pm$ 0.11	***	0.69 $\pm$ 0.09	***	0.72 $\pm$ 0.13	**
RFA L2/3 – CFA L6	0.83 $\pm$ 0.09	0.68 $\pm$ 0.10	***	0.67 $\pm$ 0.10	***	0.66 $\pm$ 0.11	***	0.68 $\pm$ 0.11	***
RFA L5 – CFA L2/3	0.80 $\pm$ 0.09	0.70 $\pm$ 0.09	***	0.69 $\pm$ 0.11	***	0.64 $\pm$ 0.07	***	0.70 $\pm$ 0.11	***
RFA L6 – CFA L2/3	0.80 $\pm$ 0.10	0.72 $\pm$ 0.10	***	0.69 $\pm$ 0.11	***	0.63 $\pm$ 0.09	***	0.68 $\pm$ 0.13	***

**Table 9: Reduction in high  $\gamma$ -band LFP coherence between RFA and CFA during high frequency STN stimulation; \*\*\*  $p < 0.001$**

high $\gamma$ - frequency band	Spon	50 Hz		140 Hz		160 Hz		180 Hz	
	Mean $\pm$ std	Mean $\pm$ std	Stat off-50	Mean $\pm$ std	Stat off- 140	Mean $\pm$ std	Stat off- 160	Mean $\pm$ std	Stat off- 180
RFA L2/3 – CFA L2/3	0.68 $\pm$ 0.09	0.60 $\pm$ 0.06	***	0.61 $\pm$ 0.06	***	0.61 $\pm$ 0.09	***	0.61 $\pm$ 0.06	***
RFA L2/3 – CFA L5	0.72 $\pm$ 0.11	0.61 $\pm$ 0.06	***	0.63 $\pm$ 0.06	***	0.61 $\pm$ 0.10	***	0.62 $\pm$ 0.06	***
RFA L2/3	0.71 $\pm$	0.59 $\pm$	***	0.61 $\pm$	***	0.61 $\pm$	***	0.61 $\pm$	***

<b>- CFA L6</b>	0.09	0.05		0.06		0.09		0.05	
<b>RFA L5 -</b>	0.68±	0.59±	***	0.61	***	0.56±	***	0.59±	***
<b>CFA L2/3</b>	0.09	0.05		0.06		0.05		0.05	
<b>RFA L6 -</b>	0.69±	0.58±	***	0.62±	***	0.54±	***	0.59±	***
<b>CFA L2/3</b>	0.09	0.04		0.07		0.04		0.06	

#### 4.2.6 Effect of high frequency STN stimulation on the effective connectivity between RFA, CFA and STN

I examined the impact of 160 Hz stimulation of the STN on the connectivity between RFA, CFA, and STN. To quantify the effect of high frequency stimulation on the direction of connectivity between RFA, CFA, and STN, I calculated the tPDC of the recorded neuronal activity (Figure 25).

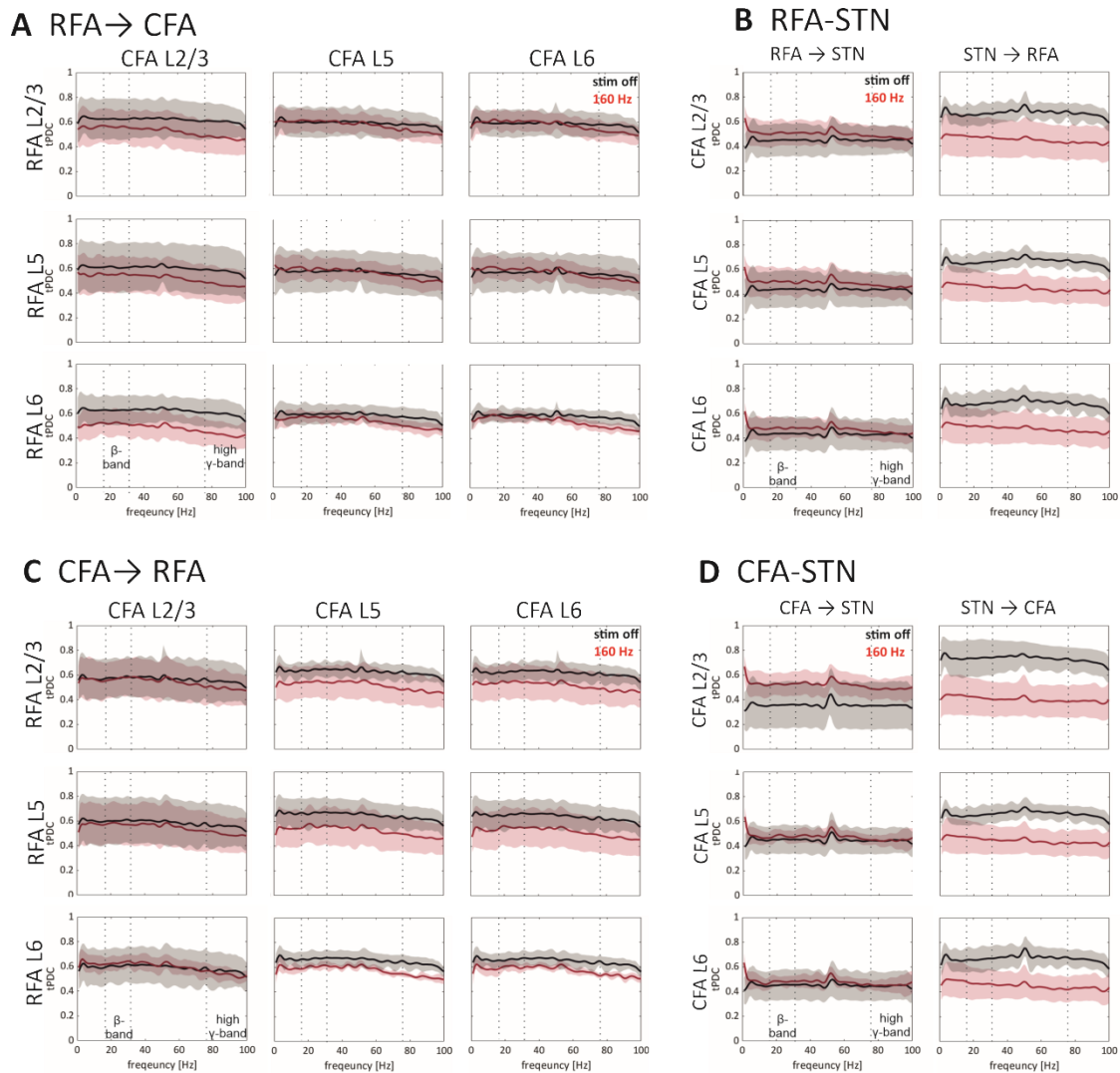


**Figure 25: High frequency STN stimulation influences the information flow between RFA, CFA and STN.** tPDC connectivity between CFA, RFA and STN without (black) and with STN stimulation (red). Layer-specific flow of information between RFA, CFA and STN. tPDC between cortical areas for the direction of (A) RFA→CFA, and (C) the direction of CFA→RFA. tPDC connectivity between (B) STN and RFA and (D) STN and CFA. Lines represent averaged across 9 mice; the shaded area indicates standard deviation. Dotted lines indicate the borders of the beta and high  $\gamma$ -frequency bands. (Kreis et al, in preparation)

I calculated the mean tPDC for each layer combination in the  $\beta$ - and high  $\gamma$ -frequency band for the direction from RFA toward CFA, as well as vice versa (as shown in Figure 26). I discovered that 160 Hz STN stimulation did not significantly affect the tPDC between RFA and CFA in the  $\beta$ -frequency band. However, when I analyzed the connectivity in the high  $\gamma$ -frequency band, I found that 160 Hz STN stimulation resulted in a significant reduction in

information transmission from CFA L5 and L6 to RFA L6 ( $p < 0.001$ ). Additionally, high frequency STN stimulation led to a significant reduction in tPDC for the direction of RFA L6 to CFA L2/3 ( $p < 0.01$ ).

Finally, the tPDC for the connectivity between STN and layers 2/3, 5, and 6 of RFA and CFA in the  $\beta$ - and high  $\gamma$ -frequency band was calculated (Figure 27). No significant alteration in the direction of connectivity from cortical areas RFA and CFA towards STN was observed ( $p > 0.05$ ). However, my findings indicate a noteworthy decrease in information transmission from the STN to all layers of RFA and CFA across both frequency bands. This impact was notably more pronounced for the connectivity from STN to CFA compared to that from STN to RFA (L2/3:  $p < 2.6173e^{-04}$ ; L5:  $p < 4.7962e^{-06}$ ; L6  $p < 2.1189e^{-06}$ ).

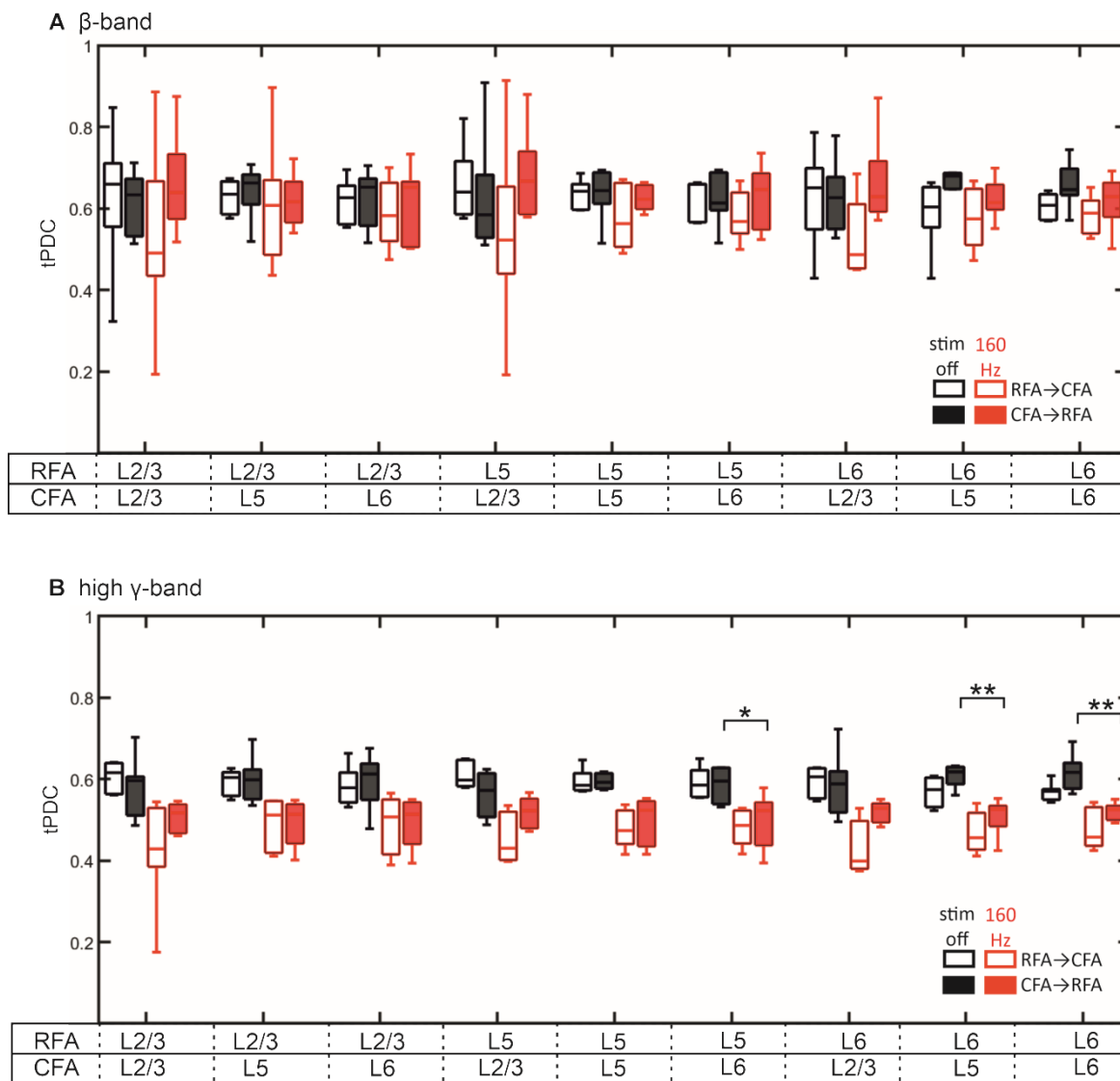


**Figure 26: High frequency STN stimulation influences the information flow between L6 of RFA and CFA in the high  $\gamma$ -frequency band.** The tPDC connectivity between L2/3, 5 and 6 of RFA and CFA. Layer-specific directionality of information flow between L2/3, 5, and 6 of RFA and CFA in  $\beta$ - (A) and high  $\gamma$ -frequency band (B) without STN stimulation (light green, light blue) and with 160 Hz STN stimulation (dark green, dark blue). Boxplot of tPDC for the directions RFA→CFA (green) and CFA→RFA (blue). All boxplots contain data from 9 mice. In each box, the central mark indicates the median, and the bottom and top edges of the box indicate the 25th and 75th percentiles, respectively. The whiskers extend to the most extreme data points not considered outliers. Each analyzed channel combination is represented by a dot. \* represents  $p < 0.01$ ; \*\*  $p < 0.001$ . (Kreis et al, in preparation)

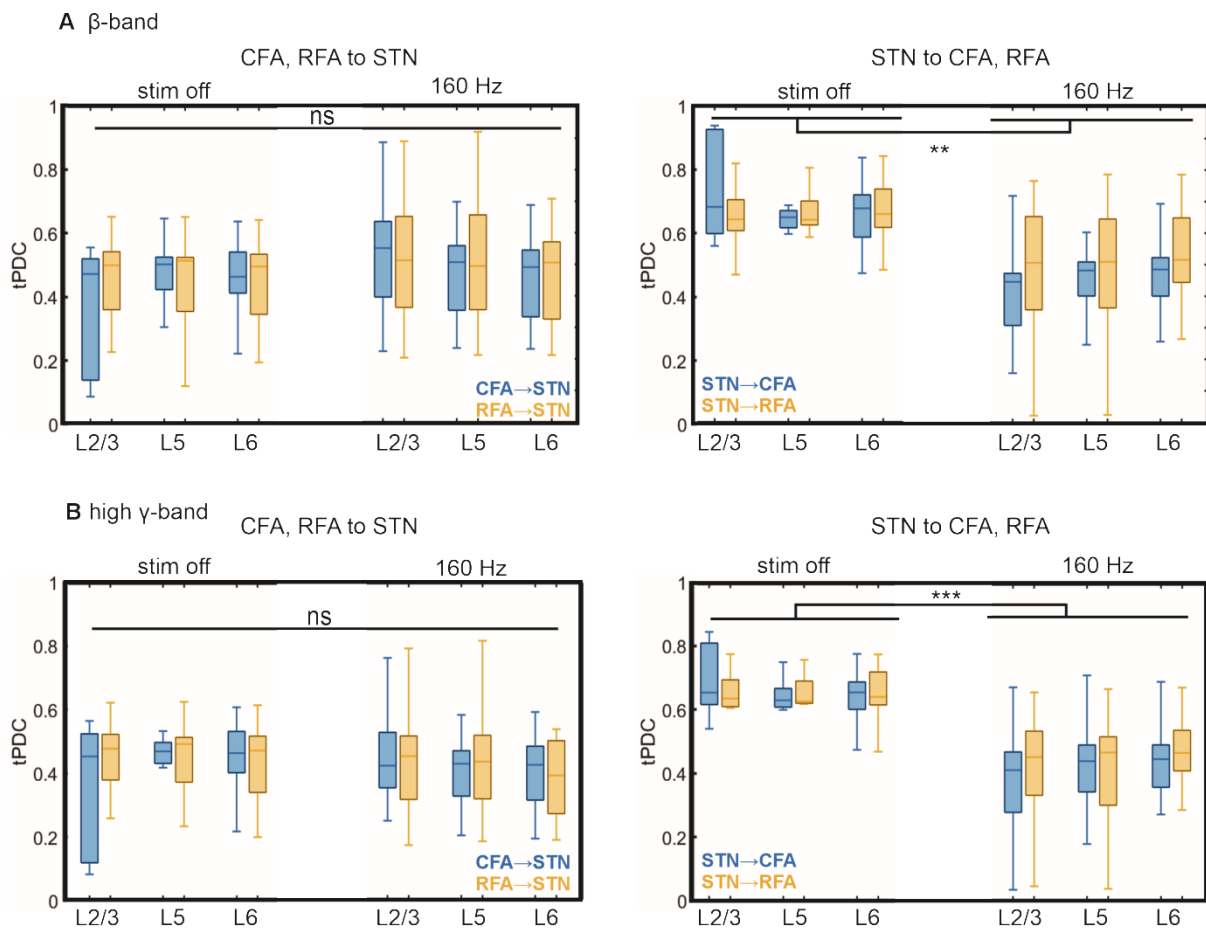


**Figure 27: High frequency STN stimulation reduces the flow of information from STN towards RFA and CFA but not from RFA and CFA towards STN.** tPDC connectivity between STN and L2/3, 5 and 6 of RFA and CFA. Layer-specific directionality of information flow between STN and L2/3, 5, and 6 of RFA and CFA in  $\beta$ - (A) and high  $\gamma$  (B) frequency band, with and without STN stimulation (left) and with 160 Hz STN stimulation for the direction of RFA and CFA towards STN (left) and STN towards RFA, CFA (right). Boxplots of tPDC for the connectivity between STN-CFA (orange) and STN-RFA (purple); All boxplots contain data from 9 mice. In each box, the central mark indicates the median, and the bottom and top edges of the box indicate the 25th and 75th percentiles, respectively. The whiskers extend to the most extreme data points not considered outliers. Each analyzed channel combination is represented by a dot. \*\* represents  $p < 0.001$ ; \*\*\*  $p < 0.0001$ . (Kreis et al, in preparation)

### 4.3 Results summary

The objective of this study was to investigate the impact of high frequency stimulation of the STN on the premotor-motor-STN network in wildtype mice. To accomplish this, I first analysed the characteristics of, and connectivity between the two motor cortical regions, RFA and CFA, in wildtype mice (Aim 1). Following this, the aim was to determine how different STN stimulation frequencies affect the RFA-CFA-STN network (Aim 2). To achieve this, an anaesthesia protocol was adapted that enabled stable recordings to be made over an extended period of time without the need for repeated anaesthetic injections. Subsequently, the craniotomy positioning and angling of electrodes was established to facilitate the placement of three separate electrodes and connected headstages in the limited available space, to allow for simultaneous recordings from STN as well as Layers 1, 2/3, 5 and 6 of RFA and CFA. This was only possible by inserting the electrode designated for STN recordings from the contralateral hemisphere at an angle of 52°. I then recorded spontaneous activity simultaneously in all layers of RFA and CFA and applied a combination of spectral power, functional and effective connectivity analysis to the resulting data. Major differences in oscillatory activity between the premotor and primary motor areas were found in the  $\beta$  and high  $\gamma$ -frequency bands. Findings from my study show that CFA exhibits significantly higher spectral power in multiple frequency bands, demonstrating that the two motor areas, RFA and CFA, can be topologically characterized by electrophysiological proxies (Aim 1.1). Additionally, I found that RFA and CFA are functionally strongly interconnected and show layer- and frequency-specific patterns of connectivity (Aim 1.2). The information flow predominantly followed the direction from RFA towards CFA in the  $\beta$ - and high  $\gamma$ -frequency band. The designed SEM model demonstrated significant causal relations between LFP power, coherence, TPDC, and SU activity in RFA L5 to CFA L2/3 in the  $\beta$ - and high  $\gamma$ -frequency band. By collaborating with Prof. Muthuraman, I was able to compare the results gathered from the mouse motor cortex data with EEG data recorded in healthy humans at rest, thus addressing the question of whether the connectivity within the RFA-CFA network can be used as a valid model for the human PMC-M1 network (Aim 1.3). Our data revealed strong similarities between human PMC-M1 functional connections and the RFA-CFA network in the mouse, providing further evidence for the validity of the model (Kreis et al. 2022).

The second section of my thesis was to identify frequency- and layer-specific effects of high frequency STN stimulation on mouse motor cortical areas (Aim 2). To achieve this goal, I applied a wide range of STN stimulation frequencies with varying intensities to the STN of anaesthetized, head-fixed mice while simultaneously recording neuronal activity from Layers 2/3, 5, and 6 of RFA and CFA as well as from all non-stimulation contacts within the STN. The network of human homologous brain areas represents the backbone of the therapeutic effects of DBS in patients with movement disorders. Therefore, this analysis adds valuable information on the mechanism of action of DBS.

The different stimulation settings were applied in a randomized order, separated by a 10 min recording of spontaneous activity, which was sufficient to allow the neuronal activity in all three areas to return to baseline activity (Figure 11-16). In my experiments, I identified 160 Hz as the most effective stimulation frequency, which is consistent with previous studies showing that the stimulation frequency used in mice is typically slightly higher than what is most effective in human Parkinson's disease patients.

Similarly to the analysis of the RFA-CFA network, I applied a combination of spectral power, effective and functional connectivity in order to study the effect of high frequency STN stimulation in the RFA-CFA-STN network. Additionally, I performed burst analysis. I found a significant reduction of  $\beta$ -power in RFA, CFA and STN. In contrast to that, the high  $\gamma$ -power was reduced only in the STN (Aim 2.1). Furthermore, my results show that high frequency STN stimulation decreases the amount of long bursts in both the  $\beta$ - and high  $\gamma$ -frequency bands in RFA, CFA, and STN (Aim 2.2 and 2.3). My data demonstrates that high frequency STN stimulation reduces the synchronization between RFA and CFA in the  $\beta$ - and high  $\gamma$ -frequency band (Aim 2.4). Lastly, the analysis showed, that high frequency STN stimulation reduces the strength of functional and effective connectivity between RFA, CFA, and STN specifically in the direction of the STN towards the cortical areas (Aim 2.5).

## 5 Discussion

### 5.1 Mouse motor cortical areas RFA and the CFA as a model for human premotor-motor network

Understanding the physiological patterns of motor network connectivity is crucial for elucidating aberrant oscillatory transformations and constructing robust translational models of movement disorders. Several studies have explored the function and connectivity between the primary motor cortex (M1) and premotor cortex (PMC) in humans (Johansen-Berg et al. 2004; Groppa and Schlaak et al. 2012). However, data on the organization and connectivity of different areas of the motor cortex in mice are scarce compared to humans and non-human primates (Tennant et al. 2011). As mouse models are widely used as a tool in research on human movement disorders (Ilderberg et al. 2012; Morin et al. 2014), it is essential to obtain more detailed information on the connectivity of the PMC-M1 network in mice. Therefore, the first section of my thesis aimed to analyze the properties of the connectivity between the two motor cortical areas RFA and CFA in wildtype mice (Aim 1) and to compare the results to the PMC-M1 network in healthy human subjects. The data on the human subjects was recorded and analyzed by my collaborator, Prof. Dr.-Ing. Muthuraman Muthuraman, while I recorded and analyzed the mouse data and performed the statistical analysis of both datasets.

#### 5.1.1 Spontaneous activity in the mouse motor cortex and its similarity to the human PMC-M1 network

I utilized intracortical MEAs to record spontaneous activity in layers 2/3, 5, and 6 of RFA and CFA in lightly anaesthetized adult C57Bl6-N mice. To estimate functional connectivity, I employed LFP coherence and studied the direction and strength of effective connectivity using SU cross-correlations and TPDC.

Prof. Dr.-Ing. Muthuraman performed high-density EEG recordings on healthy human subjects at rest in a seated position with eyes closed. After filtering and source reconstruction, the EEG data underwent a highly similar analysis pipeline as the mouse LFP

data to ensure comparability. For more information on EEG data processing, please refer to Kreis et al. (2022).

My findings showed significantly higher spectral power across all analyzed frequencies in the M1 compared to the PMC (Kreis et al. 2022). This result was expected since the PMC plays a crucial role in sensorimotor and visuomotor integration during action control (Chouinard and Paus 2006).

When analyzing the mouse data, I observed that both the RFA and the CFA displayed the strongest spontaneous activity in the delta and theta frequency range, with a decrease in spectral power from  $\alpha$  to  $\beta$  and  $\gamma$ -frequency bands. The CFA demonstrated higher power than the RFA, which is consistent with the results on spectral power differences between the human PMC and M1 (Kreis et al. 2022). My results confirm the findings of (Das A et al. 2023), who showed higher neuronal activity in CFA compared to RFA in freely moving mice. The higher mean firing rate of SU in the RFA compared to that in the CFA suggests that these two are electrophysiologically distinct areas.

### 5.1.2 Functional and effective connectivity between the mouse RFA and CFA and its similarities to the human PMC-M1 network

The analysis of functional connectivity within the motor cortex of mice revealed strong synchronization between all layer combinations of the red fluorescent axonal tracer (RFA) and the cone-shaped fluorescent axonal tracer (CFA) across a broad range of frequencies. The highest coherence was observed in the  $\beta$ -band between the RFA L5 and L6 and CFA L6. These findings align with previous studies showcasing anatomical connections between all RFA and CFA layers (Rouiller et al. 1993; Hira et al. 2013). Hira et al. (2013) demonstrated extensive anatomical connections between deeper layers of RFA and CFA.

The functional connectivity between the human prefrontal cortex (PMC) and motor cortex (M1) was also analyzed, and high coherence was found between the EEG signals recorded from both regions, with the highest coherence in the  $\beta$ -frequency band. Synchronization in the  $\beta$ -frequency band is typically associated with the processing of sensorimotor information during resting states (Engel and Fries 2010; Athanasiou et al. 2018).

Although the mouse data were collected under anaesthesia, the coherence between RFA and CFA was comparable to the coherence between PMC and M1 in humans and was significantly higher in the  $\beta$ -band compared to other frequency bands. Using tPDC analysis to analyse the directionality of connectivity between the RFA and CFA, I found reciprocal interactions in all pairs of layer combinations between the two areas, which is consistent with previous studies (Rouiller et al. 1993; Harrison et al. 2012; Hira et al. 2013; Bukhari et al. 2018). The direction of information flow was stronger from RFA towards CFA for all layer combinations, and this difference in transmission strength was significant in all frequency bands for interactions between all RFA layers and CFA layer 2/3. Our results indicate that RFA has a strong modulatory influence on neural activity in CFA and support the findings of (Deffeyes et al. 2015), who applied intracortical microstimulation techniques and found that RFA has a strong modulatory effect on CFA activity.

When analyzing the direction of information transmission between the PMC and M1 in humans at rest, we found strong bidirectional connectivity between both areas, similar to the mouse data (Kreis et al. 2022). As in mice, the information flow in  $\beta$ - and low to high  $\gamma$ -frequency bands from the PMC towards the M1 was significantly stronger compared to the opposite direction, confirming that the PMC strongly influences neural activity in the M1 (Münchau et al. 2002; Chouinard and Paus 2006).

This electrophysiological data showed, that the mouse RFA is highly similar to the human premotor cortex. This is in line with previous studies, that used anatomical tracing to show strong similarities between the cortical connections between mouse RFA and the primate PMC (Urban Iii et al. 2024).

### 5.1.3 Oscillations at $\beta$ - and $\gamma$ -frequencies as biomarkers in the premotor-motor network

Neuronal oscillatory signals represent a fundamental aspect of brain function, orchestrating the transfer of information across diverse brain regions. These oscillations are indispensable for promoting physiological brain activity and coordinating various functions, including both motor control and cognitive processes (Engel and Fries 2010). Gamma band oscillations, characterized by their high frequency activity, have been implicated in a range of cognitive

processes such as attention, multisensory integration, and sensorimotor coordination (Engel and Fries 2010). On the other hand,  $\beta$ -frequency band synchronization in the motor cortex is associated with the maintenance of the current body position, reflecting a preparatory state for movement execution (Engel and Fries 2010).

In my study, I investigated the power, functional connectivity, and effective connectivity within the  $\beta$ - and high  $\gamma$ -frequency bands in both the mouse RFA-CFA network and the human PMC-M1 connections. My results revealed significant, layer-specific differences in these parameters, highlighting their potential as biomarkers for analyzing the premotor-motor network in both species. Specifically, alterations in  $\beta$ - and high  $\gamma$ -band activity may serve as indicators of underlying physiological processes within the motor network, offering valuable insights into motor function and dysfunction.

Moreover, our study unveiled striking similarities between the mouse RFA-CFA network and the human PMC-M1 network, underscoring the translational relevance of mouse models in studying premotor-motor connectivity. By validating the mouse RFA-CFA network as a suitable model for such analyses, our findings pave the way for future translational research endeavours aimed at unravelling the pathophysiology of movement disorders and developing innovative therapeutic interventions.

In conclusion, this study provides valuable insights into the role of neuronal oscillatory signals in facilitating physiological brain activity and coordinating movements and cognitive functions. Identifying potential biomarkers for analyzing the premotor-motor network in both humans and mice offers a promising avenue for advancing translational research. These findings hold significant implications for understanding motor function and developing targeted interventions for movement disorders in both preclinical and clinical settings.

## 5.2 Effect of high frequency STN stimulation on the RFA-CFA-STN network

Using multi-electrode-arrays, I simultaneously recorded neuronal activity in L2/3, 5, and 6 of RFA and CFA, as well as in the STN of anaesthetized wildtype mice with and without high frequency electrical stimulation of the STN. I employed a combination of spectral power and burst analyses along with effective and functional connectivity to investigate the impact of

high frequency STN stimulation in the RFA-CFA-STN network (Aim 2). My findings indicate that high frequency STN stimulation decreases synchronization between RFA and CFA in the  $\beta$ - and high  $\gamma$ -frequency band; it also reduces functional and effective connectivity strength between RFA, CFA, and STN specifically from the direction of the STN towards cortical areas. Furthermore, my research reveals that high frequency STN stimulation reduces the occurrence of long bursts in both  $\beta$ - and  $\gamma$ -frequency bands within RFA, CFA and STN. My findings reveal that different stimulation frequencies alter both the intensity and direction of connections within the RFA-CFA-STN network.

### **5.2.1 High frequency STN stimulation induces a decrease in spectral LFP power in the high $\gamma$ -frequency band in RFA, CFA and STN**

Using LFP power analysis, I demonstrated that  $\beta$ -power in layers L2/3, 5, and 6 of RFA and CFA is effectively modulated only by high frequency stimulation of the STN. In contrast to that, all tested stimulation frequencies led to a significant reduction of  $\beta$ -power in the STN itself. These results are consistent with previous human studies that showed a reduction in STN  $\beta$ -power during high frequency stimulation (Kühn et al. 2009). Results from behavioural experiments conducted on freely moving mice and rats revealed significant improvement in movement speed, duration of movement, and enhanced paw coordination during the application of STN stimulation with very low frequencies, as low as 15 Hz (Brocker et al. 2017; Schor and Nelson 2019). Therefore, changes in neuronal activity in the STN with 50 Hz stimulation, as observed in my experiments, are expected.

In addition, I found that STN stimulation significantly reduced high  $\gamma$  power in the STN, while not affecting high  $\gamma$  power in the RFA and CFA cortical areas. These results suggest that STN-DBS modulates the physiological dynamics within the STN (Herz et al. 2022). Previous optogenetic studies have reported activation of L5 in the primary motor cortex (M1) neurons during STN stimulation (Gradinaru et al. 2009; Li Q et al. 2012), suggesting an antidromic activation of the hyper-direct pathway that connects the STN and M1 (Li Q et al. 2012). Axon collaterals of pyramidal neurons in L5 of the motor cortex form synapses with L2/3 and L6 neurons (Cowan and Wilson 1994). Therefore, antidromic activation of the CFA L5 is likely to engage several cortical layers (Li et al. 2007). In line with previous findings, Li et al. (2007)

reported changes in membrane potential and spiking activity in neurons located in multiple layers of the mouse motor cortex during STN stimulation.

### 5.2.2 High frequency STN stimulation reduces the occurrence of long $\beta$ - and $\gamma$ -bursts

There is widespread agreement that pathological  $\beta$ -band activity serves as a robust biomarker for motor symptoms in PD (Ni et al. 2001; Benazzouz et al. 2002). Nevertheless, temporal clusters comprising short and long burst activity may additionally contribute to the pathological transformation of physiological activity (Duchet et al. 2021). Recent studies have proposed that longer bursts or bursts exhibiting characteristic non-linearity are related to bradykinesia in PD (Deffeyes et al. 2015; Torrecillos et al. 2018). Short  $\beta$ -bursts, on the other hand, are indicative of physiological activity in the motor cortex (Deffeyes et al. 2015; Torrecillos et al. 2018; Duchet et al. 2021; Lai et al. 2022). Consequently, I was interested in determining whether high frequency stimulation of the STN would attenuate the probability of appearance and duration of long  $\beta$ -bursts in the RFA, CFA, and STN. Using a burst detection method previously described by Tinkhauser et al. (2017), I demonstrated that high frequency stimulation of the STN resulted in an increased number of short bursts (100-475 ms) in the  $\beta$ -frequency band. Moreover, I showed a reduction in the percentage of long (>800 ms) bursts in all layers of the RFA and CFA, as well as in the STN. The attenuation of  $\beta$ -band activity in the sensorimotor cortex during high frequency stimulation of the STN is attributable to reduced activity in the cortical-subcortical oscillatory network (Tinkhauser et al. 2017). Although  $\beta$  oscillations continue to occur, the network is less likely to sustain extended burst periods of 800 milliseconds to seconds, which suggests a shift towards more physiological  $\beta$  activity. Furthermore, the current study presents findings indicating that there is no change in the overall count of  $\beta$ -bursts following STN stimulation. However, there is a notable decrease in the proportion of prolonged  $\beta$ -bursts. This suggests a transition towards more physiological activity within these three analysed regions, as shorter bursts are linked to less clinical impairment while long bursts indicate motor impairment. This shift may directly contribute to the clinical outcomes in PD patients with DBS implants. While bursts in the  $\beta$ -band may forecast poorer performance on motor and sensory tasks,  $\gamma$ -bursts could foretell improved performance on working memory tasks (Lundqvist et al. 2016; Shin

et al. 2017; Torrecillos et al. 2018; Becker et al. 2020; Muthuraman et al. 2020). Consequently, my interest lies in examining how high frequency STN stimulation affects bursting activity within the  $\gamma$ -frequency band. Past studies have revealed that both DBS and levodopa intake can enhance finely tuned gamma oscillations in the STN. Nevertheless, it remains uncertain how STN stimulation impacts the occurrence of  $\gamma$ -bursts. My study aimed to analyze the effect of STN stimulation on  $\gamma$ -bursts in STN and L2/3, 5 and 6 of RFA and CFA by shifting from long  $\gamma$ -bursts to shorter  $\gamma$ -bursts without reducing the total number of bursts. This indicates a shift in  $\gamma$ -burst appearance away from bursts longer than 500 ms, which is uncharacteristic of healthy subjects (Powanwe and Longtin 2019).

### 5.2.3 High frequency STN stimulation induces a reduction in functional and effective connectivity between RFA, CFA and STN

My research utilized LFP coherence analysis to demonstrate that high frequency stimulation of the STN modulates connectivity between RFA, CFA, and STN in the  $\beta$ - and high  $\gamma$ -frequency band. These results align with previous studies that have shown a decrease in coherence between cortical areas and the STN with high frequency stimulation (Li et al. 2007; Matsumoto et al. 2007; Gonzalez-Escamilla et al. 2022). I also employed tPDC analysis to estimate the direction and strength of effective connectivity between RFA, CFA, and STN. This approach adds additional value to coherence measurements by providing information on the directionality of information flows (Vergotte et al. 2017; Muthuraman M et al. 2018). My findings revealed that 160 Hz STN stimulation led to a significant reduction in information transmission from CFA L5 and L6 to RFA L6 and from RFA L6 to CFA L2/3. Additionally, there was a decrease in information transmission from STN towards RFA and CFA. However, the tPDC values for the direction of the cortical areas towards the STN remained unchanged (Figure 27), indicating an antidromic activation of the hyper-direct pathway leading to information transmission from the STN towards RFA and CFA. My results are layer-specific and therefore capture the specificity of cortico-cortical connections as well as subthalamo-pallido-thalamo-cortical connections. We see differential effects at the single layer level and not in all recorded sites, therefore minimizing the chance of corroborated activity.

My findings extend previous research (Schor et al. 2021), by demonstrating that subthalamic nucleus deep brain stimulation (STN DBS) leads to a specific and effective modification of motor programs, which supports the pacemaker function of the STN for motor function. As mentioned earlier, three major hypotheses have been proposed regarding how DBS affects motor symptoms (Chiken and Nambu 2014): The first hypothesis suggests that STN DBS silences STN activity by inhibiting it, which is consistent with the rate model. The second hypothesis, based on the observation that STN DBS can activate cortical neurons in an antidromic fashion, proposes that STN DBS bypasses the basal ganglia output and directly influences motor cortical activity. The third hypothesis suggests that STN DBS reduces symptoms by inducing plasticity in the STN, resulting in an adaptive response in connected areas. Although these hypotheses are not mutually exclusive, our results indicate that a combination of these theories can explain the motor outcomes I observed. Specifically, I found a significant reduction in STN activity across a broad frequency range (Figure 17). Furthermore, I demonstrated that high frequency STN stimulation had a significant effect on the activity and connectivity between the two motor cortical areas, RFA and CFA.

## 6 Conclusion and Outlook

While many studies have analysed the function and connectivity within the human premotor motor network (Johansen-Berg et al. 2004; Groppa and Schlaak et al. 2012), its homologue in the mouse has not been analysed in detail. However, mice are commonly used as model organisms to analyse the pathophysiology of various movement disorders, such as Parkinson's disease, and possible treatments (Mirzac et al. 2023). Therefore, a detailed understanding of the mouse motor cortex, its physiological neuronal activity and the connectivity between its different areas is crucial.

My findings emphasize the strong connection between the RFA and CFA in the mouse motor cortex, revealing a highly interconnected network. This highlights not only the intricate organization of the motor cortical circuitry but also the translational relevance of the mouse RFA-CFA network as a model for studying premotor-motor connectivity in humans. Furthermore, the observed similarities between the mouse RFA-CFA network and the human PMC-M1 network validate the utility of the mouse model in translational research, providing

a valuable platform for investigating the pathophysiology of movement disorders (Kreis et al. 2022).

In the second part of my thesis, I investigated the effect of STN stimulation on the RFA-CFA-STN network, which has yielded significant insights, albeit revealing a complex and multifaceted relationship. Although the precise mechanism of action of STN stimulation remains unclear, our findings suggest that high frequency stimulation exerts a pronounced modulatory effect on network dynamics. Notably, our results indicate that high stimulation frequencies, particularly 160 Hz, are most effective in inducing alterations within the motor cortex-STN network. However, it is crucial to note that even 50 Hz stimulation, traditionally viewed as less effective, elicits measurable effects, consistent with previous studies.

My research results indicate a substantial impact of high frequency stimulation in the RFA-CFA-STN motor network, particularly in the STN. Our findings confirm that high frequency stimulation of the STN reduces the number of long  $\beta$  bursts in RFA, CFA, and STN. Our analysis showed a significant decrease in coherence between RFA, CFA, and STN in the  $\beta$ - and high  $\gamma$ -frequency bands during 160 Hz STN stimulation. Furthermore, we demonstrated that the flow of information from the cortex towards STN is unchanged during high frequency stimulation, while the flow of information from STN towards RFA and CFA is significantly reduced. This is likely due to antidromic activation, which quickly spreads from L5 pyramidal neurons in the primary motor cortex to all cortical layers via intracortical microcircuits. Overall, our results suggest that high frequency stimulation of the STN may not silence STN activity but rather lead to a shift towards less burst-like activity.

This thesis constitutes a critical component in the ongoing endeavour to decipher the complexities of STN DBS and its influence on the motor cortex-STN network. Although our findings offer significant insights, additional research is necessary to fully comprehend the underlying mechanism of STN DBS.

In conclusion, this study enhances our comprehension of motor cortical circuitry and its modulation by STN stimulation. By elucidating the intricate interactions within the RFA-CFA-STN network, this research establishes a solid foundation for the development of tailored therapeutic interventions aimed at restoring motor function in individuals with movement disorders. Moving forward, collaborative efforts between basic science and clinical research will be crucial in advancing our knowledge and improving treatment outcomes in this field.



## 7 References

- Abreu R, Leal A, Figueiredo P. 2018. EEG-Informed fMRI: A Review of Data Analysis Methods. *Frontiers in human neuroscience*. 12:29. eng. doi:10.3389/fnhum.2018.00029.
- Achermann P, Borbély AA. 1997. Low-frequency (< 1 Hz) oscillations in the human sleep electroencephalogram. *Neuroscience*. 81(1):213–222. eng. doi:10.1016/s0306-4522(97)00186-3.
- Adelhöfer N, Beste C. 2020. Pre-trial theta band activity in the ventromedial prefrontal cortex correlates with inhibition-related theta band activity in the right inferior frontal cortex. *Neuroimage*. 219:117052. eng. doi:10.1016/j.neuroimage.2020.117052.
- ADRIAN ED. 1950. The electrical activity of the mammalian olfactory bulb. *Electroencephalogr Clin Neurophysiol*. 2(4):377–388. eng. doi:10.1016/0013-4694(50)90075-7.
- Aron AR, Herz DM, Brown P, Forstmann BU, Zaghoul K. 2016. Frontosubthalamic Circuits for Control of Action and Cognition. *J Neurosci*. 36(45):11489–11495. eng. doi:10.1523/JNEUROSCI.2348-16.2016.
- Assenza G, Di Lazzaro V. 2015. A useful electroencephalography (EEG) marker of brain plasticity: delta waves. *Neural Regen Res*. 10(8):1216–1217. eng. doi:10.4103/1673-5374.162698.
- Athanasiou A, Klados MA, Styliadis C, Foroglou N, Polyzoidis K, Bamidis PD. 2018. Investigating the Role of Alpha and Beta Rhythms in Functional Motor Networks. *Neuroscience*. 378:54–70. doi:10.1016/j.neuroscience.2016.05.044.
- Baker SN. 2007. Oscillatory interactions between sensorimotor cortex and the periphery. *Current Opinion in Neurobiology*. 17(6):649–655. eng. doi:10.1016/j.conb.2008.01.007.
- Baker SN, Olivier E, Lemon RN. 1997. Coherent oscillations in monkey motor cortex and hand muscle EMG show task-dependent modulation. *J Physiol*. 501 (Pt 1)(Pt 1):225–241. eng. doi:10.1111/j.1469-7793.1997.225bo.x.
- Bakken TE, Jorstad NL, Hu Q, Lake BB, Tian W, Kalmbach BE, Crow M, Hodge RD, Krienen FM, Sorensen SA, et al. 2021. Comparative cellular analysis of motor cortex in human, marmoset and mouse. *Nature*. 598(7879):111–119. eng. doi:10.1038/s41586-021-03465-8.

- Bange M, Gonzalez-Escamilla G, Herz DM, Tinkhauser G, Glaser M, Ciolac D, Pogosyan A, Kreis SL, Luhmann HJ, Tan H, et al. 2024. Subthalamic stimulation modulates context-dependent effects of beta bursts during fine motor control. *Nat Commun.* 15(1):3166. eng. doi:10.1038/s41467-024-47555-3.
- Barone J, Rossiter HE. 2021. Understanding the Role of Sensorimotor Beta Oscillations. *Front Syst Neurosci.* 15:655886. eng. doi:10.3389/fnsys.2021.655886.
- Barry RJ, Clarke AR, Johnstone SJ, Magee CA, Rushby JA. 2007. EEG differences between eyes-closed and eyes-open resting conditions. *Clinical neurophysiology: official journal of the International Federation of Clinical Neurophysiology.* 118(12):2765–2773. eng. doi:10.1016/j.clinph.2007.07.028.
- Başar E, Güntekin B. 2008. A review of brain oscillations in cognitive disorders and the role of neurotransmitters. *Brain Res.* 1235:172–193. eng. doi:10.1016/j.brainres.2008.06.103.
- Becker R, Vidaurre D, Quinn AJ, Abeyesuriya RG, Parker Jones O, Jbabdi S, Woolrich MW. 2020. Transient spectral events in resting state MEG predict individual task responses. *Neuroimage.* 215:116818. eng. doi:10.1016/j.neuroimage.2020.116818;
- Benazzouz A, Breit S, Koudsie A, Pollak P, Krack P, Benabid A-L. 2002. Intraoperative microrecordings of the subthalamic nucleus in Parkinson's disease. *Mov Disord.* 17 Suppl 3:S145-9. eng. doi:10.1002/mds.10156.
- Benazzouz A, Gao DM, Ni ZG, Piallat B, Bouali-Benazzouz R, Benabid AL. 2000. Effect of high-frequency stimulation of the subthalamic nucleus on the neuronal activities of the substantia nigra pars reticulata and ventrolateral nucleus of the thalamus in the rat. *Neuroscience.* 99(2):289–295. eng. doi:10.1016/S0306-4522(00)00199-8.
- Benazzouz A, Piallat B, Pollak P, Benabid AL. 1995. Responses of substantia nigra pars reticulata and globus pallidus complex to high frequency stimulation of the subthalamic nucleus in rats: electrophysiological data. *Neurosci Lett.* 189(2):77–80. eng. doi:10.1016/0304-3940(95)11455-6.
- Berger H. 1929. Über das Elektrenkephalogramm des Menschen. *Archiv f. Psychiatrie.* 87(1):527–570. doi:10.1007/BF01797193.
- Bloem BR, Okun MS, Klein C. 2021. Parkinson's disease. *The Lancet.* doi:10.1016/S0140-6736(21)00218-X.

- Boëx C, Awadhi AA, Tyrand R, Corniola MV, Kibleur A, Fleury V, Burkhard PR, Momjian S. 2023. Validation of Lead-DBS  $\beta$ -Oscillation Localization with Directional Electrodes. *Bioengineering (Basel)*. 10(8). eng. doi:10.3390/bioengineering10080898.
- Brocker DT, Swan BD, So RQ, Turner DA, Gross RE, Grill WM. 2017. Optimized temporal pattern of brain stimulation designed by computational evolution. *Sci Transl Med*. 9(371). eng. doi:10.1126/scitranslmed.aah3532.
- Brown AR, Mitra S, Teskey GC, Boychuk JA. 2023. Complex forelimb movements and cortical topography evoked by intracortical microstimulation in male and female mice. *Cereb Cortex*. 33(5):1866–1875. eng. doi:10.1093/cercor/bhac178.
- Brunet NM, Fries P. 2019. Human visual cortical gamma reflects natural image structure. *Neuroimage*. 200:635–643. eng. doi:10.1016/j.neuroimage.2019.06.051.
- Bukhari Q, Schroeter A, Rudin M. 2018. Increasing isoflurane dose reduces homotopic correlation and functional segregation of brain networks in mice as revealed by resting-state fMRI. *Sci Rep*. 8(1):10591. doi:10.1038/s41598-018-28766-3.
- Carmona LM, Thomas ED, Smith K, Tasic B, Costa RM, Nelson A. 2024. Topographical and cell type-specific connectivity of rostral and caudal forelimb corticospinal neuron populations. *Cell reports*. 43(4):113993. eng. doi:10.1016/j.celrep.2024.113993.
- Chaure FJ, Rey HG, Quian Quiroga R. 2018. A novel and fully automatic spike-sorting implementation with variable number of features. *J Neurophysiol*. 120(4):1859–1871. doi:10.1152/jn.00339.2018.
- Chiken S, Nambu A. 2014. Disrupting neuronal transmission: mechanism of DBS? *Front Syst Neurosci*. 8:33. eng. doi:10.3389/fnsys.2014.00033.
- Chouinard PA, Paus T. 2006. The primary motor and premotor areas of the human cerebral cortex. *The Neuroscientist: a review journal bringing neurobiology, neurology and psychiatry*. 12(2):143–152. doi:10.1177/1073858405284255.
- Cohen MX. 2014. A neural microcircuit for cognitive conflict detection and signaling. *Trends Neurosci*. 37(9):480–490. eng. doi:10.1016/j.tins.2014.06.004.
- Cowan RL, Wilson CJ. 1994. Spontaneous firing patterns and axonal projections of single corticostriatal neurons in the rat medial agranular cortex. *J Neurophysiol*. 71(1):17–32. eng. doi:10.1152/jn.1994.71.1.17.

- Dancause N, Barbay S, Frost SB, Plautz EJ, Popescu M, Dixon PM, Stowe AM, Friel KM, Nudo RJ. 2006. Topographically divergent and convergent connectivity between premotor and primary motor cortex. *Cereb Cortex*. 16(8):1057–1068. eng. doi:10.1093/cercor/bhj049.
- Das A, Holden S, Borovicka J, Icardi J, O'Neil A, Chaklai A, Patel D, Patel R, Kaech Petrie S, Raber J, et al. 2023. Large-scale recording of neuronal activity in freely-moving mice at cellular resolution. *Nat Commun*. 14(1):6399. eng. doi:10.1038/s41467-023-42083-y.
- Deffains M, Bergman H. 2019. Parkinsonism-related  $\beta$  oscillations in the primate basal ganglia networks - Recent advances and clinical implications. *Parkinsonism Relat Disord*. 59:2–8. eng. doi:10.1016/j.parkreldis.2018.12.015.
- Deffains M, Iskhakova L, Katabi S, Israel Z, Bergman H. 2018. Longer  $\beta$  oscillatory episodes reliably identify pathological subthalamic activity in Parkinsonism. *Mov Disord*. 33(10):1609–1618. eng. doi:10.1002/mds.27418.
- Deffeyes JE, Touvykine B, Quessy S, Dancause N. 2015. Interactions between rostral and caudal cortical motor areas in the rat. *J Neurophysiol*. 113(10):3893–3904. doi:10.1152/jn.00760.2014.
- Deuschl G, Paschen S, Witt K. 2013. Clinical outcome of deep brain stimulation for Parkinson's disease. *Handb Clin Neurol*. 116:107–128. eng. doi:10.1016/B978-0-444-53497-2.00010-3.
- Devonshire IM, Grandy TH, Dommett EJ, Greenfield SA. 2010. Effects of urethane anaesthesia on sensory processing in the rat barrel cortex revealed by combined optical imaging and electrophysiology. *Eur J Neurosci*. 32(5):786–797. eng. doi:10.1111/j.1460-9568.2010.07322.x.
- Dichter GS, Gibbs D, Smoski MJ. 2015. A systematic review of relations between resting-state functional-MRI and treatment response in major depressive disorder. *J Affect Disord*. 172:8–17. eng. doi:10.1016/j.jad.2014.09.028.
- Dijk DJ, Beersma DG, Daan S. 1987. EEG power density during nap sleep: reflection of an hourglass measuring the duration of prior wakefulness. *J Biol Rhythms*. 2(3):207–219. eng. doi:10.1177/074873048700200304.
- Dippel G, Mückschel M, Ziemssen T, Beste C. 2017. Demands on response inhibition processes determine modulations of theta band activity in superior frontal areas and correlations with pupillometry - Implications for the norepinephrine system during

- inhibitory control. *Neuroimage*. 157:575–585. eng.  
doi:10.1016/j.neuroimage.2017.06.037.
- Donoghue JP, Wise SP. 1982. The motor cortex of the rat: cytoarchitecture and microstimulation mapping. *The Journal of comparative neurology*. 212(1):76–88.  
doi:10.1002/cne.902120106.
- Dorval AD, Kuncel AM, Birdno MJ, Turner DA, Grill WM. 2010. Deep brain stimulation alleviates parkinsonian bradykinesia by regularizing pallidal activity. *J Neurophysiol*. 104(2):911–921. eng. doi:10.1152/jn.00103.2010.
- Duchet B, Ghezzi F, Weerasinghe G, Tinkhauser G, Kühn AA, Brown P, Bick C, Bogacz R. 2021. Average beta burst duration profiles provide a signature of dynamical changes between the ON and OFF medication states in Parkinson's disease. *PLoS Comput Biol*. 17(7):e1009116. eng. doi:10.1371/journal.pcbi.1009116.
- Ebbesen CL, Brecht M. 2017. Motor cortex - to act or not to act? *Nature reviews. Neuroscience*. 18(11):694–705. eng. doi:10.1038/nrn.2017.119.
- Eisner-Janowicz I, Barbay S, Hoover E, Stowe AM, Frost SB, Plautz EJ, Nudo RJ. 2008. Early and late changes in the distal forelimb representation of the supplementary motor area after injury to frontal motor areas in the squirrel monkey. *J Neurophysiol*. 100(3):1498–1512. eng. doi:10.1152/jn.90447.2008.
- Ekstrom AD, Caplan JB, Ho E, Shattuck K, Fried I, Kahana MJ. 2005. Human hippocampal theta activity during virtual navigation. *Hippocampus*. 15(7):881–889. eng.  
doi:10.1002/hipo.20109.
- Engel AK, Fries P. 2010. Beta-band oscillations-signalling the status quo? *Current Opinion in Neurobiology*. 20(2):156–165. doi:10.1016/j.conb.2010.02.015.
- Faull RL, Lavery R. 1969. Changes in dopamine levels in the corpus striatum following lesions in the substantia nigra. *Exp Neurol*. 23(3):332–340. eng. doi:10.1016/0014-4886(69)90081-8.
- Fernandez-Ruiz A, Sirota A, Lopes-Dos-Santos V, Dupret D. 2023. Over and above frequency: Gamma oscillations as units of neural circuit operations. *Neuron*. 111(7):936–953. eng.  
doi:10.1016/j.neuron.2023.02.026.
- Fitzgerald PJ, Watson BO. 2018. Gamma oscillations as a biomarker for major depression: an emerging topic. *Transl Psychiatry*. 8(1):177. eng. doi:10.1038/s41398-018-0239-y.

- Fogelson N, Williams D, Tijssen M, van Bruggen G, Speelman H, Brown P. 2006. Different functional loops between cerebral cortex and the subthalamic area in Parkinson's disease. *Cereb Cortex*. 16(1):64–75. eng. doi:10.1093/cercor/bhi084.
- Foster NN, Barry J, Korobkova L, Garcia L, Gao L, Becerra M, Sherafat Y, Peng B, Li X, Choi J-H, et al. 2021. The mouse cortico-basal ganglia-thalamic network. *Nature*. 598(7879):188–194. eng. doi:10.1038/s41586-021-03993-3.
- Franken P, Tobler I, Borbély AA. 1991. Sleep homeostasis in the rat: simulation of the time course of EEG slow-wave activity. *Neurosci Lett*. 130(2):141–144. eng. doi:10.1016/0304-3940(91)90382-4.
- Galati S, Mazzone P, Fedele E, Pisani A, Peppe A, Pierantozzi M, Brusa L, Tropepi D, Moschella V, Raiteri M, et al. 2006. Biochemical and electrophysiological changes of substantia nigra pars reticulata driven by subthalamic stimulation in patients with Parkinson's disease. *Eur J Neurosci*. 23(11):2923–2928. eng. doi:10.1111/j.1460-9568.2006.04816.x.
- Giordano N, Alia C, Fruzzetti L, Pasquini M, Palla G, Mazzoni A, Micera S, Fogassi L, Bonini L, Caleo M. 2023. Fast-Spiking Interneurons of the Premotor Cortex Contribute to Initiation and Execution of Spontaneous Actions. *J Neurosci*. 43(23):4234–4250. eng. doi:10.1523/JNEUROSCI.0750-22.2023.
- Gonzalez-Escamilla G, Koirala N, Bange M, Glaser M, Pintea B, Dresel C, Deuschl G, Muthuraman M, Groppa S. 2022. Deciphering the Network Effects of Deep Brain Stimulation in Parkinson's Disease. *Neurol Ther*. 11(1):265–282. eng. doi:10.1007/s40120-021-00318-4.
- Gradinaru V, Mogri M, Thompson KR, Henderson JM, Deisseroth K. 2009. Optical Deconstruction of Parkinsonian Neural Circuitry. *Science*. 324(5925):354–359. eng. doi:10.1126/science.1167093.
- Grandi LC, Kaelin-Lang A, Orban G, Song W, Salvadè A, Stefani A, Di Giovanni G, Galati S. 2018. Oscillatory Activity in the Cortex, Motor Thalamus and Nucleus Reticularis Thalami in Acute TTX and Chronic 6-OHDA Dopamine-Depleted Animals. *Front Neurol*. 9:663. eng. doi:10.3389/fneur.2018.00663.

- Gray CM, König P, Engel AK, Singer W. 1989. Oscillatory responses in cat visual cortex exhibit inter-columnar synchronization which reflects global stimulus properties. *Nature*. 338(6213):334–337. eng. doi:10.1038/338334a0.
- Graziano MSA, Taylor CSR, Moore T. 2002. Complex movements evoked by microstimulation of precentral cortex. *Neuron*. 34(5):841–851. eng. doi:10.1016/S0896-6273(02)00698-0.
- Groenewegen HJ. 2003. The basal ganglia and motor control. *Neural Plast*. 10(1-2):107–120. eng. doi:10.1155/NP.2003.107.
- Groppa S, Schlaak BH, Münchau A, Werner-Petroll N, Dünneberger J, Bäumer T, van Nuenen BFL, Siebner HR. 2012. The human dorsal premotor cortex facilitates the excitability of ipsilateral primary motor cortex via a short latency cortico-cortical route. *Human brain mapping*. 33(2):419–430. doi:10.1002/hbm.21221.
- Groppa S, Werner-Petroll N, Münchau A, Deuschl G, Ruschworth MFS, Siebner HR. 2012. A novel dual-site transcranial magnetic stimulation paradigm to probe fast facilitatory inputs from ipsilateral dorsal premotor cortex to primary motor cortex. *Neuroimage*. 62(1):500–509. doi:10.1016/j.neuroimage.2012.05.023.
- Güntekin B, Başar E. 2016. Review of evoked and event-related delta responses in the human brain. *Int J Psychophysiol*. 103:43–52. eng. doi:10.1016/j.ijpsycho.2015.02.001.
- Haber SN. 2017. Anatomy and Connectivity of the Reward Circuit. In: *Decision Neuroscience*. [place unknown]: Elsevier. p. 3–19.
- Hara K, Harris RA. 2002. The Anesthetic Mechanism of Urethane: The Effects on Neurotransmitter-Gated Ion Channels. *Anesthesia & Analgesia*. 94(2):313–318. doi:10.1213/00000539-200202000-00015.
- Harrison TC, Ayling OGS, Murphy TH. 2012. Distinct cortical circuit mechanisms for complex forelimb movement and motor map topography. *Neuron*. 74(2):397–409. doi:10.1016/j.neuron.2012.02.028.
- Hashimoto T, Elder CM, Okun MS, Patrick SK, Vitek JL. 2003. Stimulation of the subthalamic nucleus changes the firing pattern of pallidal neurons. *J Neurosci*. 23(5):1916–1923. eng. doi:10.1523/JNEUROSCI.23-05-01916.2003.
- Haufe S, Nikulin VV, Müller K-R, Nolte G. 2013. A critical assessment of connectivity measures for EEG data: a simulation study. *Neuroimage*. 64:120–133. eng. doi:10.1016/j.neuroimage.2012.09.036.

- He S, Baig F, Merla A, Torrecillos F, Perera A, Wiest C, Debarros J, Benjaber M, Hart MG, Ricciardi L, et al. 2023. Beta-triggered adaptive deep brain stimulation during reaching movement in Parkinson's disease. *Brain*. 146(12):5015–5030. eng. doi:10.1093/brain/awad233.
- Héricé C, Khalil R, Moftah M, Boraud T, Guthrie M, Garenne A. 2016. Decision making under uncertainty in a spiking neural network model of the basal ganglia. *J Integr Neurosci*. 15(4):515–538. eng. doi:10.1142/S021963521650028X.
- Herz DM, Bange M, Gonzalez-Escamilla G, Auer M, Ashkan K, Fischer P, Tan H, Bogacz R, Muthuraman M, Groppa S, et al. 2022. Dynamic control of decision and movement speed in the human basal ganglia. *Nat Commun*. 13(1):7530. eng. doi:10.1038/s41467-022-35121-8.
- Hira R, Ohkubo F, Tanaka YR, Masamizu Y, Augustine GJ, Kasai H, Matsuzaki M. 2013. In vivo optogenetic tracing of functional corticocortical connections between motor forelimb areas. *Frontiers in neural circuits*. 7:55. doi:10.3389/fncir.2013.00055.
- Hira R, Terada S-I, Kondo M, Matsuzaki M. 2015. Distinct Functional Modules for Discrete and Rhythmic Forelimb Movements in the Mouse Motor Cortex. *J Neurosci*. 35(39):13311–13322. doi:10.1523/JNEUROSCI.2731-15.2015.
- Hu K, Jamali M, Moses ZB, Ortega CA, Friedman GN, Xu W, Williams ZM. 2018. Decoding unconstrained arm movements in primates using high-density electrocorticography signals for brain-machine interface use. *Sci Rep*. 8(1):10583. eng. doi:10.1038/s41598-018-28940-7.
- Hubbard J, Gent TC, Hoekstra MMB, Emmenegger Y, Mongrain V, Landolt H-P, Adamantidis AR, Franken P. 2020. Rapid fast-delta decay following prolonged wakefulness marks a phase of wake-inertia in NREM sleep. *Nat Commun*. 11(1):3130. eng. doi:10.1038/s41467-020-16915-0.
- Iderberg H, Francardo V, Pioli EY. 2012. Animal models of L-DOPA-induced dyskinesia: an update on the current options. *Neuroscience*. 211:13–27. doi:10.1016/j.neuroscience.2012.03.023.
- Jackson A, Spinks RL, Freeman TCB, Wolpert DM, Lemon RN. 2002. Rhythm generation in monkey motor cortex explored using pyramidal tract stimulation. *J Physiol*. 541(Pt 3):685–699. eng. doi:10.1113/jphysiol.2001.015099.

- Jahangiri A, Sepulveda F. 2018. The Relative Contribution of High-Gamma Linguistic Processing Stages of Word Production, and Motor Imagery of Articulation in Class Separability of Covert Speech Tasks in EEG Data. *J Med Syst.* 43(2):20. eng. doi:10.1007/s10916-018-1137-9.
- Jahanshahi M, Obeso I, Baunez C, Alegre M, Krack P. 2015. Parkinson's disease, the subthalamic nucleus, inhibition, and impulsivity. *Mov Disord.* 30(2):128–140. eng. doi:10.1002/mds.26049.
- Jana S, Hannah R, Muralidharan V, Aron AR. 2020. Temporal cascade of frontal, motor and muscle processes underlying human action-stopping. *Elife.* 9. eng. doi:10.7554/eLife.50371.
- Jenkinson N, Kühn AA, Brown P. 2013.  $\gamma$  oscillations in the human basal ganglia. *Exp Neurol.* 245:72–76. eng. doi:10.1016/j.expneurol.2012.07.005.
- Johansen-Berg H, Behrens TEJ, Robson MD, Drobnjak I, Rushworth MFS, Brady JM, Smith SM, Higham DJ, Matthews PM. 2004. Changes in connectivity profiles define functionally distinct regions in human medial frontal cortex. *Proceedings of the National Academy of Sciences of the United States of America.* 101(36):13335–13340. doi:10.1073/pnas.0403743101.
- Johnson LA, Wang J, Nebeck SD, Zhang J, Johnson MD, Vitek JL. 2020. Direct Activation of Primary Motor Cortex during Subthalamic But Not Pallidal Deep Brain Stimulation. *J Neurosci.* 40(10):2166–2177. eng. doi:10.1523/JNEUROSCI.2480-19.2020.
- Karakaş S. 2020. A review of theta oscillation and its functional correlates. *Int J Psychophysiol.* 157:82–99. eng. doi:10.1016/j.ijpsycho.2020.04.008.
- Khanna P, Carmena JM. 2015. Neural oscillations: beta band activity across motor networks. *Current Opinion in Neurobiology.* 32:60–67. eng. doi:10.1016/j.conb.2014.11.010.
- Khawaldeh S, Tinkhauser G, Torrecillos F, He S, Foltynie T, Limousin P, Zrinzo L, Oswal A, Quinn AJ, Vidaurre D, et al. 2022. Balance between competing spectral states in subthalamic nucleus is linked to motor impairment in Parkinson's disease. *Brain.* 145(1):237–250. eng. doi:10.1093/brain/awab264.
- Kilavik BE, Zaepffel M, Brovelli A, MacKay WA, Riehle A. 2013. The ups and downs of  $\beta$  oscillations in sensorimotor cortex. *Exp Neurol.* 245:15–26. eng. doi:10.1016/j.expneurol.2012.09.014.

- Klimesch W. 2012.  $\alpha$ -band oscillations, attention, and controlled access to stored information. *Trends Cogn Sci.* 16(12):606–617. eng. doi:10.1016/j.tics.2012.10.007.
- Knorr S, Musacchio T, Paulat R, Matthies C, Endres H, Wenger N, Harms C, Ip CW. 2022. Experimental deep brain stimulation in rodent models of movement disorders. *Exp Neurol.* 348:113926. eng. doi:10.1016/j.expneurol.2021.113926.
- Knyazev GG. 2007. Motivation, emotion, and their inhibitory control mirrored in brain oscillations. *Neurosci Biobehav Rev.* 31(3):377–395. eng. doi:10.1016/j.neubiorev.2006.10.004.
- Kreis SL, Luhmann HJ, Ciolac D, Groppa S, Muthuraman M. 2022. Translational Model of Cortical Premotor-Motor Networks. *Cereb Cortex.* 32(12):2621–2634. eng. doi:10.1093/cercor/bhab369.
- Kühn AA, Kempf F, Brücke C, Gaynor Doyle L, Martinez-Torres I, Pogosyan A, Trottenberg T, Kupsch A, Schneider G-H, Hariz MI, et al. 2008. High-frequency stimulation of the subthalamic nucleus suppresses oscillatory beta activity in patients with Parkinson's disease in parallel with improvement in motor performance. *J Neurosci.* 28(24):6165–6173. eng. doi:10.1523/JNEUROSCI.0282-08.2008.
- Kühn AA, Tsui A, Aziz T, Ray N, Brücke C, Kupsch A, Schneider G-H, Brown P. 2009. Pathological synchronisation in the subthalamic nucleus of patients with Parkinson's disease relates to both bradykinesia and rigidity. *Exp Neurol.* 215(2):380–387. eng. doi:10.1016/j.expneurol.2008.11.008.
- Lai H-J, Deng C-R, Wang R-W, Lee L-HN, Kuo C-C. 2022. The genesis and functional consequences of cortico-subthalamic beta augmentation and excessive subthalamic burst discharges after dopaminergic deprivation. *Exp Neurol.* 356:114153. eng. doi:10.1016/j.expneurol.2022.114153.
- Lansbergen MM, Schutter DJLG, Kenemans JL. 2007. Subjective impulsivity and baseline EEG in relation to stopping performance. *Brain Res.* 1148:161–169. eng. doi:10.1016/j.brainres.2007.02.034.
- Lee C, Kim Y, Kaang B-K. 2022. The Primary Motor Cortex: The Hub of Motor Learning in Rodents. *Neuroscience.* 485:163–170. eng. doi:10.1016/j.neuroscience.2022.01.009.

- Leviashvili S, Ezra Y, Droby A, Ding H, Groppa S, Mirelman A, Muthuraman M, Maidan I. 2022. EEG-Based Mapping of Resting-State Functional Brain Networks in Patients with Parkinson's Disease. *Biomimetics*. 7(4):231. eng. doi:10.3390/biomimetics7040231.
- Li Q, Ke Y, Chan DCW, Qian Z-M, Yung KKL, Ko H, Arbuthnott GW, Yung W-H. 2012. Therapeutic deep brain stimulation in Parkinsonian rats directly influences motor cortex. *Neuron*. 76(5):1030–1041. eng. doi:10.1016/j.neuron.2012.09.032.
- Li S, Arbuthnott GW, Jutras MJ, Goldberg JA, Jaeger D. 2007. Resonant antidromic cortical circuit activation as a consequence of high-frequency subthalamic deep-brain stimulation. *J Neurophysiol*. 98(6):3525–3537. eng. doi:10.1152/jn.00808.2007.
- Litvak V, Eusebio A, Jha A, Oostenveld R, Barnes G, Foltynie T, Limousin P, Zrinzo L, Hariz MI, Friston K, et al. 2012. Movement-related changes in local and long-range synchronization in Parkinson's disease revealed by simultaneous magnetoencephalography and intracranial recordings. *J Neurosci*. 32(31):10541–10553. eng. doi:10.1523/JNEUROSCI.0767-12.2012.
- Liu Y, Nour MM, Schuck NW, Behrens TEJ, Dolan RJ. 2022. Decoding cognition from spontaneous neural activity. *Nature reviews. Neuroscience*. 23(4):204–214. eng. doi:10.1038/s41583-022-00570-z.
- Llinás RR. 1988. The intrinsic electrophysiological properties of mammalian neurons: insights into central nervous system function. *Science*. 242(4886):1654–1664. eng. doi:10.1126/science.3059497.
- Lozano AM, Lipsman N. 2013. Probing and regulating dysfunctional circuits using deep brain stimulation. *Neuron*. 77(3):406–424. eng. doi:10.1016/j.neuron.2013.01.020.
- Lozano AM, Lipsman N, Bergman H, Brown P, Chabardes S, Chang JW, Matthews K, McIntyre CC, Schlaepfer TE, Schulder M, et al. 2019. Deep brain stimulation: current challenges and future directions. *Nat Rev Neurol*. 15(3):148–160. eng. doi:10.1038/s41582-018-0128-2.
- Lundqvist M, Rose J, Herman P, Brincat SL, Buschman TJ, Miller EK. 2016. Gamma and Beta Bursts Underlie Working Memory. *Neuron*. 90(1):152–164. eng. doi:10.1016/j.neuron.2016.02.028.

- Maggi CA, Meli A. 1986. Suitability of urethane anesthesia for physiopharmacological investigations in various systems. Part 1: General considerations. *Experientia*. 42(2):109–114. eng. doi:10.1007/BF01952426.
- Maik Stüttgen. 2020. MLIB - toolbox for analyzing spike data: MATLAB Central File Exchange. [place unknown]: [publisher unknown].  
(<https://www.mathworks.com/matlabcentral/fileexchange/37339-mlib-toolbox-for-analyzing-spike-data>),
- Mann EO, Radcliffe CA, Paulsen O. 2005. Hippocampal gamma-frequency oscillations: from interneurons to pyramidal cells, and back. *J Physiol*. 562(Pt 1):55–63. eng. doi:10.1113/jphysiol.2004.078758.
- Masamoto K, Kanno I. 2012. Anesthesia and the quantitative evaluation of neurovascular coupling. *J Cereb Blood Flow Metab*. 32(7):1233–1247. eng. doi:10.1038/jcbfm.2012.50.
- Matsumoto R, Nair DR, LaPresto E, Bingaman W, Shibasaki H, Lüders HO. 2007. Functional connectivity in human cortical motor system: a cortico-cortical evoked potential study. *Brain*. 130(Pt 1):181–197. doi:10.1093/brain/awl257.
- McVoy M, Lytle S, Fulchiero E, Aebi ME, Adeleye O, Sajatovic M. 2019. A systematic review of quantitative EEG as a possible biomarker in child psychiatric disorders. *Psychiatry Res*. 279:331–344. eng. doi:10.1016/j.psychres.2019.07.004.
- Miller KJ, Leuthardt EC, Schalk G, Rao RPN, Anderson NR, Moran DW, Miller JW, Ojemann JG. 2007. Spectral changes in cortical surface potentials during motor movement. *J Neurosci*. 27(9):2424–2432. eng. doi:10.1523/JNEUROSCI.3886-06.2007.
- Mirzac D, Kreis SL, Luhmann HJ, Gonzalez-Escamilla G, Groppa S. 2023. Translating Pathological Brain Activity Primers in Parkinson's Disease Research. *Research (Wash D C)*. 6:183. eng. doi:10.34133/research.0183.
- Mirzaei A, Kumar A, Leventhal D, Mallet N, Aertsen A, Berke J, Schmidt R. 2017. Sensorimotor Processing in the Basal Ganglia Leads to Transient Beta Oscillations during Behavior. *J Neurosci*. 37(46):11220–11232. eng. doi:10.1523/JNEUROSCI.1289-17.2017.
- Mohammed H, Jain N. 2014. Two whisker motor areas in the rat cortex: evidence from thalamocortical connections. *The Journal of comparative neurology*. 522(3):528–545. eng. doi:10.1002/cne.23424.

- Moran A, Stein E, Tischler H, Bebelovsky K, Bar-Gad I. 2011. Dynamic stereotypic responses of Basal Ganglia neurons to subthalamic nucleus high-frequency stimulation in the parkinsonian primate. *Front Syst Neurosci.* 5:21. eng. doi:10.3389/fnsys.2011.00021.
- Morin N, Jourdain VA, Di Paolo T. 2014. Modeling dyskinesia in animal models of Parkinson disease. *Exp Neurol.* 256:105–116. doi:10.1016/j.expneurol.2013.01.024.
- Münchau A, Bloem BR, Irlbacher K, Trimble MR, Rothwell JC. 2002. Functional Connectivity of Human Premotor and Motor Cortex Explored with Repetitive Transcranial Magnetic Stimulation. *The Journal of Neuroscience.* 22(2):554–561. doi:10.1523/JNEUROSCI.22-02-00554.2002.
- Muthukumaraswamy SD. 2010. Functional properties of human primary motor cortex gamma oscillations. *J Neurophysiol.* 104(5):2873–2885. eng. doi:10.1152/jn.00607.2010.
- Muthuraman M, Bange M, Koirala N, Ciolac D, Pintea B, Glaser M, Tinkhauser G, Brown P, Deuschl G, Groppa S. 2020. Cross-frequency coupling between gamma oscillations and deep brain stimulation frequency in Parkinson's disease. *Brain.* 143(11):3393–3407. eng. doi:10.1093/brain/awaa297.
- Muthuraman M, Deuschl G, Anwar AR, Mideksa KG, Helmolt F von, Schneider SA. 2015. Essential and aging-related tremor: Differences of central control. *Mov Disord.* 30(12):1673–1680. doi:10.1002/mds.26410.
- Muthuraman M, Heute U, Arning K, Anwar AR, Elble R, Deuschl G, Raethjen J. 2012. Oscillating central motor networks in pathological tremors and voluntary movements. What makes the difference? *Neuroimage.* 60(2):1331–1339. doi:10.1016/j.neuroimage.2012.01.088.
- Muthuraman M, Koirala N, Ciolac D, Pintea B, Glaser M, Groppa S, Tamás G, Groppa S. 2018. Deep Brain Stimulation and L-DOPA Therapy: Concepts of Action and Clinical Applications in Parkinson's Disease. *Front Neurol.* 9:711. eng. doi:10.3389/fneur.2018.00711.
- Muthuraman M, Palotai M, Jávör-Duray B, Kelemen A, Koirala N, Halász L, Erőss L, Fekete G, Bognár L, Deuschl G, et al. 2021. Frequency-specific network activity predicts bradykinesia severity in Parkinson's disease. *Neuroimage Clin.* 32:102857. eng. doi:10.1016/j.nicl.2021.102857.

- Muthuraman M, Raethjen J, Koirala N, Anwar AR, Mideksa KG, Elble R, Groppa S, Deuschl G. 2018. Cerebello-cortical network fingerprints differ between essential, Parkinson's and mimicked tremors. *Brain*. 141(6):1770–1781. doi:10.1093/brain/awy098.
- Neafsey EJ, Sievert C. 1982. A second forelimb motor area exists in rat frontal cortex. *Brain Res*. 232(1):151–156. doi:10.1016/0006-8993(82)90617-5.
- Ni ZG, Bouali-Benazzouz R, Gao DM, Benabid AL, Benazzouz A. 2001. Time-course of changes in firing rates and firing patterns of subthalamic nucleus neuronal activity after 6-OHDA-induced dopamine depletion in rats. *Brain Res*. 899(1-2):142–147. eng. doi:10.1016/s0006-8993(01)02219-3.
- Nowak M, Zich C, Stagg CJ. 2018. Motor Cortical Gamma Oscillations: What Have We Learnt and Where Are We Headed? *Curr Behav Neurosci Rep*. 5(2):136–142. eng. doi:10.1007/s40473-018-0151-z.
- Nudo RJ, McNeal D. 2013. Plasticity of cerebral functions. *Handb Clin Neurol*. 110:13–21. eng. doi:10.1016/B978-0-444-52901-5.00002-2.
- Okun MS, Vitek JL. 2004. Lesion therapy for Parkinson's disease and other movement disorders: update and controversies. *Mov Disord*. 19(4):375–389. eng. doi:10.1002/mds.20037.
- Olaru M, Cernera S, Hahn A, Wozny TA, Anso J, Hemptinne C de, Little S, Neumann W-J, Abbasi-Asl R, Starr PA. 2024. Motor network gamma oscillations in chronic home recordings predict dyskinesia in Parkinson's disease. *Brain*. 147(6):2038–2052. eng. doi:10.1093/brain/awae004.
- Oostenveld R, Fries P, Maris E, Schoffelen J-M. 2011. FieldTrip: Open source software for advanced analysis of MEG, EEG, and invasive electrophysiological data. *Comput Intell Neurosci*. 2011:156869. doi:10.1155/2011/156869.
- Ostrowski J, Rose M. 2024. Increases in pre-stimulus theta and alpha oscillations precede successful encoding of crossmodal associations. *Sci Rep*. 14(1):7895. eng. doi:10.1038/s41598-024-58227-z.
- Oswal A, Brown P, Litvak V. 2013. Synchronized neural oscillations and the pathophysiology of Parkinson's disease. *Curr Opin Neurol*. 26(6):662–670. eng. doi:10.1097/WCO.0000000000000034.

- Oswal A, Cao C, Yeh C-H, Neumann W-J, Gratwicke J, Akram H, Horn A, Li D, Zhan S, Zhang C, et al. 2021. Neural signatures of hyperdirect pathway activity in Parkinson's disease. *Nat Commun.* 12(1):5185. eng. doi:10.1038/s41467-021-25366-0.
- Paasonen J, Stenroos P, Salo RA, Kiviniemi V, Gröhn O. 2018. Functional connectivity under six anesthesia protocols and the awake condition in rat brain. *Neuroimage.* 172:9–20. eng. doi:10.1016/j.neuroimage.2018.01.014.
- Palva S, Palva JM. 2007. New vistas for alpha-frequency band oscillations. *Trends Neurosci.* 30(4):150–158. eng. doi:10.1016/j.tins.2007.02.001.
- Paxinos G, Franklin KBJ. 2019. Paxinos and Franklin's The mouse brain in stereotaxic coordinates. Fifth edition. London, San Diego, Cambridge, MA, Kidlington, Oxford: Elsevier Academic Press. XXVII Seiten, 326 ungezählte Seiten. ISBN: 9780128161579. eng.
- Penttonen M, Buzsáki G. 2003. Natural logarithmic relationship between brain oscillators. *THL.* 2(02):145. doi:10.1017/S1472928803000074.
- Pevzner A, Izadi A, Lee DJ, Shahlaie K, Gurkoff GG. 2016. Making Waves in the Brain: What Are Oscillations, and Why Modulating Them Makes Sense for Brain Injury. *Front Syst Neurosci.* 10:30. eng. doi:10.3389/fnsys.2016.00030.
- Pfurtscheller G, Da Lopes Silva FH. 1999. Event-related EEG/MEG synchronization and desynchronization: basic principles. *Clinical neurophysiology: official journal of the International Federation of Clinical Neurophysiology.* 110(11):1842–1857. eng. doi:10.1016/s1388-2457(99)00141-8.
- Powanwe AS, Longtin A. 2019. Determinants of Brain Rhythm Burst Statistics. *Sci Rep.* 9(1):18335. eng. doi:10.1038/s41598-019-54444-z.
- Pscherer C, Mückschel M, Summerer L, Bluschke A, Beste C. 2019. On the relevance of EEG resting theta activity for the neurophysiological dynamics underlying motor inhibitory control. *Human brain mapping.* 40(14):4253–4265. eng. doi:10.1002/hbm.24699.
- Purves D, editor. 2001. *Neuroscience.* 2. ed. Sunderland, Mass.: Sinauer. ISBN: 0-87893-742-0.
- Quiroga RQ, Nadasdy Z, Ben-Shaul Y. 2004. Unsupervised spike detection and sorting with wavelets and superparamagnetic clustering. *Neural computation.* 16(8):1661–1687. doi:10.1162/089976604774201631.

- Rad JS, Zhang Y, Aghazadeh F, Chen ZC. 2014. A study on tool wear monitoring using time-frequency transformation techniques. In: Proceedings of the 2014 International Conference on Innovative Design and Manufacturing (ICIDM). 2014 International Conference on Innovative Design and Manufacturing (ICIDM); 13.08.2014 - 15.08.2014; Montreal, QC, Canada. [place unknown]: IEEE. p. 342–347.
- Reis C, Sharott A, Magill PJ, van Wijk BCM, Parr T, Zeidman P, Friston KJ, Cagnan H. 2019. Thalamocortical dynamics underlying spontaneous transitions in beta power in Parkinsonism. *Neuroimage*. 193:103–114. eng. doi:10.1016/j.neuroimage.2019.03.009.
- Ringach DL. 2009. Spontaneous and driven cortical activity: implications for computation. *Current Opinion in Neurobiology*. 19(4):439–444. eng. doi:10.1016/j.conb.2009.07.005.
- Rouiller EM, Moret V, Liang F. 1993. Comparison of the connectional properties of the two forelimb areas of the rat sensorimotor cortex: support for the presence of a premotor or supplementary motor cortical area. *Somatosensory & motor research*. 10(3):269–289. doi:10.3109/08990229309028837.
- Salari N, Büchel C, Rose M. 2012. Functional dissociation of ongoing oscillatory brain states. *PloS one*. 7(5):e38090. eng. doi:10.1371/JOURNAL.PONE.0038090.
- Salvadè A, D'Angelo V, Di Giovanni G, Tinkhauser G, Sancesario G, Städler C, Möller JC, Stefani A, Kaelin-Lang A, Galati S. 2016. Distinct roles of cortical and pallidal  $\beta$  and  $\gamma$  frequencies in hemiparkinsonian and dyskinetic rats. *Exp Neurol*. 275 Pt 1:199–208. eng. doi:10.1016/j.expneurol.2015.11.005.
- Sceniak MP, Maciver MB. 2006. Cellular actions of urethane on rat visual cortical neurons in vitro. *J Neurophysiol*. 95(6):3865–3874. doi:10.1152/jn.01196.2005.
- Schiller B, Gianotti LRR, Nash K, Knoch D. 2014. Individual differences in inhibitory control--relationship between baseline activation in lateral PFC and an electrophysiological index of response inhibition. *Cereb Cortex*. 24(9):2430–2435. eng. doi:10.1093/cercor/bht095.
- Schor JS, Gonzalez Montalvo I, Spratt PWE, Brakaj RJ, Stansil JA, Twedell EL, Bender KJ, Nelson AB. 2022. Therapeutic deep brain stimulation disrupts movement-related subthalamic nucleus activity in parkinsonian mice. *Elife*. 11. eng. doi:10.7554/eLife.75253.

- Schor JS, Montalvo IG, Spratt PWE, Brakaj RJ, Stansil JA, Bender KJ, Nelson AB. 2021. Therapeutic Deep Brain Stimulation Disrupts Subthalamic Nucleus Activity Dynamics in Parkinsonian Mice. [place unknown]: [publisher unknown].
- Schor JS, Nelson AB. 2019. Multiple stimulation parameters influence efficacy of deep brain stimulation in parkinsonian mice. *J Clin Invest.* 129(9):3833–3838. eng. doi:10.1172/JCI122390.
- Sharott A, Magill PJ, Harnack D, Kupsch A, Meissner W, Brown P. 2005. Dopamine depletion increases the power and coherence of beta-oscillations in the cerebral cortex and subthalamic nucleus of the awake rat. *Eur J Neurosci.* 21(5):1413–1422. eng. doi:10.1111/j.1460-9568.2005.03973.x.
- Sherman MA, Lee S, Law R, Haegens S, Thorn CA, Hämäläinen MS, Moore CI, Jones SR. 2016. Neural mechanisms of transient neocortical beta rhythms: Converging evidence from humans, computational modeling, monkeys, and mice. *Proceedings of the National Academy of Sciences of the United States of America.* 113(33):E4885-94. eng. doi:10.1073/pnas.1604135113.
- Shin H, Law R, Tsutsui S, Moore CI, Jones SR. 2017. The rate of transient beta frequency events predicts behavior across tasks and species. *Elife.* 6. eng. doi:10.7554/eLife.29086.
- Shin U, Ding C, Woods V, Widge AS, Shoaran M. 2023. A 16-Channel Low-Power Neural Connectivity Extraction and Phase-Locked Deep Brain Stimulation SoC. *IEEE Solid State Circuits Lett.* 6:21–24. eng. doi:10.1109/lssc.2023.3238797.
- Smith MM, Weaver KE, Grabowski TJ, Rao RPN, Darvas F. 2014. Non-invasive detection of high gamma band activity during motor imagery. *Frontiers in human neuroscience.* 8:817. eng. doi:10.3389/fnhum.2014.00817.
- Soma LR. 1983. Anesthetic and analgesic considerations in the experimental animal. *Ann N Y Acad Sci.* 406:32–47. eng. doi:10.1111/j.1749-6632.1983.tb53483.x.
- Spinks RL, Kraskov A, Brochier T, Umiltà MA, Lemon RN. 2008. Selectivity for grasp in local field potential and single neuron activity recorded simultaneously from M1 and F5 in the awake macaque monkey. *J Neurosci.* 28(43):10961–10971. eng. doi:10.1523/JNEUROSCI.1956-08.2008.
- Tennant KA, Adkins DL, Donlan NA, Asay AL, Thomas N, Kleim JA, Jones TA. 2011. The organization of the forelimb representation of the C57BL/6 mouse motor cortex as

- defined by intracortical microstimulation and cytoarchitecture. *Cereb Cortex*. 21(4):865–876. eng. doi:10.1093/cercor/bhq159.
- Thürer B, Stockinger C, Focke A, Putze F, Schultz T, Stein T. 2016. Increased gamma band power during movement planning coincides with motor memory retrieval. *Neuroimage*. 125:172–181. eng. doi:10.1016/j.neuroimage.2015.10.008.
- Tinkhauser G, Pogosyan A, Tan H, Herz DM, Kühn AA, Brown P. 2017. Beta burst dynamics in Parkinson's disease OFF and ON dopaminergic medication. *Brain*. 140(11):2968–2981. doi:10.1093/brain/awx252.
- Tisch S, Silberstein P, Limousin-Dowsey P, Jahanshahi M. 2004. The basal ganglia: anatomy, physiology, and pharmacology. *Psychiatr Clin North Am*. 27(4):757–799. eng. doi:10.1016/j.psc.2004.06.004.
- Toro C, Deuschl G, Thatcher R, Sato S, Kufta C, Hallett M. 1994. Event-related desynchronization and movement-related cortical potentials on the ECoG and EEG. *Electroencephalogr Clin Neurophysiol*. 93(5):380–389. eng. doi:10.1016/0168-5597(94)90126-0.
- Torrecillos F, Tinkhauser G, Fischer P, Green AL, Aziz TZ, Foltynie T, Limousin P, Zrinzo L, Ashkan K, Brown P, et al. 2018. Modulation of Beta Bursts in the Subthalamic Nucleus Predicts Motor Performance. *J Neurosci*. 38(41):8905–8917. eng. doi:10.1523/JNEUROSCI.1314-18.2018.
- Uddin LQ. 2020. Bring the noise: Reconceptualizing spontaneous neural activity. *Trends Cogn Sci*. 24(9):734–746. eng. doi:10.1016/j.tics.2020.06.003.
- Urban Iii ET, Hudson HM, Li Y, Nishibe M, Barbay S, Guggenmos DJ, Nudo RJ. 2024. Corticocortical connections of the rostral forelimb area in rats: a quantitative tract-tracing study. *Cereb Cortex*. 34(2). eng. doi:10.1093/cercor/bhad530.
- Vergotte G, Torre K, Chirumamilla VC, Anwar AR, Groppa S, Perrey S, Muthuraman M. 2017. Dynamics of the human brain network revealed by time-frequency effective connectivity in fNIRS. *Biomed Opt Express*. 8(11):5326–5341. eng. doi:10.1364/BOE.8.005326.
- Verma AK, Nandakumar B, Acedillo K, Yu Y, Marshall E, Schneck D, Fiecas M, Wang J, MacKinnon CD, Howell MJ, et al. 2023. Excessive cortical beta oscillations are associated with slow-wave sleep dysfunction in mild parkinsonism. *bioRxiv*. eng. doi:10.1101/2023.10.28.564524.

- Vissani M, Palmisano C, Volkmann J, Pezzoli G, Micera S, Isaias IU, Mazzoni A. 2021. Impaired reach-to-grasp kinematics in parkinsonian patients relates to dopamine-dependent, subthalamic beta bursts. *NPJ Parkinsons Dis.* 7(1):53. eng. doi:10.1038/s41531-021-00187-6.
- Waldhauser GT, Johansson M, Hanslmayr S. 2012.  $\alpha/\beta$  oscillations indicate inhibition of interfering visual memories. *J Neurosci.* 32(6):1953–1961. eng. doi:10.1523/JNEUROSCI.4201-11.2012.
- Wichmann T, DeLong MR. 2008. Systems Level Physiology of the Basal Ganglia, and Pathophysiology of Parkinson's Disease. In: *Parkinson's Disease*. [place unknown]: Elsevier. p. 55–63.
- Wiecki TV, Frank MJ. 2010. Neurocomputational models of motor and cognitive deficits in Parkinson's disease. *Prog Brain Res.* 183:275–297. eng. doi:10.1016/S0079-6123(10)83014-6.
- Williams KA, Magnuson M, Majeed W, LaConte SM, Peltier SJ, Hu X, Keilholz SD. 2010. Comparison of alpha-chloralose, medetomidine and isoflurane anesthesia for functional connectivity mapping in the rat. *Magn Reson Imaging.* 28(7):995–1003. doi:10.1016/j.mri.2010.03.007.
- Xie P, Liu S, Huang Q, Xiong Z, Deng J, Tang C, Xu K, Zhang B, He B, Wang X, et al. 2023. Deep brain stimulation suppresses epileptic seizures in rats via inhibition of adenosine kinase and activation of adenosine A1 receptors. *CNS Neurosci Ther.* 29(9):2597–2607. eng. doi:10.1111/cns.14199.
- Yang K, Tong L, Shu J, Zhuang N, Yan B, Zeng Y. 2020. High Gamma Band EEG Closely Related to Emotion: Evidence From Functional Network. *Frontiers in human neuroscience.* 14:89. eng. doi:10.3389/fnhum.2020.00089.
- Yao M, Tudi A, Jiang T, An X, Sun Q, Li A, Huang ZJ, Gong H, Li X. 2023. Long-range connectome of pyramidal neurons in the sensorimotor cortex. *iScience.* 26(4). eng. doi:10.1016/j.isci.2023.106316.
- Yip DW, Lui F. 2024. *StatPearls: Physiology, Motor Cortical*. Treasure Island (FL): [publisher unknown].

- Yokoi A, Arbuckle SA, Diedrichsen J. 2018. The Role of Human Primary Motor Cortex in the Production of Skilled Finger Sequences. *J Neurosci.* 38(6):1430–1442. eng. doi:10.1523/JNEUROSCI.2798-17.2017.
- Young N, Stepniewska I, Kaas J. 2012. Motor Cortex. In: *The Mouse Nervous System*. [place unknown]: Elsevier. p. 528–538.
- Zimmerman EE, Kirshner HS. 2023. Cerebral Hemispheres. In: *Neurologic Localization and Diagnosis*. [place unknown]: Elsevier. p. 41–42.

## 8 Curriculum Vitae





## 9 List of Publications

- I. **Kreis, Svenja L.**; Luhmann, Heiko J.; Ciolac, Dumitru; Groppa, Sergiu; Muthuraman, Muthuraman (2022): Translational Model of Cortical Premotor-Motor Networks. In: *Cerebral cortex (New York, N.Y. : 1991)* 32 (12), S. 2621–2634. DOI: 10.1093/cercor/bhab369.
- II. Mirzac, Daniela; **Kreis, Svenja L.**; Luhmann, Heiko J.; Gonzalez-Escamilla, Gabriel; Groppa, Sergiu (2023): Translating Pathological Brain Activity Primers in Parkinson's Disease Research. In: *Research (Washington, D.C.)* 6, S. 183. DOI: 10.34133/research.0183.
- III. Bange, Manuel; Gonzalez-Escamilla, Gabriel; Herz, Damian M.; Tinkhauser, Gerd, Glaser, Martin; Ciolac, Dumitru; Pogosyan, Alek; **Kreis, Svenja L.**; Luhmann, Heiko J.; Tan, Hailing; Groppa, Sergiu (2024): Subthalamic stimulation modulates context-dependent effects of beta bursts during fine motor control. In: *Nat Commun* 15, 3166 DOI: <https://doi.org/10.1038/s41467-024-47555-3>
- IV. **Kreis, Svenja L.**(2025). Toxin-Induced Rodent Models of Parkinson's Disease. In: Groppa S, Schneider SA, editors. *Translational Methods for Parkinson's Disease and Atypical Parkinsonism Research*. Vol. 213. New York, NY: Springer US. p. 79–88 (Neuromethods).
- V. **Kreis, Svenja L.**; Gonzalez-Escamilla, Gabriel; Mirzac, Daniela; Muthuraman, Muthuraman; Luhmann, Heiko J; Groppa, Sergiu: Frequency- and layer-specific effects of high-frequency STN stimulation on mouse motor cortical areas in vivo (in preparation)

## 10 Acknowledgements

I would like to express my deepest gratitude to those who have supported me throughout my PhD journey.

First and foremost, I extend my sincere thanks to my supervisors, Prof. Luhmann, Prof. Duch, for giving me the opportunity to work on this project, and for their invaluable guidance and unwavering support. Their expertise and encouragement have been instrumental in the successful completion of this thesis. I am profoundly grateful to my mentors, whose support has been indispensable. Your constant availability, especially during the early stages of my project when I often felt lost with the analysis, was a cornerstone of my progress. Your contribution of relevant data and modelling analysis significantly enhanced the impact of my first publication. Your insights and guidance have been greatly appreciated throughout this journey. At the beginning of my project, I had the privilege of learning from, a postdoctoral researcher who patiently taught me how to use our recording setup and perform surgeries on mice, thereby laying the foundation for my lab work. Your initial training and support were crucial in getting me started. I am also deeply thankful to a fellow PhD student, whose companionship and assistance during long experimental days made 14-hour recording sessions enjoyable. Your collaboration and friendship have been invaluable. A special thank you goes to our technician, for her impeccable staining work, which greatly facilitated the reliability and ease of my research. Your technical expertise and dedication have been a tremendous asset to my work. I would also like to extend my gratitude to all the members of our lab, whose assistance with various challenges, both big and small, made the lab environment supportive and relaxed. Lastly, I want to express my heartfelt thanks to my boyfriend, my parents, and my brother. Your unwavering support, encouragement, and love have been my pillars of strength throughout this journey.

Thank you all for being part of this incredible journey.

## 11 Abbreviation

CFA	rostral forelimb area
DBS	deep brain stimulation
EC	effective connectivity
EEG	Electroencephalography
FC	functional connectivity
fMRI	Functional Magnetic Resonance Imaging
Gpe	globus pallidus externus
GPI	globus pallidus internus
HFS	high frequency stimulation
i.p.	Intraperitoneal
kHz	Kilohertz
L	cortical layer
L2/3	cortical layer 2/3
L5	cortical layer 5
L6	cortical layer 6
LFP	local field potential
LMM	Linear Mixed-Effects Models
M1	primary motor cortex
MEA	multi-electrode array
MUA	multi unit activity
PBS	phosphate buffered saline
PFA	paraformaldehyde
PMC	premotor cortex
RFA	rostral forelimb area
SD	standard deviation
SNpc	substantia nigra pars compacta
SNr	substantia nigra pars reticulata
SPC	Super-paramagnetic clustering
STN	subthalamic nucleus
SU	single unit

tPDC    time-resolved partial directed coherence